Development of Tri-layered Biomimetic Atelocollagen Scaffolds with Interfaces for Osteochondral Tissue Engineering

Yang(Jim) Xu

St Anne's College

A Thesis Submitted for the Degree of Doctor of Philosophy

Department of Materials, University of Oxford

Abstract

The development of biomimetic scaffolds for cartilage, calcified cartilage and bone regeneration for precise osteochondral repair remains a challenge. In this study, we used liquid-phase co-synthesis to construct a novel tri-layered scaffold with the top layer containing type II atelocollagen and chondroitin sulphate for cartilage regeneration, the intermediate layer with type II atelocollagen and hydroxyapatite for calcified cartilage formation and the bottom layer with type I atelocollagen and hydroxyapatite for bone growth. The tri-layered scaffold designed in this study is mechanically superior to other tri-layered scaffolds with hard interfaces and has a lower risk of delamination owing to higher cohesion resulting from the interfaces between the layers of the scaffold. In vitro analyses revealed that although mono-layered scaffolds stimulated bone marrow stem cells to differentiate and form cartilage, calcified cartilage and bone separately (detected using quantitative PCR analysis and staining with safranin-O and alizarin red S), the tri-layered scaffolds supported the regeneration of cartilage, calcified cartilage and bone simultaneously after 2 and 4 months of implantation (detected using gross and micro-CT imaging, histological staining and Avizo, a three-dimensional reconstruction tool used to detect micro-level defects usually in metals). Therefore, our study presents a promising approach to devising strategies for the precise repair of osteochondral defects.

Acknowledgement

I would like to express my great gratitude to Prof. Jan Czernuszka, who has been a tremendous supervisor for me. Especially, I want to thank you for giving the freedom to explore the in-vivo works even though that are very challenging. Thanks for giving me the trust and flexibility in term of establishing the collaboration with the external research group. I wouldn't able to finish this work if it wasn't for this.

I also wish to thank Prof. James Marrow from our department of materials. Thank you for giving me the enlightening advice and offering the assess to the micro-CT. I learnt from you and your team immensely. I would also like to thank Jennifer from David Cockayne Centre for Electron Microscopy for providing me the training for SEM and EDX. I wish to thank every colleague in our biomaterial research group, especially those who directly participated in my project, I am so glad we have a great team culture and supporting environment.

I would like to mention and express my tremendous thanks for our external collaborator from Shanghai No.9 People's Hospital, without your help I could never be able to complete my in-vitro cell work and in-vivo animal work.

I would also wish to mention my peer mates at St Anne's college, it was so much fun when spending free time with you guys.

Last but very importantly, I want to thank my family for supporting me all the way, especially during my writing-up at Covid-19 period.

Contents

Chapter 1. Introduction

Osteochondral defects (ODs) are usually caused by acute trauma, osteochondritis dissecans, osteoarthritis (OA), subchondral insufficiency fractures or osteonecrosis.[1] ODs are clinically challenging for surgeons to repair because they extend beyond the superficial cartilage into the calcified cartilage and occasionally involve the subchondral bone. Without appropriate treatment, degenerative joint diseases such as OA usually develop in the afflicted area, which seriously affects joint function and the quality of life.[2] Currently, routine clinical treatment strategies for ODs include total replacement, allograft/autograft implantation and microfracture surgery.[3] However, these treatments have several inherent limitations; total replacement leads to postoperative activity restriction,[4] autograft/allograft implantation is limited by secondary damage and topology mismatch[5] and microfracture surgery frequently leads to fibrocartilage formation and insufficient cartilage repair.[6] Although long-term results of autologous chondrocyte implantation in the knee are satisfying, a failure rate of 14.9% within the first 5 years of surgery has been heterogeneously defined in the literature.[7, 8]

Recently, researchers have devised several alternative treatment strategies for ODs. Of these, tissue engineering using a combination of scaffolds, stem cells and bioactive macromolecules is a promising strategy. Tissue engineering comprises two subcategories, namely, cell-seed scaffolds (where cells harvested from patients are cultured in vitro before being seeded on a scaffold for implantation[9]) and cell-free scaffolds (which rely on the cells of patients infiltrating the scaffold matrix and subsequently synthesising and rebuilding the osteochondral tissue matrix[10]). Despite numerous advances in the treatment of ODs using cell-seed scaffolds, this

technique is difficult to use because preculturing of cells is complicated and time-consuming.[11] Therefore, single-step treatment with cell-free scaffolds should be developed for OD repair.[12]

To date, biomimetic scaffolds that closely mimic the natural osteochondral tissue and multi-layered scaffolds such as tri-layered scaffolds that mimic cartilage, calcified cartilage and subchondral bone have been developed.[13-15] However, some critical issues need to be addressed before using these approaches in clinical settings. First, some scaffolds have improper cartilage and bone matrix composition, which can introduce undesirable microenvironmental signals that may misdirect cell differentiation and result in poor repair outcomes. One such problem is the use of type I collagen for fabricating the cartilage layer of the scaffold; however, type II collagen is predominantly found in the natural cartilage. Similarly, type II collagen has been used for bone matrix formation; however, type I collagen is predominantly found in bones.[16, 17] Second, most multi-layered scaffold designs have hard interfaces between the layers, which can lead to delamination or mechanical failure under in vivo conditions once the scaffold is implanted. This can dramatically affect the outcomes of implantation and hinder optimal repair.[18]

In this study, we attempted to design a one-step OD treatment strategy that uses a cell-free and growth factor-free integrated tri-layered scaffold. The scaffold was fabricated via liquid-phase co-synthesis with gradient/soft interfaces and appropriate collagen types to address the prevailing issues of the currently available scaffolds. The scaffold designed in this study has three layers: a top layer with type II atelocollagen (COL II) and chondroitin sulphate (CS) for cartilage regeneration (COL II/CS), an intermediate layer with COL II and hydroxyapatite (HAP) for calcified cartilage formation (COL II/HAP) and a bottom layer with type I atelocollagen (COL I) and HAP

for bone growth (COL I/HAP). We hypothesised that the correct type of collagen can provide appropriate microenvironmental signals to stem cells so that the newly regenerated osteochondral tissue formed on the scaffold is of better quality. In addition, gradient/soft interfaces between the layers in the scaffold reduce the chances of mechanical failure and make this scaffold more reliable than those developed previously. The main objectives of this study are summarised as follows:

- To investigate and understand the compositional, structural, mechanical and biological properties of the natural osteochondral joint by reviewing relevant research and publications (Chapter 2)
- To fabricate the tri-layered osteochondral device via monomeric collagen extraction (type I and II), incorporating chondroitin sulfate (CS) or hydroxyapatite (HAP) using a liquid-phase co-synthesis method to produce integrated porous scaffolds with interfaces between the layers (Chapter 3)
- To characterise the composition and structure of the tri-layered scaffold via several techniques including Fourier-transform infrared spectroscopy (FTIR), scanning electron microscopy (SEM), energy-dispersive X-ray (EDX) spectroscopy and micro-computed tomography (micro-CT) (Chapter 3)
- To determine the mechanical properties including compression, tensile strength and delamination of the prepared scaffolds via dynamic mechanical analysis (DMA) (Chapter 4)
- To determine the clinical effectiveness of the tri-layered scaffold via in vitro experiments, including cell viability assay, DNA quantification, cell attachment assay, histological analysis and real-time polymerase chain reaction (q-PCR) (Chapter 5)

- To determine the clinical effectiveness of the tri-layered scaffold in vivo by assessing whether the scaffold could repair the knee joint in rabbits using micro-CT and histological analysis (Chapter 6)

Chapter 2. Literature review

2.1 Introduction

Tissue engineering aims at regenerating damaged tissues using appropriate combinations of scaffolds, cells and growth factors. This study aimed to design, fabricate and characterise collagen-based scaffolds for OD repair (in both cartilage and bone). A comprehensive understanding of the compositional, structural, biomechanical and biological properties of the natural osteochondral tissue is vital for designing an ideal biomimetic scaffold. Therefore, this chapter presents the literature review performed for the study. The first two sections (Section 2.2 and 2.3) describe the anatomy, composition, structure and mechanical properties of the natural cartilage, bone and cartilage–bone interface. Furthermore, the scope of ODs, currently available surgical treatments and novel treatments are also discussed (Section 2.4.1 and Section 2.4.2). The next section entails a comparative study of the recent research data regarding innovative treatments proposed using collagen scaffolds, including their advantages and disadvantages (Section 2.4.3). The final section entails the aim of this study (Section 2.5).

2.2 Anatomy, composition, structure and mechanical properties of cartilage

2.2.1 Anatomy of cartilage

Cartilage is an avascular connective tissue located on the surface of articular joints, with strong compressive, tensile and shear strengths. The articular cartilage has a minimal intrinsic healing capacity,[19] with a thickness between 0.1 and 5 mm depending on the species and location.[20] It comprises four unique zones: superficial, middle, deep and calcified (the transitional region from cartilage to bone).[21, 22] The material composition, matrix structure and biological properties of cartilage vary

significantly with the depth.[15] The characteristics of the four cartilage layers are summarised in **Table 2.1** and elaborated below.

Superficial zone

In the superficial zone, chondrocytes have the highest cell density with flattened cell shape. The concentration of type II collagen is highest in this zone. Moreover, the proteoglycan content is lower, and packed layers of uniform collagen fibres are oriented parallel to the surface.[23] The superficial zone constitutes approximately 10–20% of the total articular cartilage thickness, playing a vital role in protecting the deeper layers from external shear loading.[24] In addition, this zone has the highest tensile strength.

Middle zone

The middle zone is located underneath the superficial zone and occupies 40–60% of the total cartilage volume. Unlike the chondrocytes in the superficial zone, the cells in the middle zone have low density and a spherical shape. The collagen fibrils are larger in diameter and unaligned,[25] and the proteoglycan content is higher.[26] The middle zone is the first line of resistance to compressive forces, acts as a transition phase between the superficial and deep cartilage zones and provides a collagen matrix with randomly oriented fibres, which act as a compressive layer to respond to external forces.[27]

Deep zone

The deep zone that accounts for approximately 30% of the cartilage thickness is mainly made of type II collagen fibres that are oriented perpendicular to the superficial

layer. In addition to type II collagen, type X collagen is present at an appreciable degree in this zone. The content of glycosaminoglycans (GAGs) and aggrecan is high.[22] Furthermore, this zone has the highest resistance to compressive forces, given that collagen fibrils are perpendicular to the articular fibrils. In addition, this zone has the highest proteoglycan content.[28]

Tidemark

Tidemark is a thin distinct layer that separates the calcified zone and subchondral bone.[29] It is made of a matrix consisting of small branching fibres, which serves to distribute the mechanical force through the tidemark along the whole cartilage–subchondral bone area.[30]

Calcified cartilage zone

Calcified cartilage is the deepest zone of articular cartilage, which has a similar composition to that of the deep layer with additional calcified collagen and HAP.[22] The length of this zone is between 20 and 243 μm in humans, depending on the location.[31] Cells and proteoglycans are absent in this zone.[32] The function of this zone is to support cartilage-to-bone integration. Moreover, it also acts as a barrier to prevent vascular invasion.[33] The mechanical strength of this zone is between that of articular cartilage and bone.[34]

Table 2.1 Summary of characteristics of the four cartilage layers

Zone	Length/ depth	Collagen content	Proteoglycan content	Cell amount/ morphology	Fibril and orientation

Superficial	10–20%	Highest	Lowest	Highest/flattened	Parallel/uniform
Middle	40–60%	Intermediate	Intermediate	Intermediate/random	Larger diameter/unaligned
Deep	30%	Lowest	Highest	Lowest/spherical	Perpendicular
Calcified	/	/	/	Low	/

2.2.2 Composition of cartilage

Articular cartilage, like many other tissues, is made of cells and extracellular matrix (ECM). Cartilage-specific cells, called chondrocytes, are embedded in ECM. The cartilage ECM matrix comprises collagen, proteoglycans and non-collagenous proteins (**Figure 2.1**). Water accounts for approximately 70–80% of the weight of articular cartilage, whereas collagen and GAGs account for the remaining 20% of the weight. The collagen component in articular cartilage mostly includes type II collagen; type I collagen is not found in the natural articular cartilage.[35] The major GAG component is CS, which constitutes approximately 20% of the dry cartilage weight.[36]

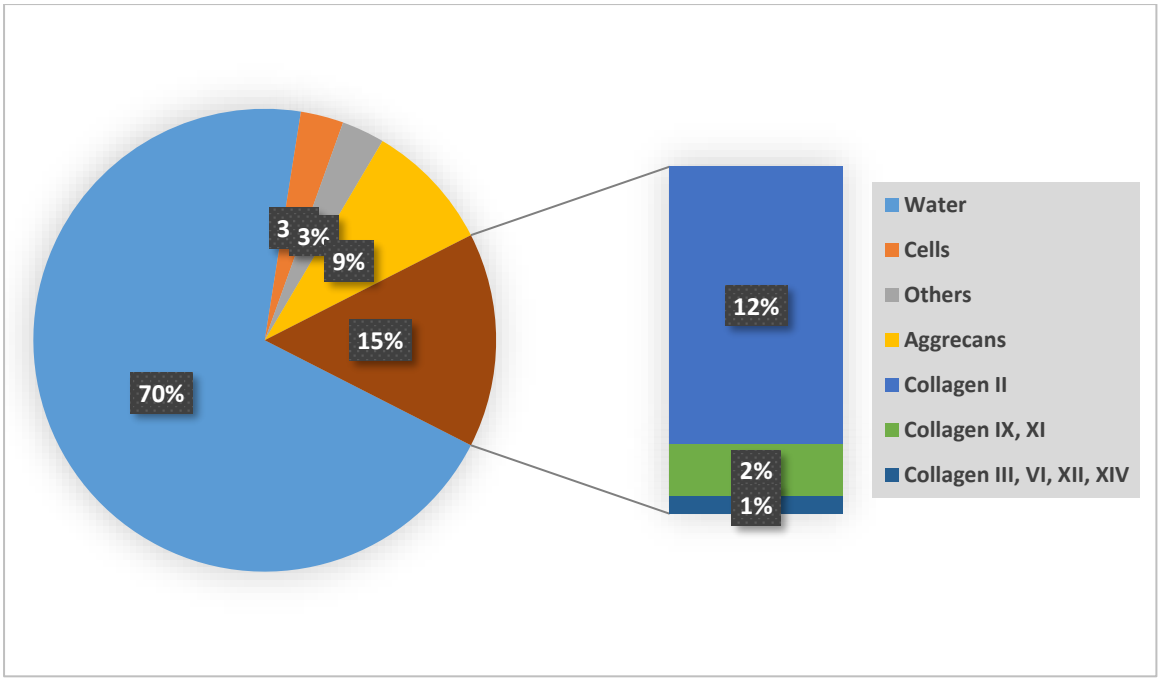

Figure 2.1 Composition of the articular cartilage, adapted from [37].

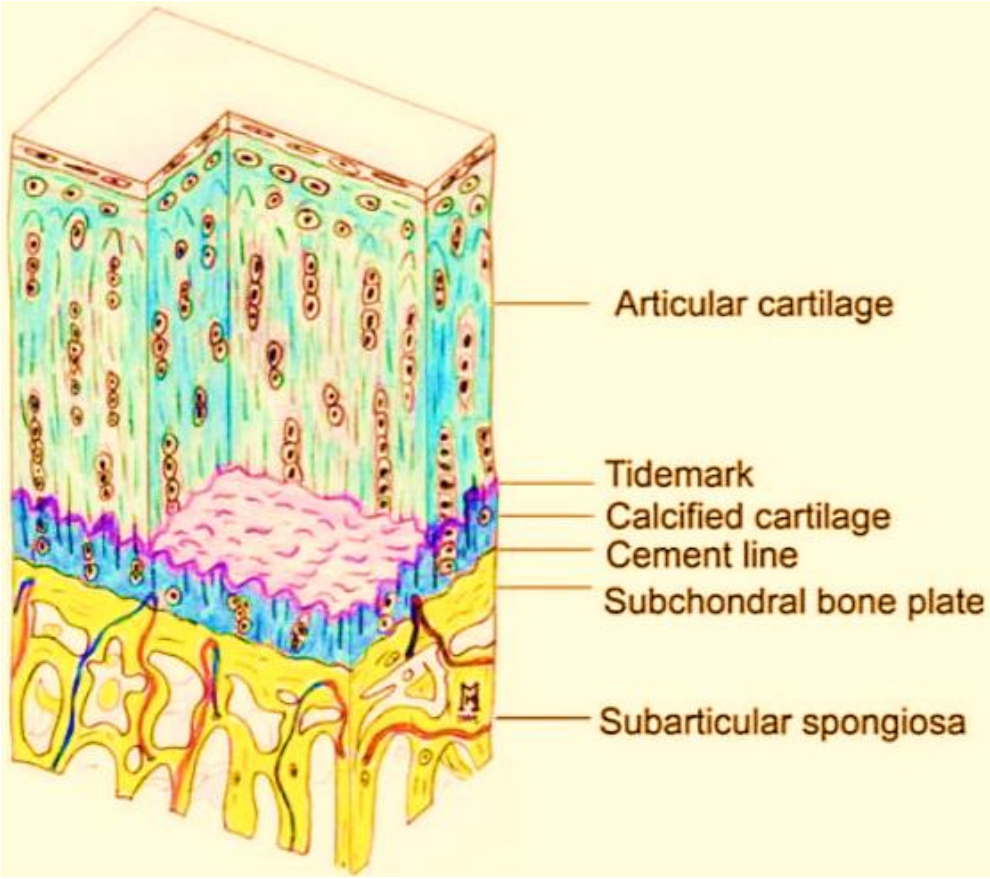

Figure 2.2 Osteochondral joint structure: subchondral bone plate and subarticular spongiosa. Adapted from [35][38].

Collagen

Amount: Collagen is an abundant structural protein, constituting approximately 30% of total body proteins and 60% of the dry weight of cartilage in mammals.[39] It contributes to a majority of the structural and mechanical properties of cartilage.[40]

Types: The types of collagen found in the cartilage ECM include the following:

- Type II: 80% of collagen in the articular cartilage is type II collagen.[41]
- Type VI: It closely surrounds the chondrocytes.[42]
- Type IX: It is found on the surface of type II collagen fibrils.[43]
- Type X: It is found near the calcified cartilage layer and plays a vital role in bone mineralisation.[44]
- Type XI: It helps to resemble the type II collagen matrix structure.[45]

Function:

- Collagen provides mechanical strength and stiffness to cartilage.[46]

Proteoglycans

Amount: 25–35% of the dry cartilage weight

Types:

- **Aggregating (GAGs):** CS, hyaluronic acid, keratan sulphate and dermatan sulphate
- **Non-aggregating:** Decorin, biglycan and fibromodulin

Functions:

- Proteoglycans contribute to the mechanical properties of tissues.[47]
- They contribute to biological properties such as cell adhesion, migration, proliferation and differentiation.[48]

Water and tissue fluid

Amount: 60–80% of the wet cartilage weight[49]

Function: Protection of the solid phase under mechanical stress and supply of nutrients and oxygen[50]

Chondrocytes

Amount: 1–10% of the dry cartilage weight[51]

Function: Synthesis of cartilage ECM and maintenance of ECM by continuously replacing the degraded component

2.2.3 Mechanical properties of cartilage

The mechanical function of articular cartilage is to minimise the contact stress and friction between two adjacent bones. Two important and common parameters for the assessment of the mechanical properties of cartilage are compression and tension tests.

Compression modulus of natural cartilage

Two approaches are available to measure the compression modulus: confined or dynamic (indentation) compression. **Table 2.2** summarises the values and methods for evaluating the compression modulus of natural cartilage as described in various studies. The elastic modulus of articular cartilage varies among different species, such as humans, bovines, canines and pigs. In addition, articular cartilage in humans exhibits the highest elastic modulus.

Table 2.2 Measurement of compressive modulus in the articular cartilage of native species

Species	Elastic modulus (MPa)	Method	Ref.
Humans	0.7±0.2	Creep indentation	[10][52]
	5.1	Confined compression	[37][53]
	5.8	Creep indentation	[38][54]
Bovines	0.5±0.1	/	[10][52]
Canines	0.6±0.1	Creep indentation	[10][52]
Pigs	2.6	Indentation	[39][55]

Tensile modulus of the natural cartilage

Collagen content is correlated with tensile strength and stiffness. Tensile strength increases with the increased collagen content of cartilage tissue. Tensile modulus is higher in the upper layer of cartilage in native species as demonstrated in **Table 2.3**.[56] In the superficial zone, the tensile modulus of the lateral patella groove is between 6.22 and 20.67 MPa, and that of the medial femoral condyle is between 4.98 and 10.13 MPa. In the middle zone, the tensile modulus of the lateral patella groove is between 3.12 and 4.14 MPa, and that of the medial femoral condyle is between 3.10 and 4.54 MPa. In the deep zone, the tensile modulus of the lateral patella groove is between 0.93 and 1.01 MPa. Therefore, it is better to fabricate a scaffold with three distinct layers to mimic the native articular cartilage.

Table 2.3 Tensile modulus of articular cartilage in native species

	Zone	Lateral patella groove		Medial femoral condyle	
Tensile modulus (MPa)	Superficial zone	6.2±1.6	20.7±3.0	5.0±1.7	10.1±1.8
	Middle zone	3.1±1.2	4.1±1.7	3.1±0.7	4.5±1.3
	Deep zone	0.9±0.4	1.0±0.7	/	/

2.3 Anatomy, composition, structure and mechanical properties of subchondral bone

2.3.1 Anatomy of subchondral bone

Subchondral bone is located just below the cartilage tissue in the osteochondral joint and is a shock absorber in weight-bearing joints. Blood vessels are present for the supply of nutrients and oxygen in subchondral bone, unlike in cartilage.[25] Subchondral bone is made of two mineralised zones, namely, the subchondral bone plate and subarticular spongiosa, which separate the articular cartilage from the bone marrow (**Figure 2.2**).

2.3.2 Composition of subchondral bone

The bone matrix is a composite of organic and inorganic components. The predominated organic component in bone is type I collagen, and the primary inorganic component is a specific type of calcium phosphate mineral named HAP with the chemical formula of $Ca_{10}(PO_4)_6(OH)_2$.[25]

Based on mass percentage, bone is composed of 60% mineral, 30% collagen and10% water as demonstrated in **Figure 2.3**. Type I collagen primarily accounts for 90% of the collagen content of the bone. Collagen II is absent. Other types of collagen include collagen V, VIII and XII.[57]

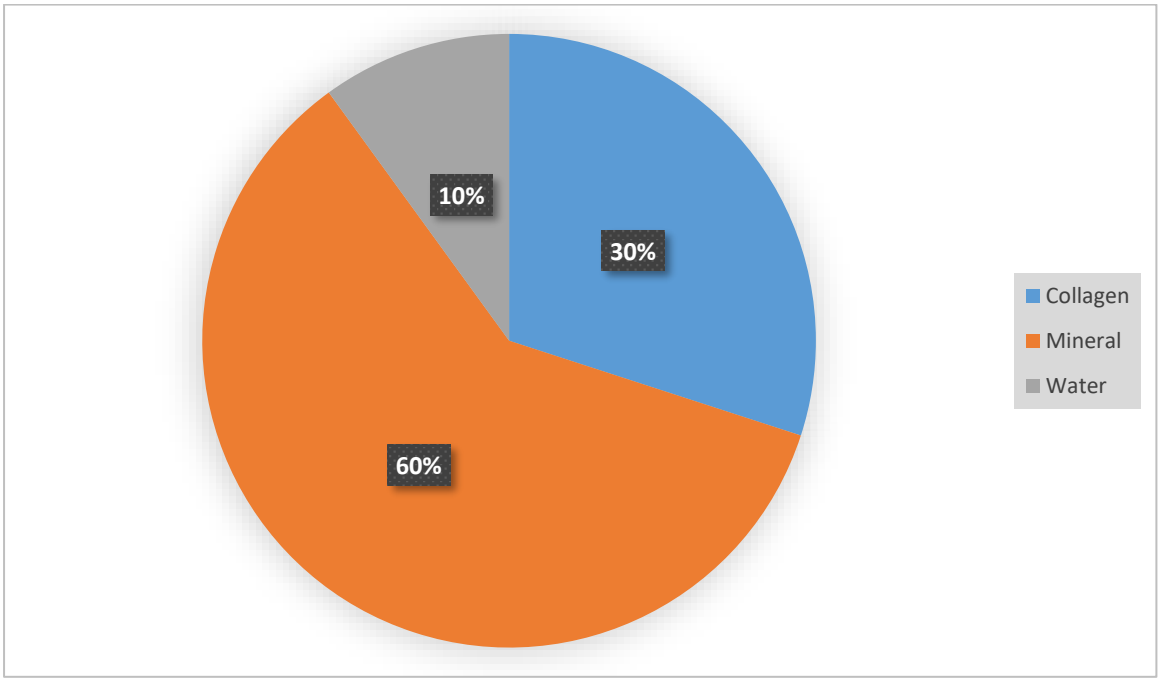

Figure 2.3 Composition of bone: collagen, mineral and water. Adapted from [40][57]

Cells

Three types of cells with different functions are present in the bone tissue: osteoblasts, osteocytes and osteoclasts. The bone matrix is continuously remodelling itself, with osteoblasts producing and mineralising the new bone and osteoclasts resorbing the old matrix. Osteocytes play an important role in maintaining the bone matrix.[58]

2.3.3 Mechanical properties of subchondral bone

As a composite of collagen fibres and HAP, bone is highly resistant to compressive forces. The tensile property of bone, however, is relatively weak.[59] **Table 2.4** demonstrates mechanical data from previous studies. In the subchondral compact bone plate, the density is 1.8 g/cm^3, compressive strength is 133 MPa and tensile

strength is 49–60 MPa. In the subchondral spongiosa, the density is 0.2 g/cm^3, compressive strength is 0.5–100 MPa and tensile strength is 1–20 MPa.

The two factors that affect the mechanical properties of subchondral bone are compositional and organisational. Compositional factors include the mineral content and porosity of the matrix, wherein the increasing degree of mineralisation and the decreasing porosity of the matrix lead to high stiffness but lower fracture strain. Organisational factors include the orientation of collagen fibrils and spacing of trabeculae.[60] The subchondral bone plate (compact) has a stronger mechanical property than that of subchondral spongiosa (spongy) because the bone plate has high density and hence a higher degree of mineralisation and lower porosity.

Table 2.4 Mechanical properties of subchondral bone plate and spongiosa

Type of bone	Subchondral bone plate (compact)	Subchondral spongiosa (spongy)
Density (g/cm^3)	1.8[57]	0.2[57]
Compressive strength (MPa)	133[59]	1–100[59] 0.5–50[60]
Tensile strength (MPa)	49[59] 50–60[61]	1–6[61] 10–20[60]

2.4 Osteochondral defect and treatment

2.4.1 Osteochondral defect

In the past decades, considerable efforts have been made to develop clinical treatment strategies for articular cartilage defects. However, cartilage defects extending deep

into the underlying subchondral bone have not been receiving adequate attention. OD is a type of articular cartilage defect that affects both articular cartilage and the underlying subchondral bone (**Figure 2.4**). This defect is difficult to treat because the subchondral bone and articular cartilage are tissues with different intrinsic properties (e.g. composition, structure, mechanical properties and self-healing capacity). Untreated osteochondral lesions may lead to OA, a prevalent degenerative joint disease.[62] Repair of articular cartilage is a relevant clinical therapeutic strategy to prevent the progression of OA.[63]

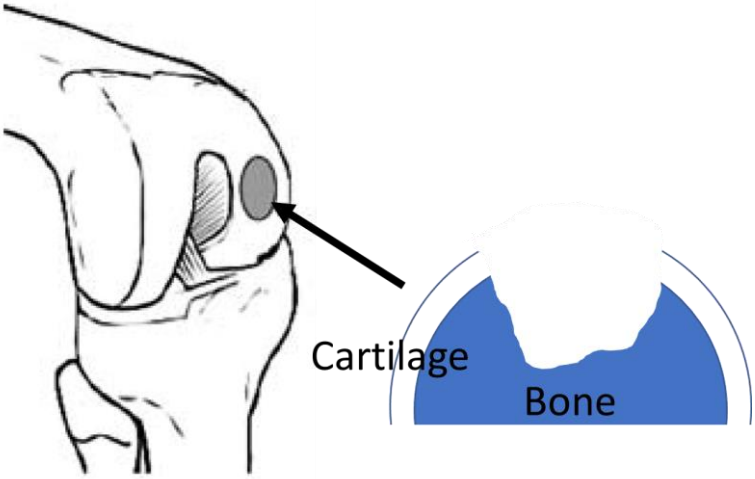

Figure 2.4 Osteochondral defect that damages both cartilage and bone. Adapted from [64].

2.4.2 Treatment of osteochondral defect

Currently available clinical gold-standard methods of surgical intervention for OD repair are described below.

1) Total joint replacement

Total knee replacement, also known as knee arthroplasty, uses an artificial material (metal) to replace the damaged knee joints with a large defect area. Total joint replacement is one of the surgical techniques to restore the function of joints. Although the promising clinical result of pain relief is achieved after total knee replacement,

potential postoperative infection and significant activity restrictions are the main drawbacks of this technique.[65]

2) Autologous chondrocyte implantation

Autologous chondrocyte implantation (ACI) aims to replace the damaged cartilage with hyaline cartilage. A small piece of articular cartilage is removed from the knee, and chondrocytes are cultured in a laboratory until millions of cells are formed, which are implanted into the damaged area. The technique of ACI has evolved since its emergence. In the first generation of ACI (ACI-periosteum [ACI-P]), the cultured cells were implanted as a liquid suspension, and the implant was covered with a cap made from the periosteum, a tough fibrous tissue that covers the surface of bones. ACI-P required a procedure to harvest the periosteum, which caused discomfort to patients afterwards. In the second generation of ACI, the periosteal cover was replaced with a collagen cover (ACI-C); however, the cells were used as a liquid suspension, and the cover had to be stitched in place. A developmental aspect of ACI is ‘characterisation’, a process in which the cells considered to have the best ability to form hyaline cartilage are selected during culture. In the third generation of ACI, the cells are seeded or loaded into a collagen membrane, which is implanted into the defected area. This technique is referred to as matrix-applied chondrocyte implantation.[66-69]

3) Autograft/allograft transplantation (two-step approach)

Autograft/allograft transplantation involves two surgical procedures. The first step is to collect a healthy full-thickness sample from a non-weight-bearing region of the joint of a patient or an external donor, and the second step is to implant the well-expanded sample into the damaged cartilage of the patient.

Although some promising clinical results have demonstrated autograft/allograft transplantation as an effective and durable treatment strategy for large (>4 cm^2) knee cartilage lesions,[70] this technique is associated with the following critical disadvantages: two surgeries are required that substantially increase the treatment complexity, pain and uncertainty, cause damage to the healthy tissue (autograft) and induce potential immune reactions (allograft). In addition, a long recovery time (6–12 months) is required.

4) Microfracture (one-step approach)

Microfracture was introduced to treat early-to-middle stage of ODs. Briefly, damaged cartilage tissue is debrided, followed by the creation of multiple holes (‘microfractures’) approximately 3–4 mm apart via an arthroscopic awl. The bone marrow-derived mesenchymal stem cells (BMSCs) subsequently migrate to the site of the cartilage defect and are expected to proliferate and differentiate to form new cartilage and bone tissue. Microfracture is typically used to treat small defects ranging between 1 and 2.5 cm^2 in size.

However, the formation of fibrocartilage is biomechanically inferior to and biochemically incompatible with the healthy hyaline cartilage. A study demonstrated that the repaired tissue is vulnerable to mechanical joint forces and typically deteriorates within 18–24 months of surgery.[71] Moreover, intralesional osteophytes are developed in 20–50% of cases owing to the penetration of subchondral bone.[72]

Despite the promising results achieved by clinical gold-standard methods, as mentioned above, the complication rate is high owing to their critical drawbacks (**Table 2.5**).

Table 2.5 Clinical gold-standard methods for articular cartilage repair: summary of their procedure and drawbacks.

	Total replacement	Autograft/allograft	Microfracture
		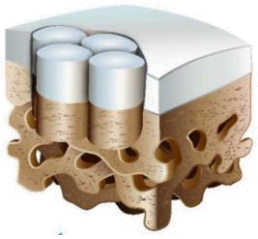	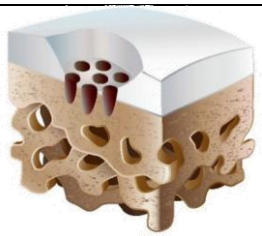
Operation steps	One step	Two steps	One step
Drawbacks	• End-stage • Infection • Limited lifespan (5 years) • Activity restriction	• Complex • Secondary damage • Lack of donors • Immune reaction	• Fibrocartilage • Incompatible • Intralesional osteophytes

5) Novel approaches proposed by recent research and development

Alternative approaches such as stem cell therapy, tissue engineering and organogenesis have been intensively investigated in the past decades. Of these approaches, tissue engineering is a promising clinically feasible approach involving innovative materials, cell transplantation and biomolecules. Tissue engineering

imitates the natural body condition to enhance and leverage the regenerative ability of the body to repair ODs.[73]

The three major components in osteochondral tissue engineering include a scaffold (natural or synthetic), cells (usually bone marrow stem cells of a patient or an external donor) and inductive biomolecules (growth factors) (**Figure 2.5**).

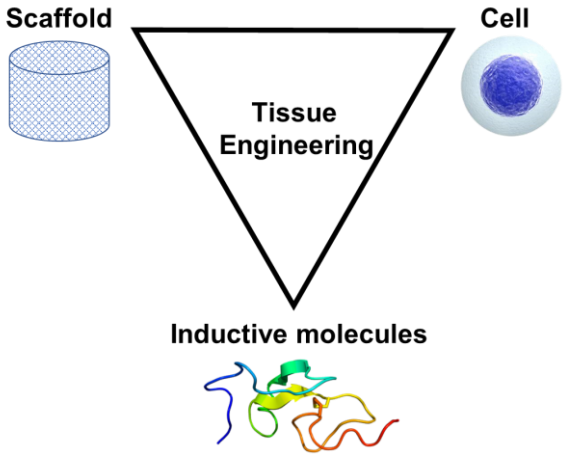

Figure 2.5 Three major components of tissue engineering: scaffold, cells and inductive biomolecules.

The role of the scaffold is to establish a matrix providing not only physical, structural support to cells but also biological guidance for cell growth and differentiation. An ideal scaffold for OD treatment should provide a degradation rate comparable to the production rate of neotissue in the body. It should also have appropriate porosity (pore size should be larger than 50 µm) and pore interconnectivity for cell growth and exchange of nutrients and waste products. In addition, it should be mechanically stable to withstand intensive in vivo loading in the osteochondral joint.[74]

Cells are the primary source for neotissue regeneration. The cell types used for OD repair are bone marrow stem cells and chondroprogenitor cells because they can differentiate into chondrocytes and osteoblasts.[75]

The role of inductive biomolecules (growth factors) is to instruct and regulate cell behaviour, particularly for cell proliferation and differentiation.[76] The growth factors are usually physically or chemically attached to the scaffolds.

Commonly used growth factors in tissue engineering include transforming growth factors (TGFs), bone morphogenetic proteins (BMPs), fibroblast growth factors (FGFs) and vascular endothelial growth factor (VEGF).

Favourable osteochondral regeneration in vivo/in vitro may attribute to the following aspects:

1) biocompatibility

2) biodegradability

3) suitable pore structure for cell distribution and nutrient supply

4) mechanical strength

5) weak immunogenicity

6) desired microenvironment for independent differentiation

2.4.3. Development of tri-layered biomimetic atelocollagen scaffolds for osteochondral defect repair

Despite significant advances in the treatment of damaged articular cartilage via cell- and growth factor-assisted approaches, an off-the-shelf, low cost, one-step approach

is required for clinical treatment of OD repair. This study aimed to design a one-step off-the-shelf collagen-based scaffold without using cells and growth factors. Therefore, we reviewed relevant studies published in this specific field.

Early stage of collagen scaffold development: Mono-layered collagen scaffolds

Mono-layered (homogenous) collagen scaffolds have been intensively explored. Related studies have explored both type I and II collagen scaffolds and incorporated CS or HAP for building a better biomimetic model of the natural osteochondral tissue. In some studies, chemical crosslinkers have been used to enhance the mechanical properties of scaffolds.

However, most studies only focus on either bone or cartilage; however, the defect usually affects both. In some studies, attempts were made to repair OD defects using a one-step approach; however, the result was usually the formation of fibrocartilage.

For bone-focussing type I collagen scaffold, as shown in **Table 2.6**, homogenous type I collagen is not ideal for in vivo implantation owing to its weak mechanical properties. Porous calcium phosphate ceramics such as HAP, tricalcium phosphate (TCP) and biphasic calcium phosphate (BCP) have been incorporated because they can reinforce the matrix to increase the mechanical strength. The major drawbacks of this type of collagen scaffold are as follows:

1) Poor cartilage repair outcome: Osteochondral joint defects usually involve both cartilage and bone damage; however, type I collagen scaffolds regenerate fibrocartilage instead of hyaline cartilage.

2) Type I collagen scaffolds, as shown in **Table 2.6**, sometimes require additional growth factors or pre-seeded MSCs, which further complicate surgery.

In a study, mono-layered type I collagen scaffolds without crosslinking exhibited a weak Young's modulus of 0.04 kPa,[76] resulting in no in vivo outcome (**Table 2.6**). Furthermore, mono-layered type I collagen/HAP composite scaffolds with co-precipitation exhibited enhanced mechanical property with a Young's modulus of 1.93k Pa, resulting in only bone defect repair and poor cartilage repair.[77] In addition, mono-layered type I collagen/HAP/PCL composite scaffolds with 1-ethyl-3-(3-dimethylaminopropyl) carbodiimide/N-hydroxysuccinimide (EDC/NHS) crosslinking improved the mechanical properties with a Young's modulus of 3.5–8.5 kPa, resulting in successful large bone defect repair. However, this type of repair requires pre-cultured MSCs and growth factors (owing to the lack of a chondrogenesis-inducing component in the type I collagen/HAP/PCL composite scaffold).[78]

Given that type I collagen scaffolds often regenerate fibrocartilage instead of hyaline cartilage, researchers attempted to use type II collagen scaffolds aiming at better cartilage repair outcomes. In a study, a mono-layered type II collagen/CS scaffold was fabricated without crosslinking or co-participation, which exhibited weak mechanical properties with a Young's modulus of approximately 0.02–0.28 kPa.[79] However, no bone or cartilage defect repair was achieved in vivo owing to weak mechanical properties. A study reported the development of a mono-layered type II collagen/CS scaffold with EDC/NHS crosslinking; however, no bone or cartilage defect repair was reported [80]. Furthermore, a study reported the synthesis of a mono-layered type II collagen scaffold with EDC/NHS crosslinking, achieving 40% hyaline cartilage repair in a canine model with chondrocyte-seeded matrix.[81] In a similar study, a mono-

layered type II collagen scaffold with Genipin crosslinking was fabricated and repopulated with MSCs to achieve adequate cartilage repair after 24 weeks of in vivo implantation.[82] Furthermore, a mono-layered type II collagen/CS with Genipin crosslinking was fabricated to mimic the cartilage niche and repopulated with MSCs to achieve better cartilage repair compared with type II collagen scaffold after in vivo implantation.[83]

The major drawbacks of cartilage-focussing type II collagen scaffolds are summarised as follows (**Table 2.6**):

1) Homogenous type II collagen scaffolds have weak mechanical properties and hence cannot remain stable in the in vivo environment.[77]

2) Poor bone repair: The natural bone matrix is made of type I collagen instead of type II collagen, and osteochondral joint defects often involve both cartilage and bone damage.

3) Type II collagen scaffolds sometimes require pre-seeded MSCs, which further complicate surgery.

Table 2.6 Mono-layered collagen scaffolds for osteochondral defect repair

Composition	Structure	Fabrication	Young's modulus	In vivo application	Outcomes	Ref
CI*	Mono-layer	No crosslinking	0.04 kPa	No in vivo results owing to	Weak mechanical properties	[78]

				weak mechanical properties		
CI + HAP*	Mono-layer	Co-participation	1.9 kPa	Bone defect repair	Poor cartilage repair	[79]
CI + HAP PCL*	Mono-layer	EDC/NHS* crosslinking	3.5 kPa 8.5 kPa (PCL)	Large bone defect repair	Requires pre-cultured MSCs and growth factors	[80]
CII* CII + CS*	Mono-layer Mono-layer	No crosslinking Co-precipitation	0.02 kPa 0.28 kPa	No in vivo results owing to weak mechanical properties	Weak mechanical properties	[81]
CII + CS	Mono-layer	EDC/NHS crosslinking	/			[82]
CII	Mono-layer	EDC/NHS crosslinking	/	40% hyaline cartilage	A canine model with chondrocyte-seeded matrix	[83]
CII	Mono-layer	Genipin crosslinking	/	Adequate cartilage repair after 24 weeks	Requires pre-cultured MSCs;	[84]

					only cartilage is targeted	
CII + CS	Mono-layer	Genipin crosslinking	/	Better cartilage repair in CII + CS than in CII	Requires pre-cultured MSCs; only cartilage is targeted	[85]

CI* = Collagen type I
CII* = Collagen type II
HAP* = Hydroxyapatite
CS* = Chondroitin sulfate
PCL* = Polycaprolactone
EDC/NHS* = Reactive carbodiimide (EDC-HCl) and sulfo-NHS

Mid-stage collagen scaffold development: Bi-layered collagen scaffolds

Owing to the different intrinsic structures and physiological functions of cartilage and bone, single-layer tissue engineering scaffolds with homogenous properties may not be ideal for supporting the metabolic and morphogenic activities of multiple cell types. Therefore, researchers started to combine two different collagen scaffolds to form bi-layered scaffolds for simultaneous cartilage and bone repair (**Table 2.7**).

This bi-layered combination strategy achieved considerable success in dealing with both cartilage and bone repair simultaneously. However, a lack of transition phase between the two layers of bi-layered scaffolds leads to potential mechanical failure including delamination and biological issues such as vessel penetration into the cartilage region.[86, 87] In a study, the scaffold group did not yield significantly better

in vivo results than those of the control group, which was mainly owing to denudation of the cartilage region of the scaffolds.[88]

A bi-layered type I collagen/TCP scaffold fabricated using DHT crosslinking had a Young's modulus of 1 MPa in the TCP layer, resulting in increased new bone formation in the TCP layer and fibrocartilage formation in type I collagen layer after 52 weeks of implantation in a pig model.[87] The resulting fibrocartilage in the type I collagen layer indicated that growth factors were required to achieve satisfactory hyaline cartilage regeneration. Another study reported the development of a bi-layered type I collagen scaffold using DHT crosslinking, which yielded a 34% hyaline cartilage repair effect after pre-seeding of BMSCs.[88] Consequently, an improved strategy was proposed with porous type I collagen in the upper layer and dense type I collagen in the bottom layer in combination with DHT crosslinking to achieve enhanced hyaline cartilage repair outcomes after pre-seeding of chondrocytes.[89] Furthermore, a bi-layered scaffold with type I collagen/CS in the upper layer and type I collagen/HAP in the bottom layer was fabricated using a co-precipitation method,[90, 91] which achieved a better OA repair effect than that achieved by PLGA scaffold after 26 weeks of in vivo implantation in a caprine model; moreover, the calcified cartilage layer was not observed. In addition, a bi-layered scaffold with HyA/type I collagen in the upper layer and HA/β-TCP in the bottom layer was fabricated using EGDGE layer-by-layer interface method (however, the interface did not work mechanically). A large defect was repaired with an International Cartilage Repair Society (ICRS) score of 8.7 in a rabbit model with pre-seeded chondrocytes, with no difference between cell-seeding and non-seeding groups, and displayed obvious residual HA/β-TCP scaffold.

Table 2.7 Bi-layered collagen scaffolds for osteochondral defect repair

Composition	Structure	Fabrication	Young's modulus	In vivo application	Outcomes	Ref
CI* TCP*	Bi-layer	DHT* crosslinking	1 Mpa (TCP*)	TCP layer significantly enhanced new bone formation in pigs after 52 weeks	Requires growth factor; fibrocartilage formation (T1 collagen)	[89]
CI	Bi-layer	DHT crosslinking	/	34% hyaline cartilage	Pre-seeded BMSCs	[90]
CI (porous) CI (dense)	Bi-layer	/	/	Hyaline-like cartilage	Pre-seeded chondrocytes	[91]
CI + CS CI + HAP	Bi-layer	Coprecipitation (no crosslinking)	/	Better than PLGA scaffold (caprine model, 26 weeks)	No calcified cartilage layer (middle layer)	[92, 93]
HyA* + CI HA + β-TCP	Bi-layer	EGDGE* layer-by-layer interface The interface didn't work mechanically	/	ICRS score of 8.7 Large defect repair in rabbit (diameter = 6, depth = 5 mm)	Pre-seeded chondrocytes Residual HA/β-TCP No noticeable difference between cell-seeding and non-seeding groups	

TCP* = β-tricalcium phosphate
EGDGE* = Ethylene glycol diglycidyl ether
HyA* = Hyaluroate
CI* = Collagen type I
CII* = Collagen type II

HAP* = Hydroxyapatite
DHT* = Dehydrothermal

Current progress in collagen scaffold development: Tri-layered and multi-layered scaffolds

The tidemark is defined by its location at the junction between pliant hyaline cartilage and the more rigid calcified tissue. The mechanical properties of this unique interface are fascinating and may be relevant to the pathogenesis of OA. Among existing concepts of the tidemark, one of the most persistent defines it to be a scar of the original, subchondral growth plate, which fits well with the fact that the tidemark initially develops when and where the growth plate ceases its development. Tidemarks are not seen in children but develop in all adults after puberty. In addition, the tidemark is unique as a normal, extracellular deposit of intracellular proteins (whose antigenicity may have been amplified via citrullination as part of apoptosis) and contains proinflammatory HMGB1 and DNA. If these proteins are recognised by the host immune system, progressive immune-mediated articular damage and destruction is the consequence.

Upward migration of subchondral bone was reported in 25–34% of patients after ACI[66, 67], and in vivo intra-articular implantation of grafts for osteochondral lesion repair has previously failed to restrict bone and vessel overgrowth into the cartilage region. This may lead to serious cartilage damage and early progression toward degenerative change.[94, 95] To prevent this, effective tidemark formation acts as a stable mechanical matrix and an integrated interface between the newly regenerated cartilage and subchondral bone.[96] Therefore, scientists began to introduce a

calcified cartilage layer (intermediate layer) in between the cartilage and subchondral bone layers to make tri-layered or multi-layered scaffolds.

Previous studies have successfully demonstrated that an intermediate osteochondral layer within scaffolds is beneficial for the restoration of the anatomical tidemark in rabbit and caprine joints.[12, 97] The interface between the cartilage and bone regions in the scaffold design contributes significantly to stabilising the mechanical integrity of multi-layered scaffolds. A recent study demonstrated that a compact interface layer of scaffolds contributed to the formation of ordered and uniformed neo-tidemark.[98] Considering the disadvantages of mono-layered and bi-layered scaffolds, increasing attention has been paid to the development of tri-layered and multi-layered scaffolds. In a study, a tri-layered scaffold composed of type I collagen/type II collagen/HyA in the upper layer, type I collagen/type II collagen/HAP scaffold in the middle layer and type I collagen/HAP scaffold in the bottom layer was developed using iterative laying method with EDC/NHS+DHT crosslinking. The resulting tri-layered scaffold was seamless but had no interface, with a Young's modulus of 0.3–0.4 kPa. It achieved ICRS grade II after 12 weeks of in vivo implantation, caused shrinking and delamination and had weak mechanical properties (as crosslinking was not effective) and poor cartilage repair owing to the use of type I collagen.[95, 97] Another study reported a tri-layered scaffold composed of type I collagen in the upper layer, type I collagen /HAP (40%) in the middle layer and type I collagen/HAP (70%) in the bottom layer using BDDE crosslinking. The scaffold resulted in bone regeneration without developing an immune response after 6 months of in vivo implantation in a horse model. However, press-fit or bio-glue led to delamination; therefore, fibrin glue was

used to prevent delamination in continuous passive motion experiments; in addition, fibrocartilage formation was observed.[84, 85]

Table 2.8 Tri-layered and multi-layered collagen scaffolds (layer ≥ 3) for osteochondral defect repair

Composition	Structure	Fabrication	Young's modulus	In vivo application	Outcomes	Ref
CI + CII + HyA CI + CII + HAP CI + HAP	Three layers	Iterative laying EDC/NHS+DHT crosslinking (seamless but no interface)	0.3–0.4 kPa	ICRS grade II (12 weeks)	Shrinking and delamination Weak mechanical properties (crosslinking was not effective) Poor cartilage repair (T1 Col)	[97, 99]
CI CI + HAP (40%) C1 + HAP (70%)	Three layers	Crosslinking (BDDE*)		Bone regenerative evidence was clear; immune response was not produced	Press-fit or bio-glue lead to delamination; fibrin glue was used to prevent delamination in continuous passive motion experiments; fibrocartilage	[86, 87]

				(horse, 6 months)	formation was observed	

CSMA* = Methacrylated chondroitin sulfate
PECDA* = Acryloyl chloride-poly(Ɛ-caprolactone)-poly(ethylene glycol)-poly(Ɛ-caprolactone)-acryloyl chloride
PEGDA* = Poly(ethylene glycol) diacrylate
BDDE* = 1,4-butanediol diglycidyl ether
CI = Collagen type I
CII = Collagen type II

We compared two recent relevant studies on tri-layered scaffolds (**Table 2.8**). Although the number of layers was increased to three, including the introduction of an intermediate layer, the two following critical issues remained prevalent:

1) Structural integration: Although the concept of designing a tri-layered scaffold was proposed[86, 87, 99], hard interfaces were not addressed because the fabrication method used in previous studies was layer-by-layer synthesis[99], i.e. fabricating three different layers separately and assembling them by knitting or using glue[86, 87]. As the layers were made separately without integration, they had different shrinking levels and delamination properties, which affected their tri-layered scaffold behaviour as a whole. An outstanding example is the tri-layered scaffold developed by E. Kon et al. in which a gap between the layers can be easily seen[86, 87] (**Figure 2.7)**.

2) Composition: Although collagen II is the dominating type of collagen in the natural cartilage of animals, collagen I was used to make scaffolds for cartilage repair in previous studies. Moreover, in some studies [97, 99], although type II collagen was introduced to make the cartilage layer, type I collagen was used to reinforce the mechanical properties. However, type I collagen did not provide an ideal

environment for chondrogenic differentiation and hence reduced the final quality of regenerated cartilage and calcified cartilage (fibrocartilage formation was observed).

Therefore, structural integration and composition of cartilage are important aspects for tri-layered scaffold improvement, which may lead to better osteochondral repair outcomes.

Figure 2.7 Fabricated tri-layered collagen scaffold [86, 87] demonstrating different levels of shrinkage and a clear gap between layers.

2.5 Basis and aims of this study

This study was based on the scaffold manufacturing and fabrication techniques developed at the Biomaterial Group, Department of Materials, University of Oxford. The raw collagen material was extracted and purified by the Collagen Research Group of the Veterans Affairs Medical Centre Research Service, University of Tennessee.

The literature search revealed that although significant progress has been made to replace homogenous scaffolds with tri-layered and multi-layered scaffolds, the critical limitations of currently developed multi-layered scaffolds are as follows:

1) Composition

Type I collagen is still widely used in the cartilage layer of scaffold production. Its use is controversial because the natural component in the human body is type II collagen,

which is the only predominant collagen type. Therefore, incorrect composition of the scaffold matrix can be one of the factors misleading cell differentiation.

An insoluble, naturally fibrillar form of collagen is most commonly used. Extensive crosslinking of this type of fibre can lead to batch-to-batch variations, and the presence of telopeptides can lead to antigenicity.

2) Structure and mechanical properties

Although multi-layered scaffolds have been introduced in some studies, integration between layers was hardly observed. Hard interfaces resulted in delamination and hence affected the clinical outcome.

3) Osteochondral repair quality in vivo

Owing to the factors mentioned in 1) and 2), the quality of repair was not ideal in previous studies. To date, in most studies, the outcome was reported to be a relatively low ICRS score. Therefore, in this study, we proposed a novel scaffold design to address the concerns regarding both material composition and structure to achieve a better in vivo outcome. **Figure 2.7** represents a schematic demonstration of the proposed design of the integrated tri-layered scaffold with the correct collagen type, mimicking the composition and structure of the natural osteochondral joint.

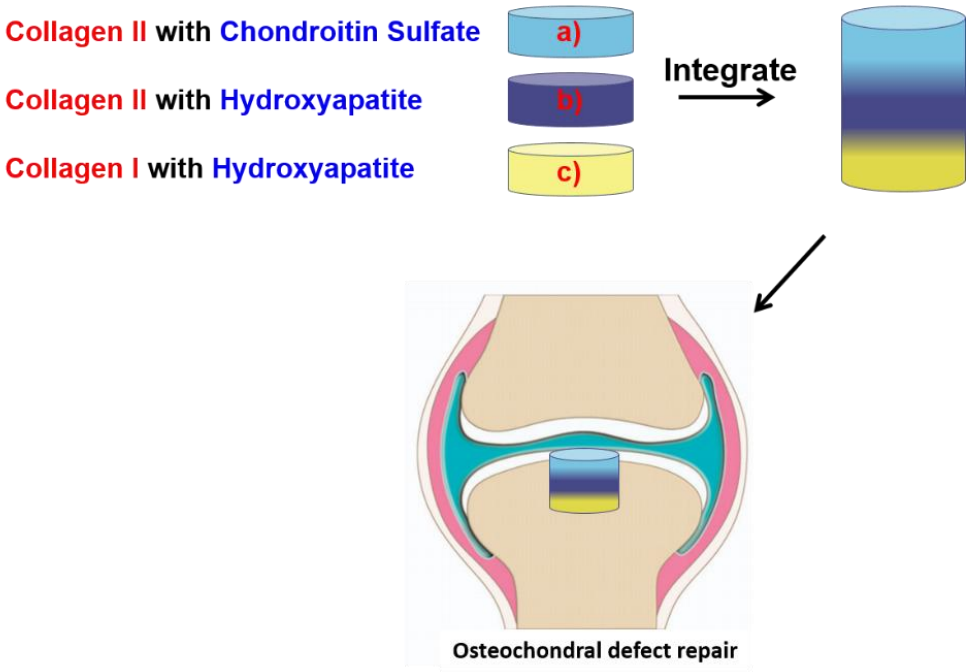

Figure 2.7 Schematic representation of the designed tri-layered collagen scaffold with gradient interfaces for osteochondral tissue repair. The collagen scaffold comprises three components: a) cartilage layer/top layer: type II collagen with chondroitin sulfate, b) calcified cartilage layer/intermedium layer: type II collagen with 70% hydroxyapatite, c) bone layer: type I collagen with 80% hydroxyapatite.

The principal aims of this study were as follows:

1) To develop an integrated tri-layered scaffold with gradient interfaces and correct collagen components according to the natural composition and structure of osteochondral joint using atelocollagen type II and type I and other major components of extracellular matrix (i.e. HAP and CS) to enhance the mechanical and biological function of the scaffold

2) To examine the structure, microstructure, mechanical properties and biological repair outcomes of the designed scaffold (in vitro and in vivo)

Chapter 3. Material synthesis, fabrication and characterisation

3.1 Introduction

Scaffolds with the correct cartilage and bone matrix composition can introduce desirable microenvironmental signals that may direct desirable cell differentiation and result in good repair outcomes. In addition, when fabricating multi-layered scaffolds, introducing soft/gradient interfaces between the layers may prevent delamination or mechanical failure under in vivo conditions after the scaffold is implanted.

In this chapter, Section 3.2 explains the experimental procedure for scaffold fabrication (Section 3.2.1 and 3.2.2). Various characterisation techniques were used to validate the structural information and mechanical properties of the fabricated scaffolds, including FTIR (Section 3.2.3), SEM (Section 3.3.4), EDX spectroscopy (Section 3.2.5) and micro-CT (Section 3.2.6). The results are presented in Section 3.3 and discussed in Section 3.4. A summary of the findings is detailed in Section 3.5.

3.2 Method

3.2.1 Synthesis of the required materials

Synthesis of COL II/CS suspensions (for the cartilage/top layer)

Both COL I and II monomers were provided by the Veterans Affairs Medical Center. Tris-buffered saline (TBS) solution [50-mM tris-(hydroxymethyl)-aminomethane, 150-mM sodium chloride, pH=7.4], EDC/NHS solution (60-mM EDC and 30-mM NHS) were purchased from Sigma-Aldrich, UK. A monomeric COL II suspension (1% by weight) was prepared by dissolving 0.5-g COL II monomers in 50 mL of acetic acid solution (pH=3.2). The suspension was then homogenised for 1 min at 4°C in a

conventional blender; this step was performed twice to obtain a uniformly dispersed suspension of COL II monomers. The suspension was then mixed with 10 mL of TBS solution and incubated at 37°C for 1 h to achieve a fibrillar COL II suspension.

The fibrillar COL II suspension was mixed with CS in a 1:1 (w:w) ratio and 200 mL of ethanol/water (50% v/v) solution with EDC/NHS for 24 h to create a COL II/CS suspension via crosslinking. Finally, the COL II/CS suspension was washed twice with 0.1-M Na_2HPO_4 in deionised water (DW), the pH of the final suspension was adjusted to 3.5 and the solution was stored at 4°C until it was used for scaffold fabrication.

Synthesis of COL II/HAP suspension (for the calcified cartilage/intermediate layer)

A fibrillar suspension of COL II was prepared, crosslinked and washed using the same procedure as mentioned in the previous sub-section. This suspension was subsequently homogeneously mixed with HAP powder (particle size < 50 nm) in a 3:7 (w:w) ratio using a conventional blender to obtain the COL II/HAP suspension. The pH of the final suspension was adjusted to 3.5, and the suspension was stored at 4°C until it was used for scaffold fabrication.

Synthesis of COL I/HAP suspension (for the bone/bottom layer)

A fibrillar suspension of COL I was prepared, crosslinked and washed using the same procedure as mentioned in sub-section 3.2.1. This suspension was homogeneously mixed with HAP powder (particle size < 50 nm) in a 4:1 (w:w) ratio using a conventional blender to obtain the COL I/HAP suspension. The pH of the final suspension was adjusted to 3.5, and the suspension was stored at 4°C until it was used for scaffold fabrication.

3.2.2 Fabrication of mono-layered and tri-layered scaffolds

Mono-layered scaffolds were fabricated by pouring each of the three suspensions into plastic moulds, freezing them at -20°C and freeze-drying them overnight to remove water.

The integrated tri-layered scaffolds were fabricated using a method called liquid-phase co-synthesis, in which all scaffold compartments were formed simultaneously. Briefly, 1 mL of each suspension was poured into a mould in the following order: COL I/HAP in the bottom layer, COL II/HAP in the middle layer and COL II/CS in the top layer. The layered suspensions were allowed to undergo interdiffusion at room temperature for 5 min before being chilled at -20°C and freeze-dried overnight. The additional processing step at room temperature creates a zone of interdiffusion that extends across different interfaces between the suspensions.

To fabricate a control for the tri-layered scaffold, a slightly modified version of a previously published protocol called layer-by-layer method was used. Briefly, the COL I/HAP suspension (bottom layer) was poured into the mould and frozen overnight; subsequently, the COL II/HAP suspension was poured into the mould on top of the frozen COL I/HAP suspension and frozen overnight to create the intermediate layer. Finally, the COL II/CS suspension was poured and frozen overnight, and the resulting tri-layered frozen suspension was freeze-dried.

The scaffolds fabricated as mentioned above were immersed in ethanol and DW to remove acetic acid and then refrozen and freeze-dried again.

3.2.3 Fourier-transform infrared spectroscopy

The samples were analysed in the infrared absorption mode in a Varian FTIR spectrometer, UMA600, (Palo Alto, CA, USA) over a range of 4000–500 cm^{-1} with a resolution of 2 cm^{-1}. Results were recorded as the average of 64 scans for each sample with the background scan removed. The spectra were analysed using essential FTIR (Operant, LLC., FL, USA).

3.2.4 Scanning electron microscopy

Scaffold morphology was characterised by SEM using a ZEISS EVO machine operating at an accelerating voltage of 10 kV. Specimens were sectioned with a sharp blade, and the cross-sections were examined. Owing to some difficulties in the charges of HAP + collagen samples, a backscattered electron (BSE) detector under variable pressure mode was used; this method did not require the specimens to be coated. We used the image analysis software ImageJ to analyse pores, calculate microstructural dimensions of SEM micrographs and calibrate scale bars. For pore size distribution measurements, the micrographs were converted into black and white images (black representing the pores and white representing the material) by adjusting the threshold set by comparing with a non-converted image.

3.2.5 Energy-dispersive X-ray spectroscopy

EDX spectroscopy is used to measure the elemental composition (such as the content of calcium, phosphate and sulfur) of a sample. The tri-layered scaffolds were analysed using EDX spectroscopy to visualise pore microstructures and determine relative distributions of minerals throughout the scaffolds, especially at the interface between

two layers. Line scans and compositional map data were acquired for regions between the layers.

3.2.6 Micro-computed tomography

The microarchitecture (13 mm in diameter and 17 mm in height) and porosity of the scaffolds were analysed using micro-CT. The thickness of each layer of the tri-layered scaffold was quite even (approximately 5–6 mm) owing to the manufacturing process. Approximately 2000 images of each scaffold were taken from different angles (1600 projections). ImageJ was used to calculate the porosity of the scaffold, and three-dimensional (3D) models were reconstructed using the Avizo software.

To calculate porosity, thresholding was performed, followed by binarisation, and porosity was determined using the image volume method by adding the porosity pixels of all analysed images and dividing that value by the sum of the areas observed on these images. The obtained value was multiplied by 100%.

3.2.7 Statistical analyses

Analysis of variance (ANOVA) was performed using the SPSS software for each experiment. Post-hoc Bonferroni correction was performed for all multiple comparisons. Results were considered significant at $P < 0.05$. If the data were non-normal, the Greenhouse–Geisser correction values for ANOVA were used.

3.3 Results

3.3.1 SEM and FTIR

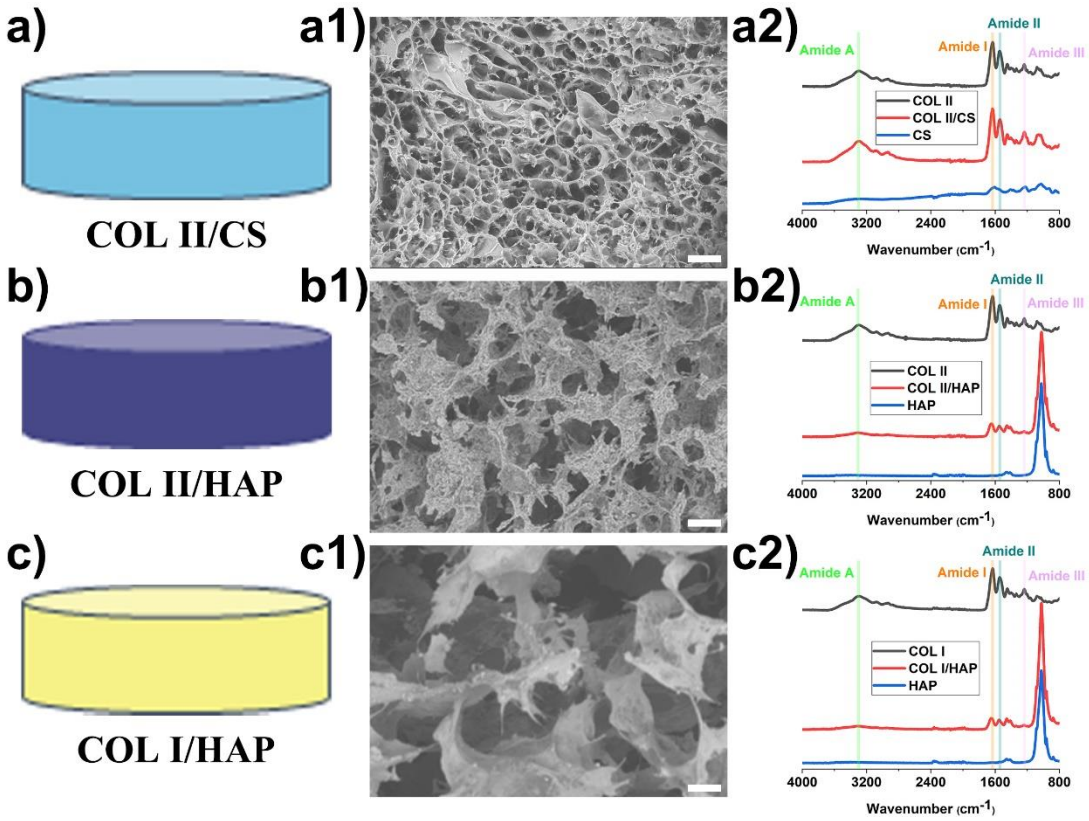

Figure 3.1 SEM images and FTIR spectra of COL II/CS (top layer), COL II/HAP (intermediate layer) and COL I/HAP (bottom layer) (scale bar = 100 μm).

SEM micrographs were obtained to examine the internal (cross-sectional) structures of the scaffold. SEM characterisation of the three layers is illustrated in **Figure 3.1**. SEM images were acquired on an EVO SEM system. The results revealed that each layer of scaffolds had high degree of interconnectivity and a uniform pore microstructure.

Figure 3.1 (a2) shows the FTIR spectra of crosslinked COL II, COL II/CS and CS samples. The addition of CS to COL II only caused minor shifts to the amide A peak (3300–3296 cm^{-1}), amide I peak (1631–1633 cm^{-1}), amide II peak (1544–1545 cm^{-1}) and amide III peak (1235–1234 cm^{-1}). No significant changes (>5 cm^{-1}) were observed.

The small vibration peak reflecting the CH_2 side chain, an important characteristic feature of collagen, was identified in both collagen type II (1336 cm^{-1}) and collagen type II + CS (1338 cm^{-1}) samples. However, this peak was not seen in the FTIR spectrum of CS. A shift of the characteristic peak from 1078 cm^{-1} in the spectrum of COL II to 1029 cm^{-1} in the spectrum of COL II/CS was observed. This characteristic peak was also found in the spectrum of pure CS, which was considered the carbohydrate peak (approximately at 950–1100 cm^{-1}) [100, 101]. Moreover, there was an increase in the carbohydrate peak (amide I peak height). The peak increase and peak shift indicated the chemical bonding between COL II and CS.

Figure 3.1 (b2) shows the FTIR spectra of crosslinked COL II, COL II/HAP, and HAP samples. Addition of HAP to COL II caused a significant decrease in the amide A peak from 3310 cm^{-1} to 3315 cm^{-1} and amide I peak from 1632 cm^{-1} to 1645 cm^{-1}, which was also observed in a previous study conducted in our laboratory [102]. No significant changes (>5 cm^{-1}) were observed in the amide III peak. The small vibration peak reflecting the CH_2 side chain (1338 cm^{-1}) remained unchanged and was not seen in the FTIR spectrum of HAP. Peaks reflecting PO_4^{3-} were observed in HAP (1022 cm^{-1}) and COL II/HAP (1026 cm^{-1}) samples, which indicated the presence of HAP and the bonding between HAP and COL II.

Figure 3.1 (c2) shows the FTIR spectra of crosslinked COL I, COL I/HAP and HAP samples. Addition of HAP to type I collagen caused a significant decrease in the amide A peak from 3306 cm^{-1} to 3315 cm^{-1}, amide I peak from 1631 cm^{-1} to 1645 cm^{-1} and amide II peak from 1537 cm^{-1} to 1548 cm^{-1}, which was also observed in a previous

study conducted in our laboratory [102]. No significant changes (>5 cm^{-1}) were observed in the amide III peak and the small CH_2 side-chain peak. The CH_2 side-chain peak was not seen in the FTIR spectrum of HAP. Peaks reflecting PO_4^{3-} were seen in HAP (1022 cm^{-1}) and COL I/HAP (1026 cm^{-1}) samples, indicating the presence of HAP and the bonding between HAP and COL I.

Table 3.1 FTIR spectroscopic analysis for characterising the functional groups.

	ColT2 (cm^{-1})	**ColT2 + CS (cm^{-1})**	**CS (cm^{-1})**	**Ref**
Amide A	3300	3296	3298	[16][103]
Amide I	1631	1633	1606	[18, 22]
Amide II	1544	1545	1568	[18, 22]
CH_2 side chain	1336	1338	/	[18, 20, 21]
Amide III	1235	1234	1225	[18, 22]
Carbohydrate	1078	1029	1024	[15, 21]
PO_4^{3-}	/	1022	1026	[13]

3.3.2 EDX

EDX spectroscopy was used for the quantitative analysis of the two upper layers (cartilage and intermediate) of the scaffold.

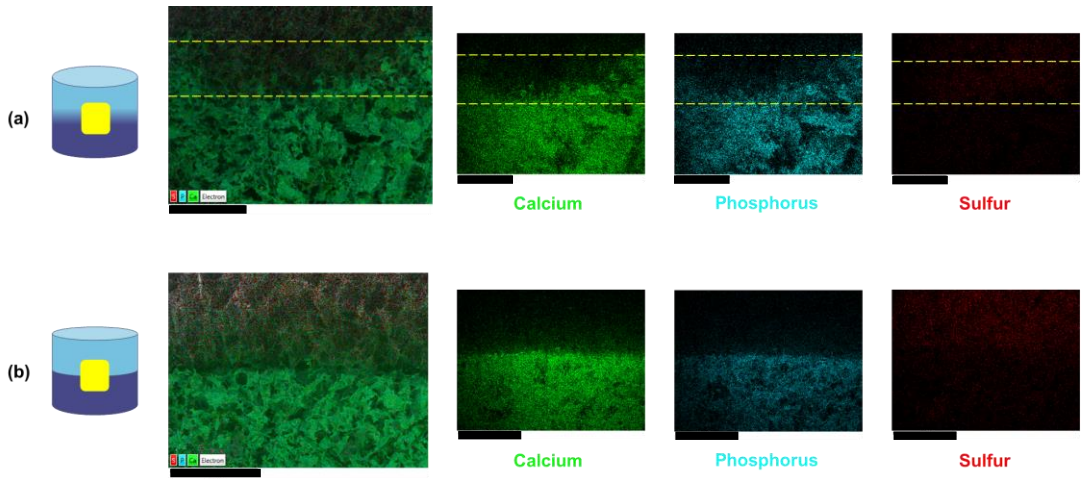

Figure 3.2 Energy dispersive X-ray (EDX) analysis via map scan for three elements (calcium, phosphorus and sulfur) of the osteochondral scaffolds at the cartilage–calcified cartilage layer transitional phase. Map scans of the bi-layered scaffold (cartilage and calcified cartilage layers) in (a) experimental group with integrated scaffold with interface and (b) control group without integration and interface (scale bar = 1 mm). (The control group scaffolds were fabricated as described in Section 3.2)

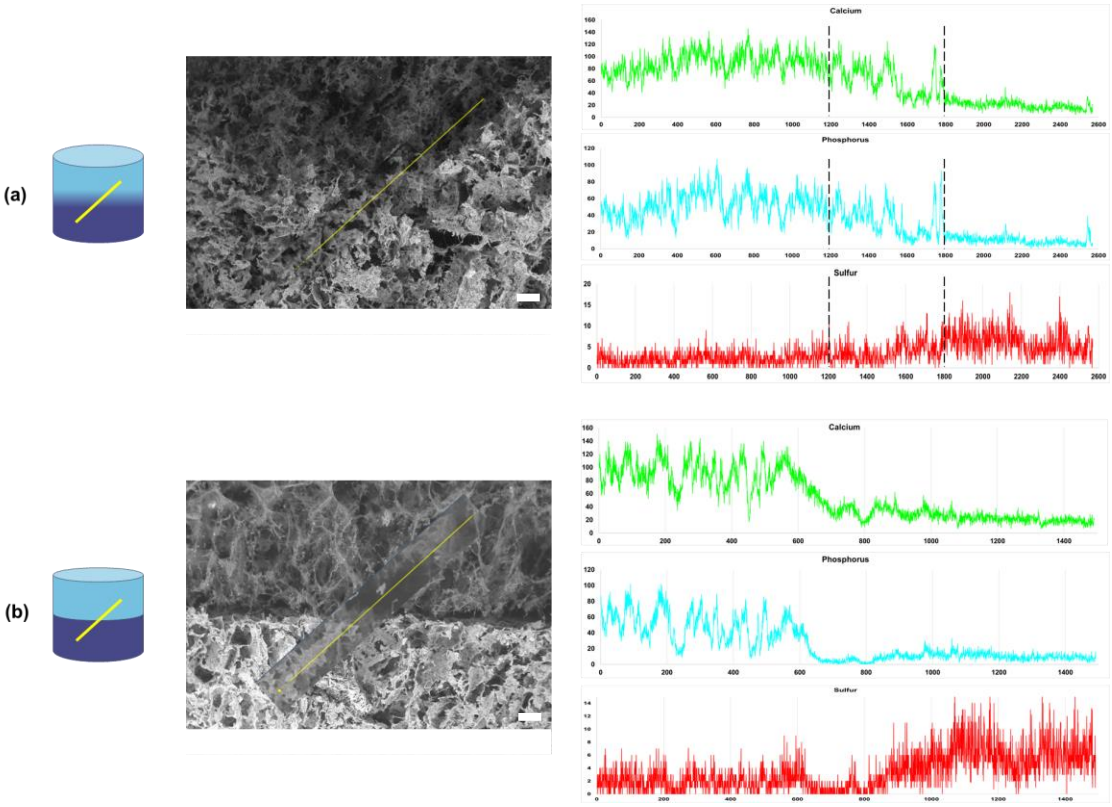

Figure 3.3 Energy dispersive X-ray (EDX) analysis via line scan for three elements (calcium, phosphorus and sulfur) of the osteochondral scaffolds at the cartilage–calcified cartilage layer transitional phase. X-axis: 0–2400 μm (a) and 0–1300 μm (b); Y-axis: atomic counts, scale bar = 200 μm.

EDX map scan analysis (**Figure 3.2a and 3.2b**) of the transition regions of the bi-layered scaffolds (both experimental and control groups) revealed distinct mineralised (high content of Ca and P) and unmineralised (low/no content of Ca and P) regions within the scaffold corresponding to the known locations of the cartilage and calcified cartilage layers. Furthermore, as shown in **Figure 3.2a**, no abrupt, hard interface was observed between the two layers; instead, an interfacial zone was created, in which the cartilage and calcified cartilage layers mixed to change the gradient elemental composition. However, such an interfacial zone was not observed in the control group (**Figure 3.2b**). In the control group, a distinct gap between the cartilage and calcified cartilage layers was observed, with no interfacial penetration of Ca and P between the two layers. Therefore, an abrupt, hard interface was observed in the control group.

EDX line scans revealed additional quantitative characteristics. **Figure 3.3a** shows a line scan region of 2400 μm across the two layers. An interfacial region of 614.33 (±10.23) μm was identified (approximately from 1200 to 1800 μm) in all three elemental scans. However, the control group (**Figure 3.3b**) did not show such an interfacial region, and a very sharp decrease in Ca and P was observed at approximately 600 μm. In addition, the content of sulfur showed an increase at approximately 800 μm instead of 600 μm, indicating a gap between 600 and 800 μm.

<u>Interface distance between the two lower layers</u>

After characterising the interface of the upper two layers (cartilage and calcified cartilage layers) via EDX spectroscopy, we further analysed the interface of the bottom two layers (calcified cartilage and subchondral bone layers) via SEM.

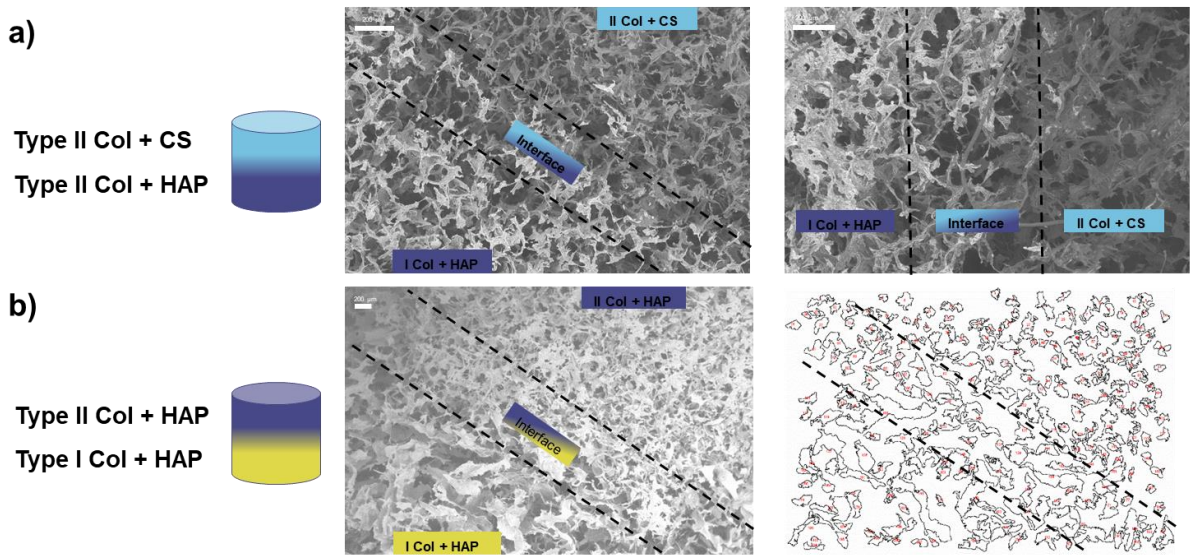

Composites	Average Pore Size
Type II Col + HAP	137(±49) µm
Interface	110(+37) µm
Type I Col + HAP	97(+25) µm

Figure 3.4. SEM micrographs of the bi-layer scaffolds. (a) Cartilage and intermediate layers, (b) Intermediate and bone layers. ImageJ was used to create the pore size distribution graphs and measure the pore size (scale bar = 200 µm).

In the bi-layered scaffold (calcified cartilage and subchondral bone layers), three distinct zones were observed: COL I + HAP, interface and COL II + HAP (**Figure 3.4**). The pore size was larger in COL II + HAP than in COL I + HAP.

The interfacial zone thickness was also measured using ImageJ based on the SEM images shown in **Figure 3.4** and was consistent with the results of EDX spectroscopy (**Figure 3.3**).

Table 3.2 Measurement of interface distance based on SEM images using ImageJ

Resource	Average thickness of the interfacial zone (µm) (n = 3)
Figure 3.16a	644
Figure 3.16b	710

3.3.3 Micro-CT imaging of tri-layered scaffolds

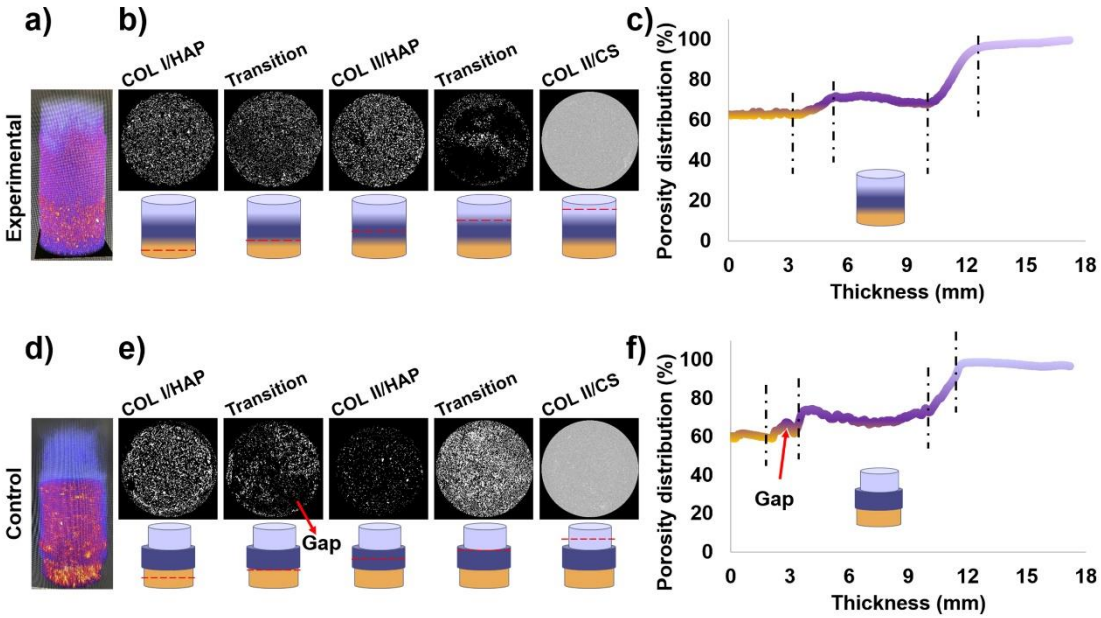

Figure 3.5 Micro-CT imaging of the tri-layered scaffolds in both experimental and control groups. (a and d) Qualitative restructuration: intensity mapping; (b and e) Micro-CT images of each layer and the two transition zones; (c and f) Porosity distribution curves from bone to cartilage.

Qualitative analysis: Three-dimensional visualisation of the scaffolds

The reconstructed scaffold models are shown in **Figure 3.5a** and **3.5d**. Different materials interact differently with X-rays, leading to dissimilar absorption of X-rays and different signals. Therefore, the three layers of the scaffold can be distinguished because they consist of materials with different atomic numbers (layers with calcium are heavier than layers with only collagen and CS). As shown in **Figure 3.5a** and **3.5d**, the three layers were coloured differently: light purple (top layer with COL II and CS), purple and yellow (some regions) (intermediate layer with COL II and HAP) and red–yellow (bottom layer with COL I and HAP).

Qualitative analysis: Interface penetration

In the experiment group (**Figure 3.5a**), the two transition regions (one region between the cartilage and middle layers and another between the middle and bottom layers) were inter-penetrated because we used a liquid-phase co-synthesis method[104] for manufacturing the scaffold. Therefore, in the transition zone, the two components mixed to form a gradient structure.

However, the transition zones were not seen in the control group scaffolds (**Figure 3.5d**) because each layer was frozen and freeze-dried separately as opposed to the simultaneous assembly in the liquid-phase co-synthesis method.

Qualitative analysis: Shape (shrinkage)

On comparing the shape of the two 3D reconstructed scaffolds, we observed that the shape of the scaffolds was more uniform in the experimental group (**Figure 3.5a**) than in the control group. The diameter of the three layers of the scaffold in the experimental group was similar, indicating that the three layers shared a similar degree of shrinkage after freeze-drying. However, in the scaffolds of the control group (**Figure 3.5d**), the top layer had a shorter diameter than that of the middle layer. Furthermore, the transition region between the middle and bottom layers showed a distinct ‘ring-like’ edge, indicating a sudden change in diameter, which was not observed in the scaffolds of the experimental group.

Quantitative analysis: Micro-CT imaging and porosity distribution

Quantitative analysis including micro-CT images and porosity distribution curves is demonstrated in **Figure 3.5c** and **3.5f**.

The average porosity of the scaffolds in the experimental group was 62.9%, 70.1% 98.2% for the bone, middle and cartilage layers, respectively. The average porosity of the scaffolds in the control group was 60.5%, 70.2% and 97.6% for the bone, middle and cartilage layers, respectively. No difference was observed in the porosity of the three layers between the experimental and control groups because the three layers essentially had the same composition.

However, two differences were observed in the two transition zones. The first difference was that the thickness of the transition zones (illustrated in the curves in **Figure 3.5c** and **3.5f**) was larger in the experimental group than in the control group. In the experimental group, the thickness of the transition zone between the bone and middle layers was 2.54 mm, and that between the middle and cartilage layers was 2.66 mm. However, in the control group, the thickness of the transition zone between the bone and middle layers was 1.82 mm, and that between the middle and cartilage layers was 1.77 mm. Moreover, the microstructure of the transition zones was different. On comparing the transition zone between the bone and middle layers (**Figure 3.5b** and **3.5e**, the second micro-CT image), we observed that the cross-section from the control group showed some empty regions where the material of the bone layer was missing and the material of the middle layer was hardly present. However, a good mix of the two components was observed in the scaffolds of the experimental group. Therefore, a sudden decrease in porosity was observed in the curves of the control group, which was called a ‘gap’ (**Figure 3.5e and 3.5f**). In the transition zone between the middle and cartilage layers (**Figure 3.5b** and **3.5e**, the fourth micro-CT image), no decrease in the pore size was observed in the corresponding curve. The possible reason for the absence of a ‘gap’ in this transition zone was that the porosity of the

cartilage layer was low (98.2 %) and hence a ‘gap’ could not contribute to a change in porosity.

3.4 Discussion

This study was based on the existing expertise of our research group in developing collagen-based scaffolds. We developed a novel tri-layered collagen scaffold for osteochondral repair. The designed scaffold contains three distinct regions to repair the damaged cartilage, calcified cartilage and subchondral bone simultaneously. Collagen formed the base material for each layer of this tri-layered construct, thus offering the advantage of the presence of natural binding sites and the ability to degrade without releasing harmful products. By combining these biocompatible characteristics, integrated techniques and mechanical properties, this novel multi-layered scaffold with different composition in each layer has the potential to offer an off-the-shelf cell-free approach for early-stage OD repair.

Scaffold fabrication

As mentioned in Section 3.2.1, after synthesising the scaffold suspensions, pH was adjusted back to 3.5, which helped to improve the shape of the scaffold. The ability of collagen to form a homogeneous liquid with water is highly dependent on the ability of its amino acids to interact with water molecules. Because collagen is an amphoteric molecule, which contains both amine and carboxylic acid groups, it cannot be dispersed or solubilised in deionised water at room temperature (pH = 6–7, 25°C). The pH of deionised water at room temperature is close to the isoelectric point (pI) of collagen, at which point amino acids have no net charge (neutral zwitterion state).[105,

106] **Figure 3.6** illustrates how an acidic environment induces protonation of the charged carboxylic acid group (COO^-) to result in a positively charged ion with a stabilised carboxylic acid group (COOH). The collagen molecules then interact with water molecules. The pH of an adequately homogenised collagen suspension is approximately 3–3.5. A negatively charged ion may be formed after exposure to an alkaline environment, again allowing interaction with water. However, it requires a highly alkaline environment (pH > 12) to form a homogenised collagen solution because the pI of collagen is approximately 9.3,[107] which makes dissolving collagen in an alkaline environment more difficult. Moreover, a highly alkaline environment may alter the native structure of collagen.[108, 109]

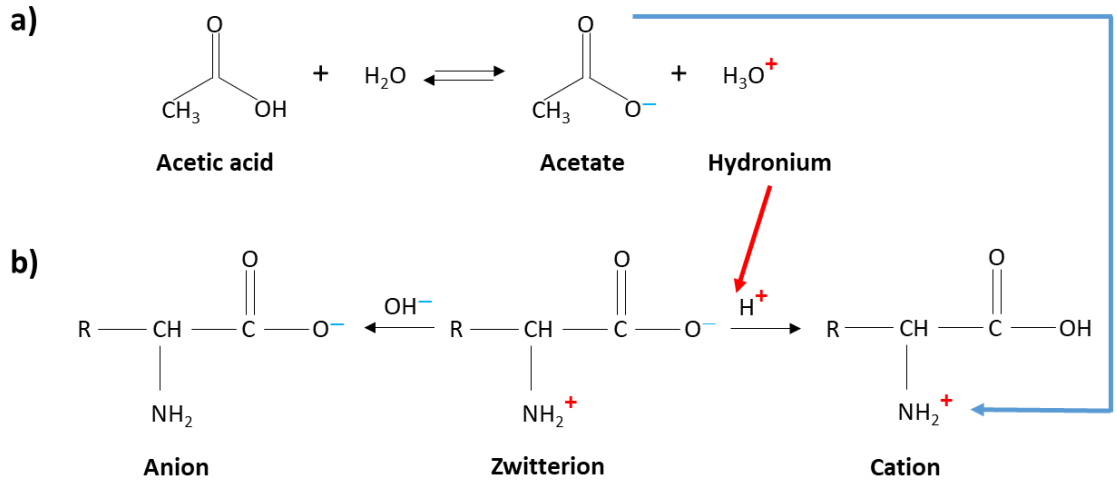

Figure 3.6 a) Disassociation of acetic acid in water; b) Ionic states of amino acids lead to the formation of a positive ion in acidic conditions and a negative ion in alkaline conditions. The red arrow indicates proton donation by hydronium to the carboxylic group, and the blue arrow indicates possible ionic salt formation between the acetate and cations of amino acids.

Blending procedure

Blending was performed when lyophilised collagen resisted water uptake (swelling) under acidic conditions. The rationale for this additional blending step is described below.

In dilute acetic acid suspension, diffusion/swelling of collagen is governed by the difference in osmotic pressure between non-diffusible ions present on solid collagen and diffusible ions present in the acidic solution. According to Wilsons, acetate ions absorbed by collagen tend to diffuse into the surrounding solution to equilibrate the concentration between two phases.[110] However, these acetate ions may form salts with amino acid cations (blue arrow in **Figure 3.6**) and hence prevent diffusion into the solution without dragging them along, which is hindered by intermolecular cohesion forces and the elasticity of the collagen triple helix. Therefore, blending may help to reduce this cohesive effect by enhancing COO^- protonation of amino acids via increased exposure to acidic solution. When a large number of proton-captured cations are formed, the electrostatic repulsion between the similarly charged groups allows for additional association with free water molecules as the structure is partially disorganised (**Figure 3.7**) and water flows into the capillary spaces.

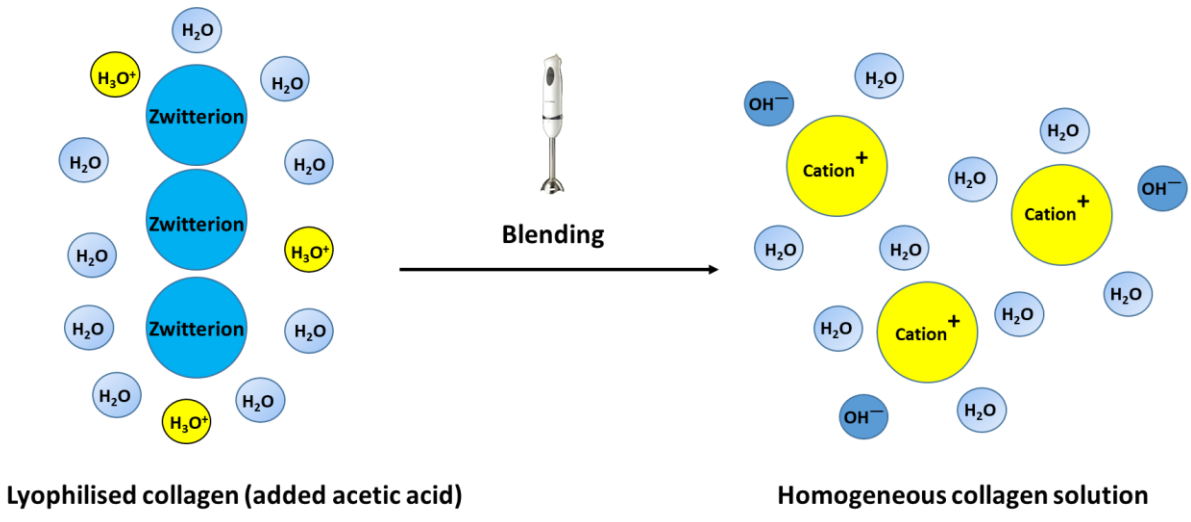

Figure 3.7 Blending lyophilised collagen in an acetic acid solution to help the dissolution of solid material and produce a homogenous collagen solution.

FTIR

Amide A, amide I, amide II and amide III functional groups

Amide A, amide I, amide II and amide III peaks were observed in all samples, confirming that the polypeptide structure was maintained after chemical synthesis and material fabrication. Amide A, amide I and amide II had the strongest infrared absorption owing to N-H stretching (amide A), C=O stretching (amide I) and a combination of C-N stretching and N-H bending (amide II).[81, 111] Because both collagen II and CS have aforementioned bonding, amide I and amide II peaks of the spectrum were affected by both collagen and CS. Absorption at the amide III peak (1235 cm^{-1}) was more complicated and related to the combination of C-N stretching, N-H bending and C-C stretching.[101]

CH_2 side chain

The absorption peak at 1336 cm^{-1} corresponded to the small CH_2 side-chain vibration (wagging) peak. The side chain of proline of collagen contributes the most to this peak.[112] This peak is an important characteristic feature of collagen, which is not seen in a pure CS spectrum.

Interaction between CS and collagen

Absorption in the carbohydrate region (approximately 950–1100 cm^{-1}) is mainly related to the stretching vibrations of C-O and C-OH and C-C ring vibrations. Although both collagen and CS contain these vibrations, the region is believed to be more specific towards CS.[100, 101] The peak at 1024 cm^{-1} shown in **Figure 3.1** may correspond to C-O stretching vibrations of CS.[113]

Moreover, there was an increase in the carbohydrate peak (amide I peak height) from 1078 cm^{-1} to 1029 cm^{-1} (CS had the carbohydrate peak at 1024 cm^{-1}). The peak increase and peak shift both indicated the bonding between CS and type II collagen. The proposed chemical reaction mechanism for crosslinking collagen and CS is illustrated in **Figure 3.8**. It was deduced that the amino acid of collagen was essentially reacting with the carboxylic acid of CS via EDC/NHS crosslinking.

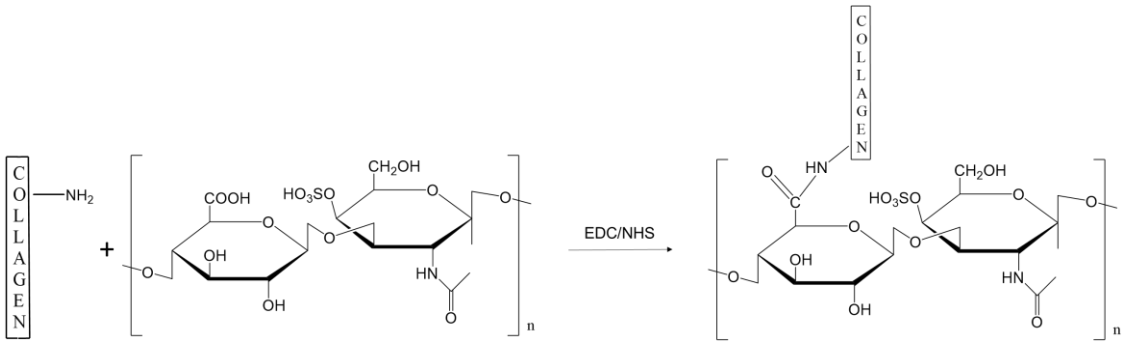

Figure 3.8 Schematic demonstration of the chemical mechanism of EDC/NHS crosslinking of collagen and chondroitin sulfate. Adapted from [105][114]

Interaction between HAP and collagen

Collagen is an ideal target for calcium and phosphate ions originating from HAP. Addition of HAP resulted in a shift in the position of the amide I peak in both collagen type I and collagen type II composites.

Two chemical reactions are illustrated in **Figure 3.9**, which may explain the less tightly coiled triple helix and the resulting weakening of the C=O bond. Therefore, a shift to lower frequencies was observed after the mineralisation of type I and type II collagen.

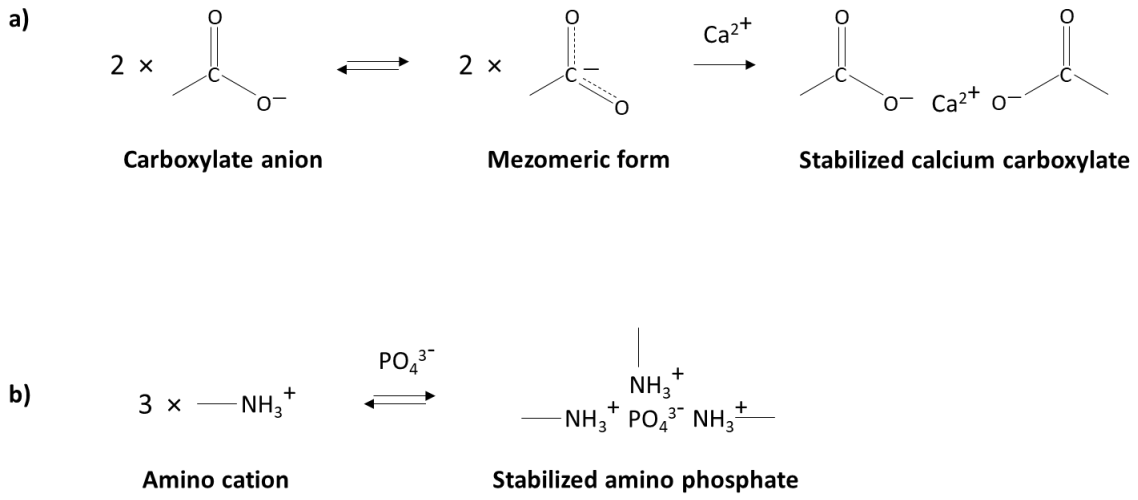

Figure 3.9 a) Interaction and bond formation between carboxylate anion (collagen) and calcium (HAP), adapted from [107][115]; b) Interaction and bond formation between amino cation (collagen) and phosphate (HAP).

Microstructure evaluation (SEM)

Appropriate scaffold pore size for cell growth

The acceptable scaffold pore size range for promoting the growth of chondrocytes is 50–300 µm [116]. The acceptable scaffold pore size for promoting the growth of osteoblasts is in the range of 100–600 µm.[11, 117] The recommended pore size for osteogenesis is 100 µm; however, a study by Itala [118] illustrated that osteoblasts can grow in scaffolds with small pores (50 µm) as well. Considering the size of bone cells (10–20 µm), the pore size range of 50–300 µm is suitable for both chondrogenesis and osteogenesis.

3.5 Summary

In this chapter, we successfully fabricated a novel osteochondral device, which was characterised by several techniques to reveal three dedicated layers for cartilage, calcified cartilage and bone repair with gradient interfaces.

In conclusion, the main findings are summarised as follows:

1. The structural information including morphology and chemical bonding for the crosslinking of each layer of the tri-layered scaffold was confirmed by several characterisation techniques.
2. The tri-layered scaffolds were fabricated following a liquid-phase co-synthesis method. The interfaces between each layer were characterised by EDX spectroscopy; these interfaces were not seen in the scaffolds of the control group that were made using a layer-by-layer method.
3. A ‘gap’ was observed in the control scaffolds as determined based on the porosity distribution evaluated using ImageJ, which was not observed in the designed scaffolds.

Therefore, we confirm that we have successfully designed a tri-layered scaffold with interfaces between layers.

Subsequently, we aimed to prove that the tri-layered scaffold was mechanically strong enough to survive during surgery and in an in vivo environment.

Chapter 4. Mechanical studies

4.1 Introduction

To assess the potential clinical applications of the tri-layered scaffold, we investigated its mechanical properties. The scaffold should withstand the external force generated by a surgeon during press-fitting and by internal loading during the movement of joints. The mechanical behaviour of the scaffold in both dry and wet states under compression, tensile force and delamination is discussed in this chapter.

The experimental procedure is illustrated in Section 4.2. The compression test (Section 4.2.1) was performed to test whether the scaffolds can withstand the press-fitting force. The tensile (Section 4.2.2) and delamination tests were performed to assess where and how much force was needed to delaminate the scaffold, which is an important mechanical property. The results are demonstrated in Section 4.3 and are discussed in Section 4.4. A summary of the main findings is detailed in Section 4.5.

4.2 Method

4.2.1 Compression

The compression test was performed using a dynamic mechanical analyser (DMA, PerkinElmer) to measure the Young's modulus of the scaffold. Disc specimens (approximately 11 mm in diameter and 12 mm in height) were prepared, and four samples were tested for each layer of the scaffold. For the wet compression test, scaffold samples were immersed in phosphate-buffered saline (PBS). The test was performed using a load cell of 2.6 N at a rate of 50 mN/min (approximately 2.5% strain rate per minute).

4.2.2 Tensile strength

The tensile strength of each layer was determined using a custom-designed interfacial strength test rig fitted to DMA as described by Levingstone.[99] The rig design allows for secure fixation of the scaffold during testing while ensuring the correct alignment of the scaffold between the load cell and base platen of the machine. Scaffold samples (approximately 11 mm in diameter and 12 mm in height) were adhered to a carbon adhesive tab using a high-viscosity adhesive (super glue) and inserted into the rig for testing. The high viscosity of the adhesive ensured minimal integration into the scaffold, which was confirmed by applying the adhesive to the scaffold and inspecting the depth of penetration after sectioning. Samples were tested using a 1-N load cell tensile force at a rate of 50 mN/min (approximately 2.5% strain rate per minute). The Young's modulus of scaffolds was calculated according to the obtained strain–stress curves.

4.2.3 Delamination adhesion test

The interfacial adhesion strength between the layers of the integrated scaffolds was determined using a custom-designed interfacial strength test rig fitted to DMA, as described by Levingstone.[99] The rig design allowed for secure fixation of the scaffolds during the test while ensuring the correct alignment of the scaffold between the load cell and base platen of the machine. Scaffold samples were adhered to a carbon adhesive tab using a high-viscosity adhesive (super glue) and inserted into the rig for testing. The high viscosity of the adhesive used ensured minimal integration into the scaffolds, which was confirmed by applying the adhesive to the scaffolds and inspecting the depth of penetration following sectioning. Samples were tested using 1-N load cell tensile force at a rate of 500 mN/min (approximately 25% strain rate per minute). Failure was expected to occur either at the ultimate tensile strength of one of

the component layers of the scaffolds or as a result of delamination at the layer interfaces. The scaffolds were 11 mm in diameter and 12 mm in height.

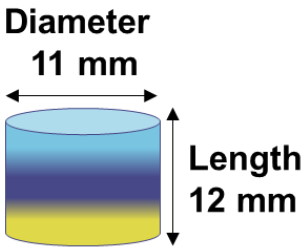

Figure 4.1 Diameter and length of the scaffold sample for mechanical testing.

4.2.4 Measurement of the shrinkage level

The shrinkage level was determined using the following equation:

Shrinkage level = volume of the scaffold / volume of the empty space of the mould x 100%

$$\text{Volume of the scaffold } = \pi(\frac{d}{2})^2 h$$

d is the diameter of the actual scaffold, and h is the height of the actual scaffold.

$$\text{Volume of the empty space of the mould } = \pi(\frac{D}{2})^2 \text{H}$$

D is the inner diameter of the mould, and H is the height of the mould.

$$\text{Therefore, shrinkage level } = \pi(\frac{d}{2})^2 h \,/\, \pi(\frac{D}{2})^2 \text{H} = \frac{d^2 h}{D^2 H}$$

4.3 Results

4.3.1 Compression

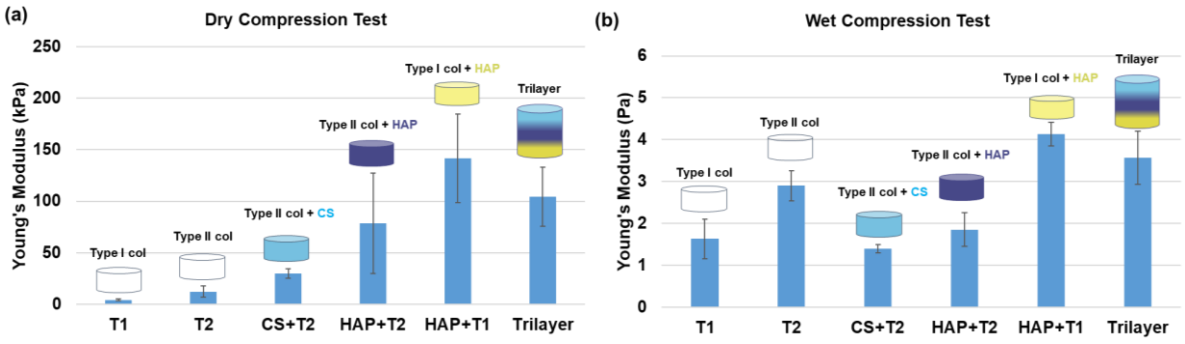

Figure 4.2 Young's modulus calculated from the compression tests of the mono-layered and integrated tri-layered scaffolds under (a) dry and (b) wet conditions.

The Young's modulus calculated from the compression tests is shown in **Figure 4.2**. Under dry compressive conditions (**Figure 4.2a**), the bone layer (COL I + HAP) was found to have the highest compressive Young's modulus (142 kPa), which was significantly higher than that of the calcified layer (COL II + HAP, 78 kPa). This was attributed to the higher content of HAP in the bone layer than in the calcified cartilage layer (collagen:HAP = 1:4 in the bone layer and 3:7 in the calcified cartilage layer). The cartilage layer (COL II + CS) had the lowest modulus of only 30 kPa. A similar increasing trend in the Young's modulus was observed under wet compressive conditions (**Figure 4.2b**) from the top cartilage layer to the bottom bone layer. However, the exact modulus of these layers significantly reduced under wet conditions compared with that under dry conditions and was 1.40 kPa, 1.86 kPa and 4.14 kPa (cartilage, intermediate and bone layer, respectively).

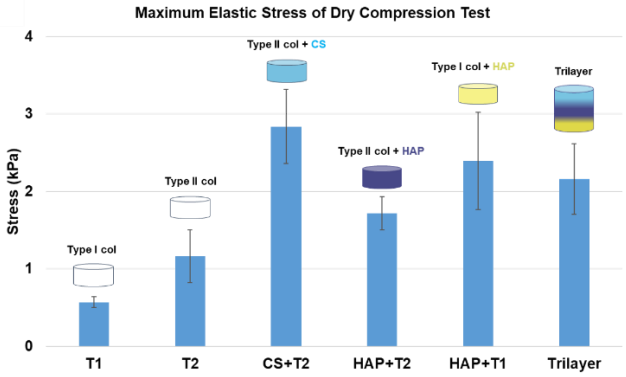

Figure 4.3 Maximum elastic stress calculated from compression tests of the mono-layered and integrated tri-layered scaffolds.

Figure 4.3 illustrates the maximum elastic stress for all scaffolds. It was observed that pure collagen had the smallest elastic compression stress (stress = 0.57 kPa for type I collagen and 1.16 kPa for type II collagen). After CS and HAP were added to collagen, elastic stress was increased (stress = 2.84 kPa for CS + T2 collagen, 1.72 kPa for HAP + T2 collagen and 2.39 for HAP + T1 collagen). The maximum elastic stress for the tri-layered scaffold was 2.16 kPa.

4.3.2 Tensile strength

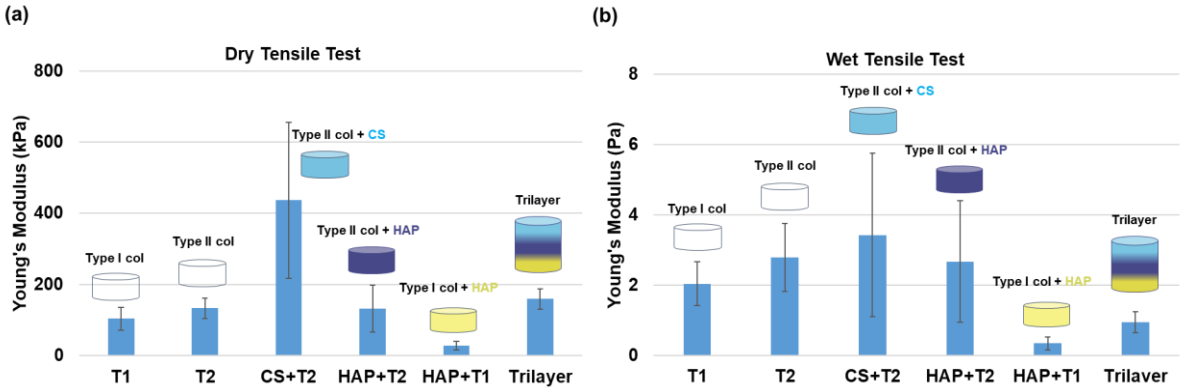

Figure 4.4 Tensile strength of the mono-layered and integrated tri-layered scaffolds under (a) dry and (b) wet conditions.

Changes in tensile strength were opposite. Under dry conditions (**Figure 4.4a**), the bone layer (HAP + T1) was found to have the lowest Young's modulus of 27.8 kPa,

which was significantly lower than that of the intermediate layer (HAP + T2) with a modulus of 178.6 kPa. The highest Young's modulus was observed in the cartilage layer (CS + T2) with a modulus of 577.7 kPa. Under wet conditions (**Figure 4.4b**), the intermediate layer (HAP + T2) was found to have the highest modulus (9.74 kPa) followed by the cartilage layer (CS + T2) with a modulus of 4.10 kPa. The bone layer (HAP + T1) was found to have the lowest modulus (only 0.54 kPa).

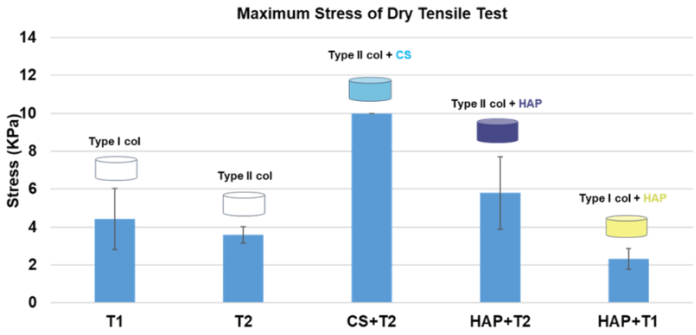

Figure 4.5 (a) Maximum stress and (b) maximum strain calculated from tensile tests of the mono-layered and integrated tri-layered scaffolds.

Figure 4.5a demonstrates the pattern of maximum stress of the tensile test, which was quite different from that of the compression test (**Figure 4.5a**). For pure type I and II collagen, the maximum stress was 4.43 kPa and 3.59 kPa, respectively. The maximum stress for HAP + collagen was 5.80 kPa (HAP+T2) and 2.33 kPa (HAP+T1). The maximum stress for CS + T2 collagen was undetermined but surely larger than 10 kPa (beyond the maximum measurement range of our machine).

4.3.3 Effects of CS

Crosslinking of CS to type II collagen enhanced mechanical strength in both compression and tensile tests. Based on the previous results (**Section 4.3.1 and 4.3.2**), the effect of CS on the mechanical properties of scaffolds was analysed as shown in **Figure 4.6**.

In compression tests, as illustrated in **Figure 4.6c and 4.6d**, two interesting observations were made. First, the compression modulus increased two-fold after the addition of CS. Second, the ultimate strain of scaffolds made of pure type II collagen was larger than that of the scaffolds made of type II collagen and CS (48% versus 45%, respectively), which indicated that under the same ultimate static force (1100 mN), the scaffold with pure type II collagen was compressed more than the scaffold with type II collagen and CS.

As illustrated in the bottom two graphs in **Figure 4.6e and 4.6f**, the tensile modulus of the scaffolds made of type II collagen and CS was 4 times as large as that of the scaffolds made of pure type II collage.

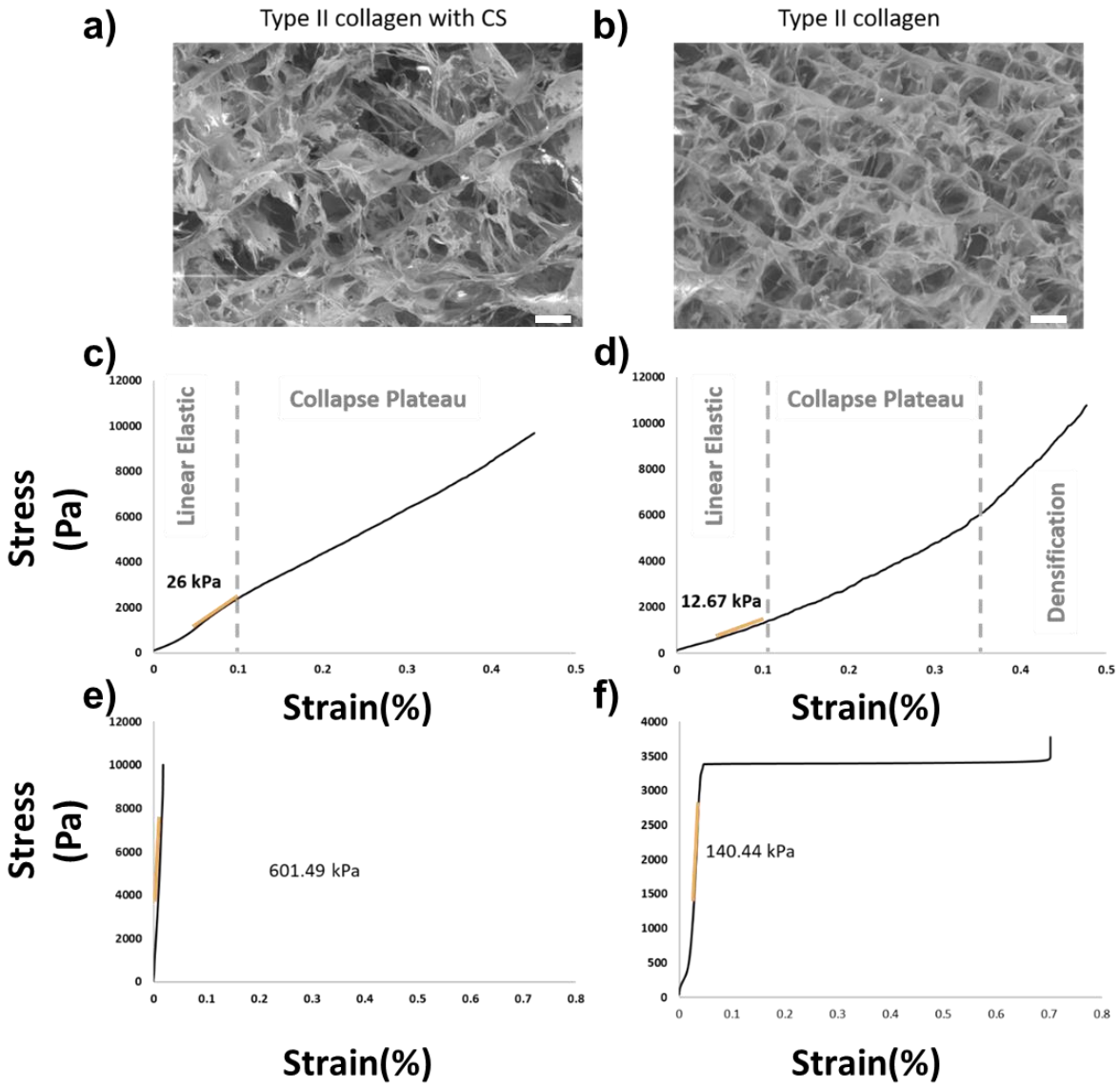

Figure 4.6 SEM images (a and b), compression stress–strain curves (c and d) and typical tensile stress–strain curves (e and f) of the scaffold composed of type II collagen and CS and the scaffold composed of pure type II collagen (scale bar = 100 μm).

The Young's modulus of the scaffolds depends on three critical factors as follows[119]:

1) Relative density of the sponge

2) A constant related to the pore geometry

3) Elastic modulus of struts (solid materials that scaffolds are made from)

For the tri-layered scaffold designed in this study, the relative density of the two sponges is mentioned below:

	Type II collagen scaffold	Type II collagen + chondroitin sulfate (CS) scaffold
Relative density ($\frac{\rho_{scaffold}}{\rho_{solid}}$)	0.017	0.028

The increase in relative density (nearly double, from 0.017 to 0.028) contributes significantly to the larger Young's modulus of the scaffolds made of type II collagen and CS. Increasing the amount of the matrix materials may enhance mechanical properties. However, some other factors might have contributed to the increased Young's modulus because the modulus of type II collagen in both compression and tensile tests was larger than that of 2% pure type II collagen (data not shown).

According to SEM analysis, the geometry of the scaffolds did not change significantly (**Figure 4.7**). Therefore, we speculated that the increase in strut strength was a result of variations in composition (addition of CS) and enhanced fibre strength owing to bond formation between CS and collagen. In addition, fibre thickness was increased. The average wall thickness of type 2 collagen + CS was almost 3 times that of pure type 2 collagen.

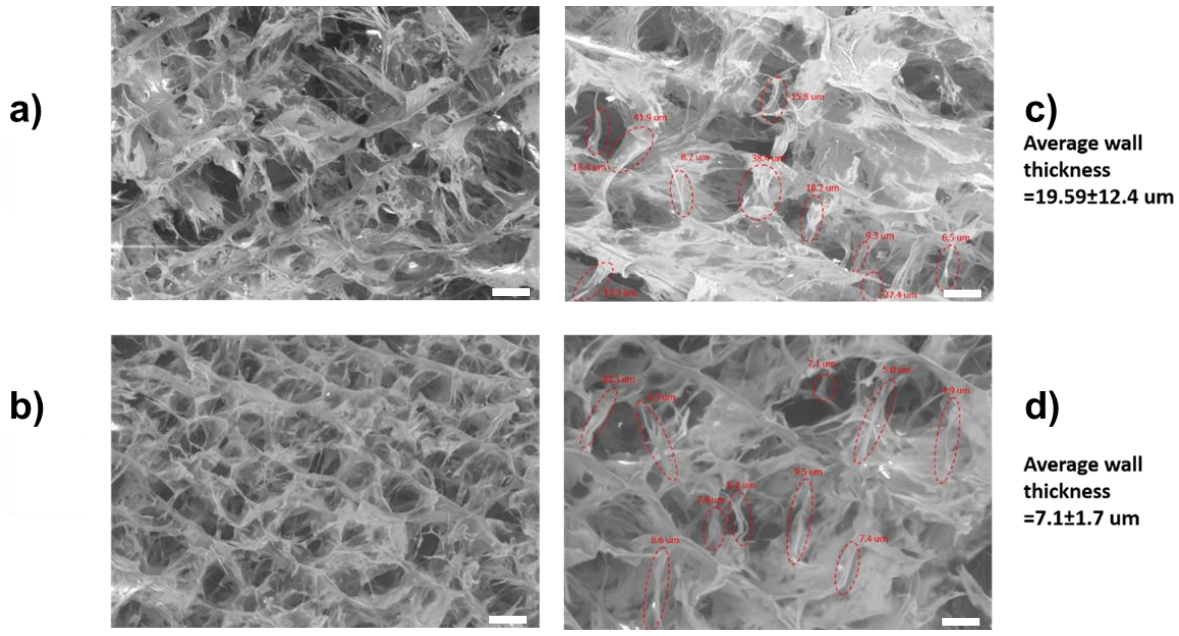

Figure 4.7 Comparative study on a) scaffolds made of type II collagen with CS and b) scaffolds made of pure type II collagen. c) and d) are the magnified images of a) and b) (scale bar = 100 μm).

In conclusion, the addition of CS enhanced the mechanical property of almost every parameter in both compression and tensile tests. In the compression test, the modulus of the scaffold was doubled after the addition of CS. In the tensile test, the modulus of the scaffold with type II collagen and CS increased nearly 3-fold as that of the scaffold with pure collagen, and more importantly, the maximum tensile stress increased from 3.59 kPa to 10 kPa.

4.3.4 Effects of HAP

HAP is the main component of the bone mineral phase. It is a ceramic bone-conductive material, which is composed of calcium, phosphorus, oxygen and hydrogen. Its molecular formula is $Ca_{10}(PO_4)_6(OH)_2$. The ratio of calcium to phosphorus in human bones is 1.67:1. HAP is a non-plastic material with a hexagonal biconical crystal

structure. Owing to its biological stability, biocompatibility and bioactivity, HAP has been widely used in the biomedical field. The mechanical behaviour of HAP and the speed and quality of bone integration depend on the size, pore size, porosity and interconnection of crystals.[120] The effect of HAP on the collagen matrix was much stronger than that of CS. SEM (**Figure 4.8**) demonstrated that all three factors contributing to mechanical strength were changed dramatically after adding HAP to the collagen matrix (relative density of the sponge, pore geometry and elastic modulus of struts[101]).

The relative density of the scaffolds increased after HAP was added.

	Type II collagen scaffold	Type II collagen scaffold with HAP	Type I collagen scaffold	Type I collagen scaffold with HAP
Relative density $(\frac{\rho_{scaffold}}{\rho_{solid}})$	0.017	0.023	0.018	0.0214

The geometry of scaffolds was changed after HAP was added. As shown in **Figure 4.8**, the circularity of the scaffolds decreased after HAP was added to both type I and type II collagen, and the scaffold matrix resulted in a more elongated and sheet-like structure. This change in geometry was also discovered and reported in a study by Kane,[121] in which histological sections and SEM micrographs of freeze-fractured scaffolds showed a highly elongated linear pore structure. In addition, in HAP whisker-reinforced scaffolds, the freezing process appeared to preferentially align whiskers in the direction of ice crystal propagation along the mechanical loading axis. All scaffolds contained numerous transverse cross-struts bridging the elongated pores; however,

their morphology varied depending on the HAP reinforcement weight fraction and morphology. Cross-struts in unreinforced scaffolds appeared thin and rope-like. Scaffolds reinforced with HAP powder contained small HAP particles incorporated into the cross-struts. However, cross-struts in HAP whisker-reinforced scaffolds were thicker, and the pore space was often bridged by HAP whiskers.

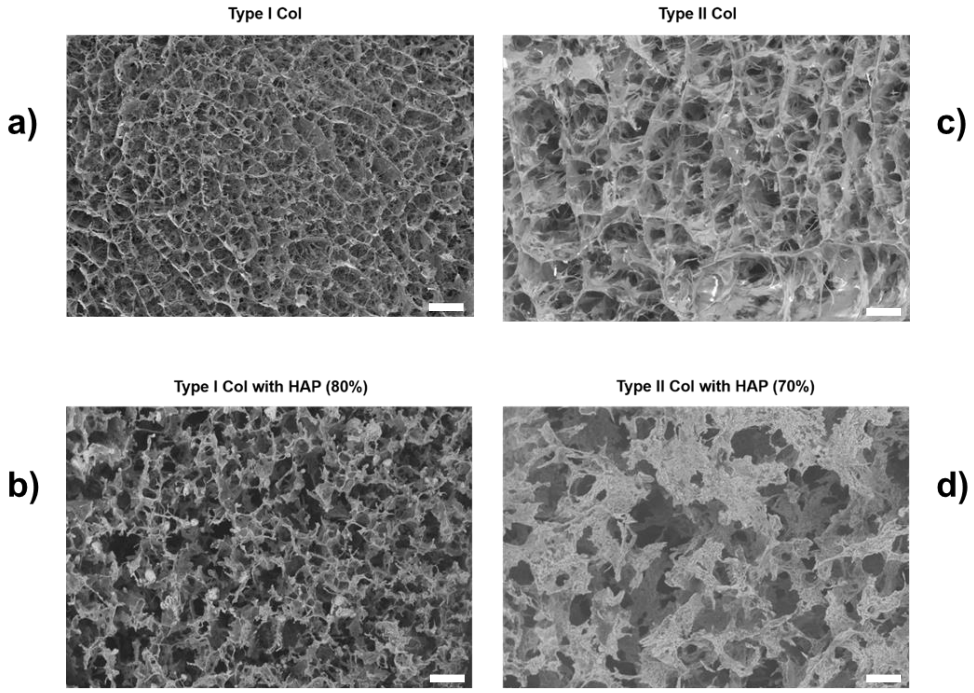

Figure 4.8 Comparative SEM images of scaffolds composed of collagen and HAP and those composed of pure collagen. a) and c) SEM images of pure type I collagen and type II collagen scaffolds, respectively. b) and d) SEM images of scaffolds composed of type I collagen and HAP and those composed of type II collagen and HAP, respectively (scale bar = 200 μm). These images are a part of the data presented in **Section 3.3.1.**

Furthermore, the elastic property of the struts changed after HAP was added to the collagen matrix. HAP is known to strongly interact with collagen.[122] Therefore, we speculated that fibre strength was enhanced owing to the bond formation between HAP and collagen. In addition, HAP clusters (**Figure 4.9**) contributed to the increase in compression modulus owing to repulsion. However, these HAP clusters did not

affect tensile strength after they were separated from each other but contributed to the decrease in tensile modulus.

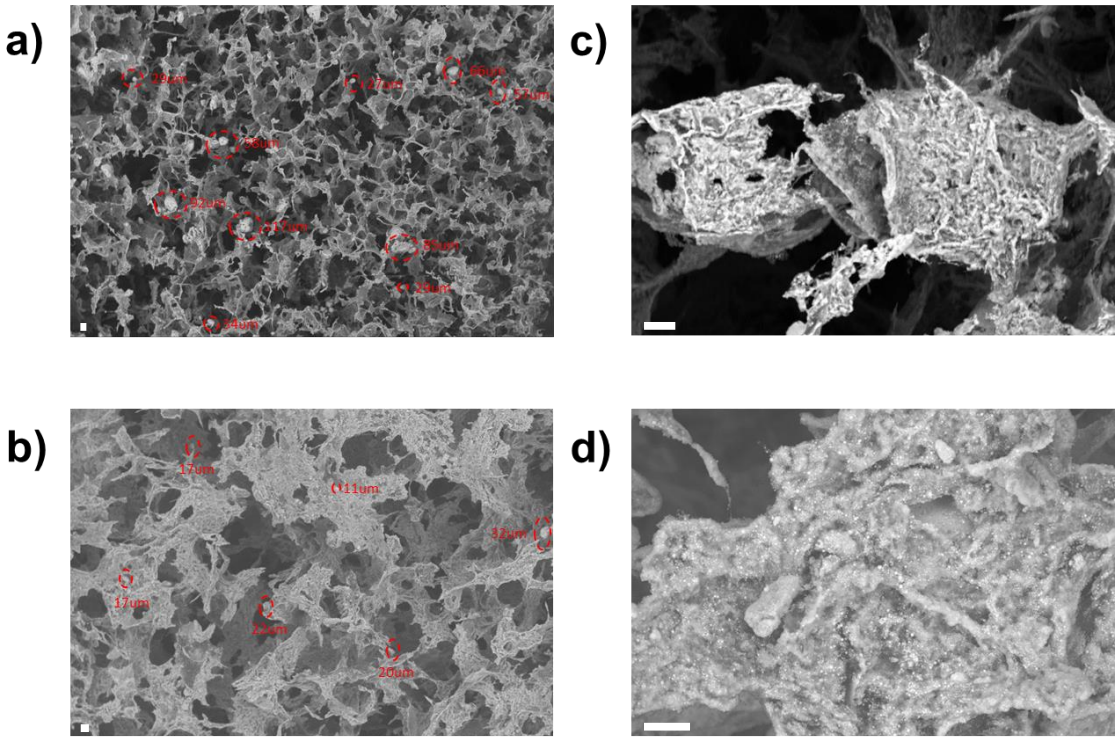

Figure 4.9. Observation of HAP clusters (red circle with diameter). a) SEM image of the bone layer made of collagen type I and 80% HAP; b) SEM image of the calcified cartilage layer made of collagen type II and 70% HAP. c) and d) are the magnified images of a typical HAP cluster in a) and b), respectively (scale bar = 20 μm). These images are a part of the data presented in **Section 3.3.1**.

4.3.5 Delamination testing of the bi-layered and tri-layered scaffolds

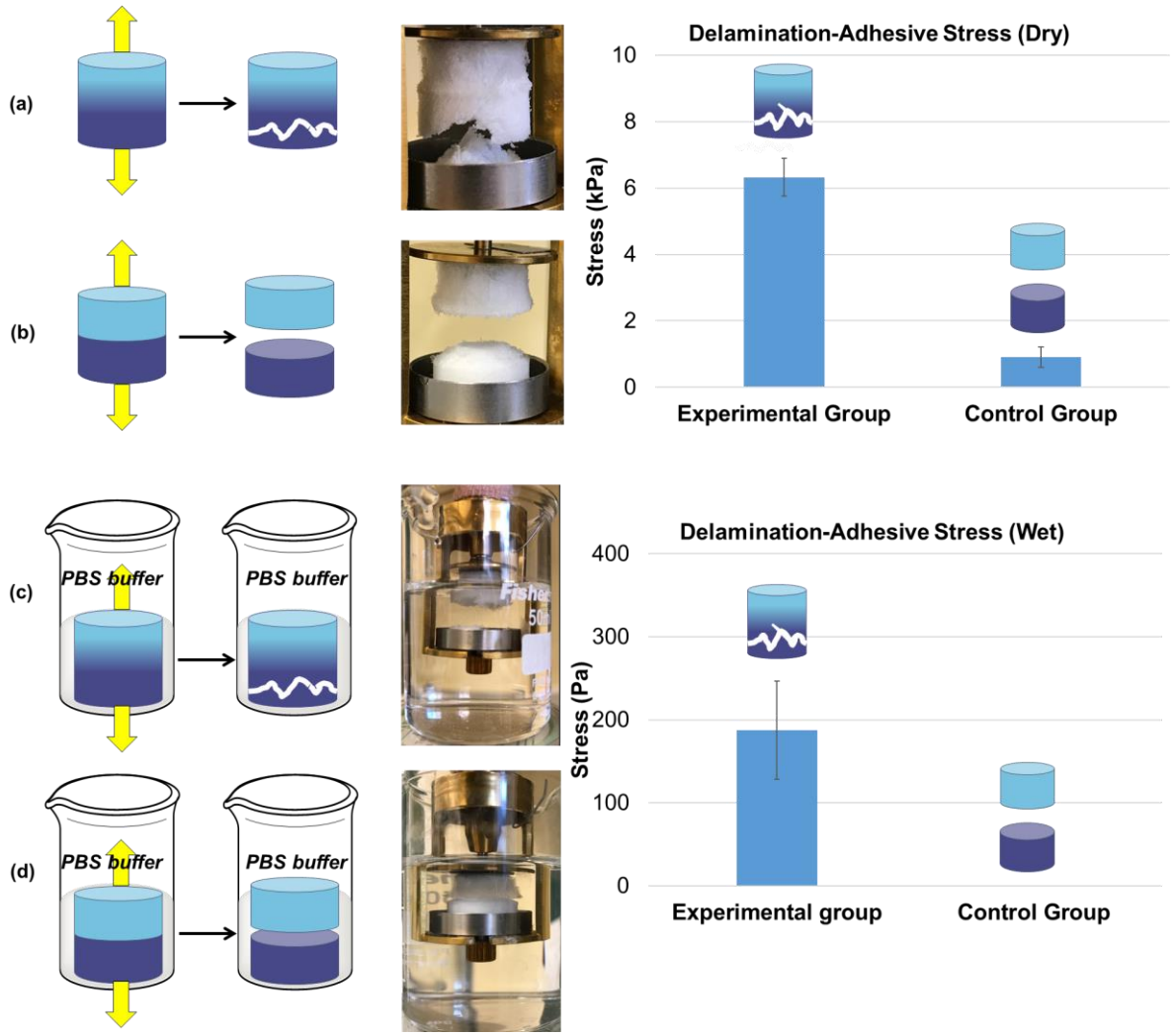

Figure 4.10 Delamination test of the bi-layered scaffolds (cartilage and intermediate layers), including the illustration of delamination of the bi-layer scaffolds and their ultimate stress at failure. a) and c) Scaffolds from the experimental group under dry and wet conditions. b) and d) Scaffolds from the control group under dry and wet conditions.

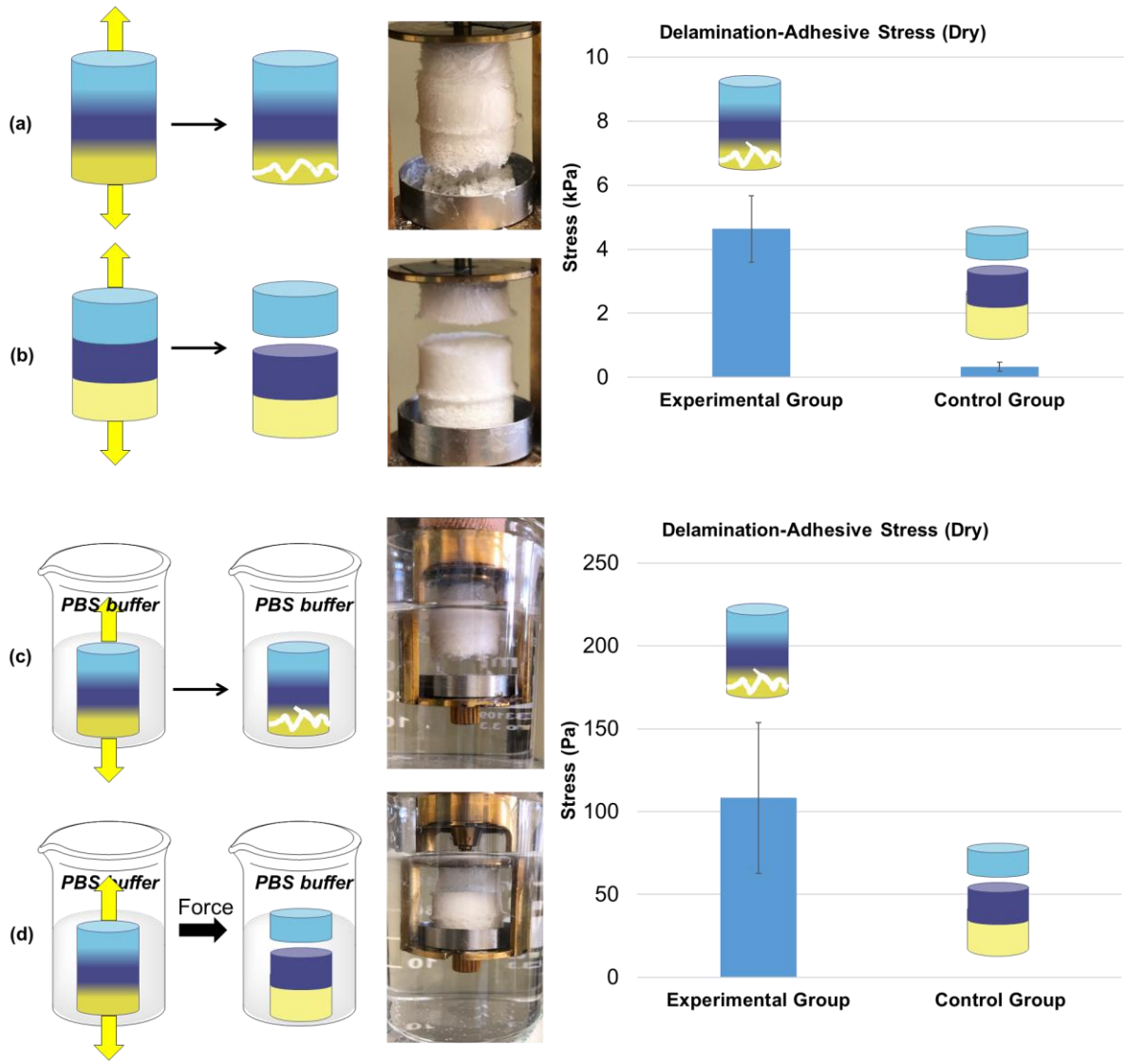

Figure 4.11 Delamination test of the tri-layered scaffolds, including an illustration of delamination of the tri-layered scaffolds and their ultimate stress at failure. a) and c) Scaffolds from the experimental group under dry and wet conditions. b) and d) Scaffolds from the control groups under dry and wet conditions.

Delamination of different layers was not seen in the experimental group. Under dry conditions, failure occurred within the intermediate layer in the bi-layer scaffold (6.32 kPa, **Figure 4.10a**) and within the bone layer in the tri-layered scaffold (4.64 kPa, **Figure 4.11a**), suggesting that interfacial strength was more significant than the strength of individual layers. Under wet conditions, failure occurred at a much lower modulus within the cartilage layer in the bi-layered scaffold (187.7 Pa, **Figure 4.10c**) and within the bone layer in the tri-layered scaffold (108.2 Pa, **Figure 4.11c**).

However, interfacial delamination of different layers was observed in the control group. Failure always occurred at the interface under both dry (0.57 kPa [**Figure 4.10c]** for the bi-layered scaffold and 0.33 kPa [**Figure 4.11c**] for the tri-layered scaffold) and wet conditions (the interfacial layers were separated immediately after they were immersed in PBS).

Moreover, the mechanical performance of the bi-layered scaffold was better than that of the tri-layered scaffold, that is, higher failure stress was observed under dry and wet conditions in both experiment and control groups. This was because the bi-layered scaffold did not contain the compartment with weak tensile strength, that is, the bone layer. In the bi-layered scaffold, delamination occurred at the intermediate layer, that is, the calcified cartilage layer, whereas in the tri-layered scaffold, it occurred at the bone layer. In addition, the maximum tensile stress of the intermediate layer was larger than that of the bone layer (5.80 kPa versus 2.33 kPa, respectively, in the dry state and 906.34 Pa versus 178.82 Pa, respectively, in the wet state).

4.3.6 Shrinkage levels in six types of scaffolds

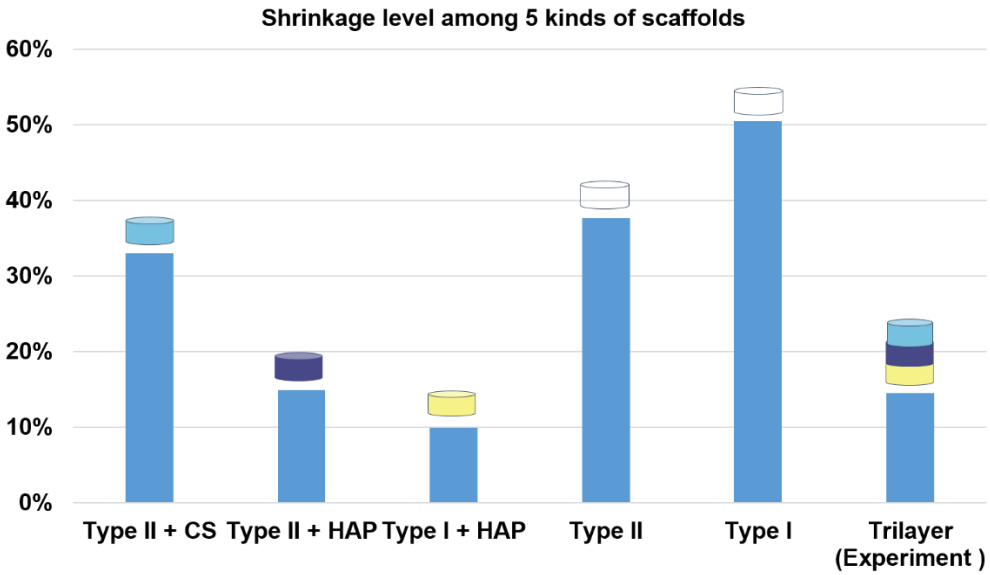

Figure 4.12 Shrinkage levels of six scaffolds

Figure 4.12 demonstrates the shrinkage level of six types of scaffolds. The scaffold composed of pure collagen had the highest shrinkage level, followed by a shrinkage level of 38% in the scaffold composed of type II collagen and 50% in the scaffold composed of type I collagen. The cartilage, middle and bone layers had a shrinkage level of 33%, 15% and 10%, respectively. The integrated tri-layered scaffold had a uniform and relatively low shrinkage level (14%).

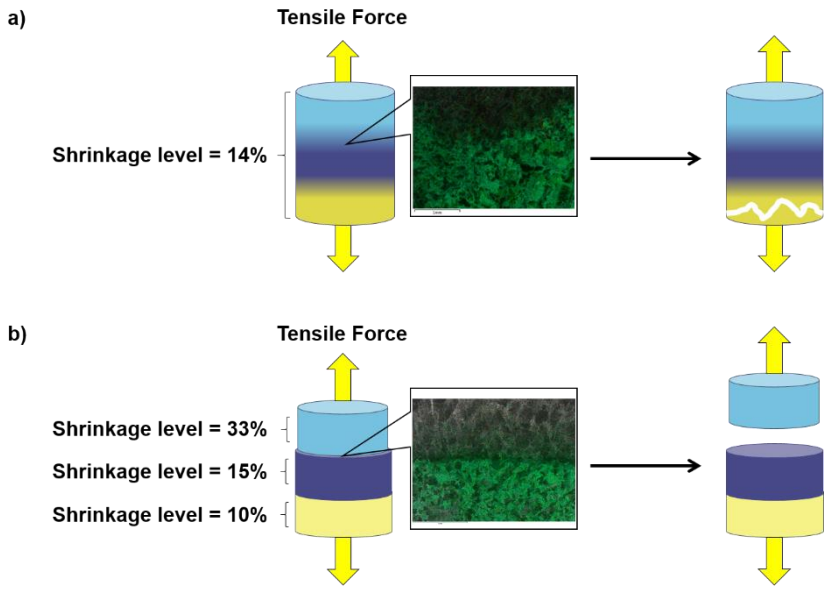

Figure 4.13. a) Scaffolds in the experimental group had a uniform shrinkage level; no gap but gradient change was observed between the layers, and hence, delamination was not observed in the interface. b) Scaffolds in the control group had three different shrinkage levels with differences between the top (shrinkage level = 33%) and middle (shrinkage level = 15%) layers, which resulted in a gap formation between the layers and hence contributed to delamination in the transition region.

As shown in **Figure 4.13b**, scaffolds in the control group had different shrinkage levels because the layers were not integrated. Shrinkage resulted in the separation of layers, and a gap was observed in the transition region that contributed to delamination. However, scaffolds in the experimental group (**Figure 4.13a**) had a uniform shrinkage level, indicating that there was a gradient change in the transition region between layers, and hence, delamination did not occur in the transition region.

4.4 Discussion

Press-fitting leeway range for clinical application

The maximum elastic stress and strain help surgeons to determine how much leeway they can have when handling the scaffolds (dry). The tri-layered scaffold designed in this study has a cylindrical shape (diameter = 2 cm and height = 2 cm). As seen in **Figure 4.14**, to maintain the shape and microstructure of the scaffold, it should be carefully handled during implantation. The maximum force of a surgeon's hand should not exceed 0.68 N, with a maximum strain of 8.62% (or displacement of approximately 0.2 cm).

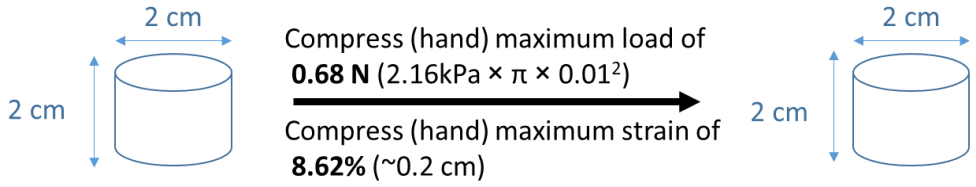

Figure 4.14. Leeway range of the press-fitting compression force (0.68 N) and strain (8.62% or 0.2 cm) for a cylindrical-shaped implant with a diameter and height of 2 cm.

Mechanical properties of the mono-layered scaffolds

Type I versus type II collagen scaffold

Type II collagen scaffold had a larger Young's modulus than that of the type I collagen scaffold according to both compression (12.22 kPa versus 4.11 kPa, respectively) and tension (132.86 kPa versus 103.5 kPa, respectively) tests. In addition, crosslinked scaffolds had a higher modulus than that of the non-crosslinked scaffolds (non-crosslinked type I collagen scaffold, 2.3 kPa; non-crosslinked type II collagen scaffold, 2 kPa).[102]

The results revealed that the modulus of the tensile strength was a magnitude higher than that of the compression strength of pure type I and type II collagen scaffolds. Pure type I and type II collagen scaffolds had a compression modulus of approximately 10–20 kPa. However, their tensile modulus was approximately 10 times higher (130 kPa and 100 kPa for type I and type II collagen scaffolds, respectively). This phenomenon has been reported and investigated in previous studies as well. Harley explained that this phenomenon can be attributed to the presence of a dense 'air side' layer, which significantly increases the tensile strength of the scaffolds.[123] Franklin and Liang also demonstrated that the tensile modulus was orders of magnitude higher than the corresponding compressive modulus.[124, 125]

Interaction between HAP and the scaffold matrix

The addition of HAP dramatically impacted the compression and tensile modulus. After the addition of 70% and 80% HAP to pure type I and type II collagen, the modulus of

the two collagen composites was almost 10 times larger than that of the pure collagen scaffolds. We proposed two hypotheses to explain this dramatic increase in modulus.

First, HA particles are trapped in the collagen fibres through mechanical interlocking and act as crosslinks between adjacent fibrils. Second, as shown in **Figure 4.15a**, as the compression force increases, HAP particles come closer, repel each other and hence limit the final length to which the fibres can be strained before rupture. An increase in modulus of the composite has also been reported in other studies.[104, 124]

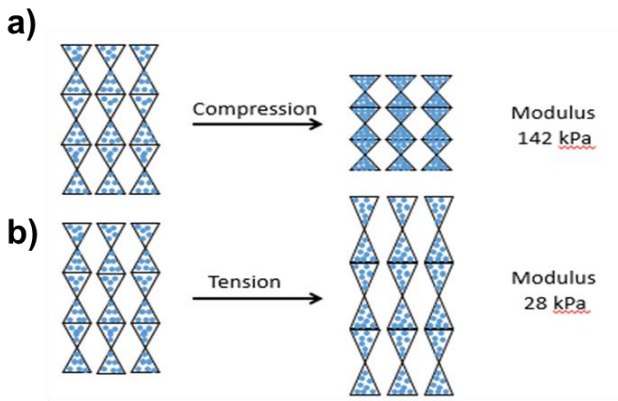

Figure 4.15 Interaction between HAP (blue dot) and the scaffold matrix. a) In the compression test, HAP particles repel each other when compressed together; b) In the tensile test, HAP particles are localised on the elongated scaffold matrix.

However, HAP did not contribute to the increase in the tensile strength of the scaffold matrix. No difference was observed in the tensile modulus between pure collagen type II scaffold and scaffold composed of type II collagen and HAP (70%). Furthermore, HAP (80%) significantly reduced the tensile modulus of type I collagen from 100 kPa to 28 kPa because HAP particles acted as localised stress concentrators on the fibrous collagen matrix. When tension force was applied, the collagen fibres began to align

and extend in the direction of the force. HAP particles were separated with the tensile force to prevent them from influencing the tensile strength (**Figure 4.15b**). However, the stress between collagen and HAP particles increased, which decreased the modulus of the overall composite and strain at failure (from 6.08% to 2.12%). Similar results were reported by Wahl et al from our research group in a previous study.[126]

Dry and wet conditions

In this study, the mechanical modulus (both compression and tensile) under dry conditions was always 5–100 times larger than that under hydrated (wet) conditions. Some previous studies have also reported this phenomenon.[123, 127, 128] This change in modulus is attributed to the plasticising effect of water on collagen, which results in a weaker bulk mechanical response in the wet state. Water is a plasticiser that can reduce both inter- and intra-macromolecular interactions among the collagen matrix owing to strong hydrogen bonding in water, which gives it the ability to interact with other polar molecules. For example, water molecules can form hydrogen bonds with many polar groups (hydrophilic and charged) within the collagen matrix, such as OH, -COOH, COO^- and $-NH_2$ [129]

Plasticisation effects of water

Under wet conditions, as illustrated in **Figure 4.10d** and **4.11d**, the non-integrated scaffolds delaminated immediately after they were immersed in PBS owing to the plasticisation effects of water. Water filled the gap between the cartilage and middle layers and softened the interface; therefore, the weak interaction between the layers could not maintain the bonding between them. However, the integrated scaffolds did

not delaminate immediately after they were immersed but delaminated under an ultimate tension force of 108.2 Pa. In the case of real surgery, the scaffolds may be immediately filled with blood that contains bone marrow stem cells after the scaffolds are implanted into the defect.

Shrinkage, Poisson's ratio and delamination

The gradient interface of the native tissue contributes greatly to mechanical properties. When the osteochondral joint moves, the cartilage layers lining the articular surfaces of the bones slide and roll.[130] When two layers of cartilage come in contact with each other, the phenomenon is equivalent to a rigid sphere indenting a flat articular cartilage layer[131] as described in **Figure 4.15**.

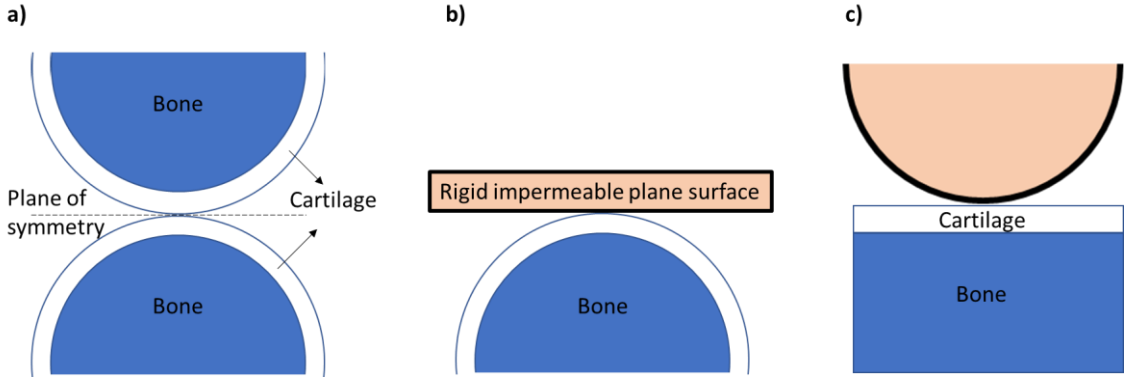

Figure 4.16 (a) Two cartilage layers in contact with each other at a plane of symmetry; (b) The contact model is equivalent to a rigid plane contacting the bone–cartilage layer; (c) A rigid sphere indenting a flat cartilage–bone composite. Adapted from [49][131].

Without a gradient interface, or if the cartilage and bone bind with a hard interface (**Figure 4.16a**), the sliding contact in the joint induces a very different shear elongation owing to different Poisson's ratios and leads to decohesion and delamination between the cartilage and bone.[132] The gradient interface (**Figure 4.16b**) suppresses delamination by providing cohesion between layers.

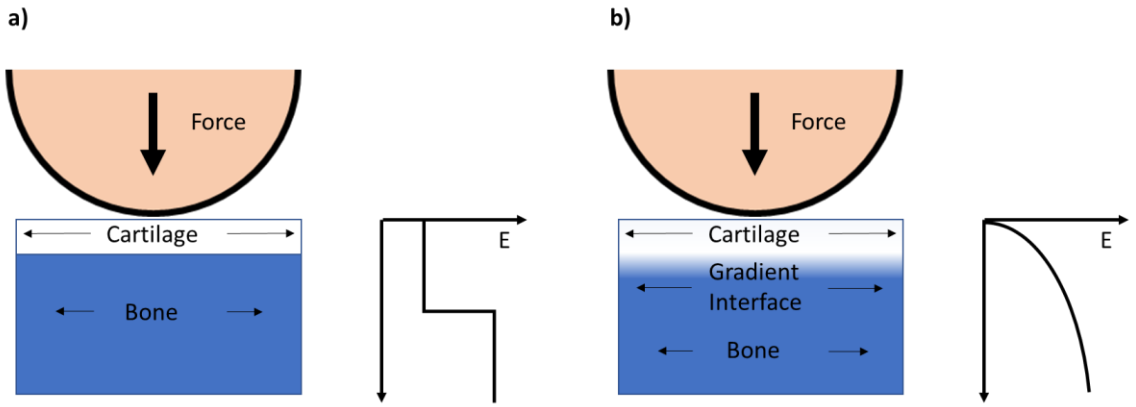

Figure 4.17 Effect of force on osteochondral joint with (a) a hard interface, leading to delamination between layers owing to decohesion caused by different shear elongations in the cartilage and bone and with (b) a gradient interface that provides cohesion between two layers, suppressing delamination. Adapted from [50][132]

Therefore, the cause of delamination was a significant level of differential shrinkage among the various layers of scaffolds. This finding has also been reported in other studies. Sherwood found that the cartilage layer shrunk by 8.3% in diameter, whereas the transition layer only shrunk by 3.8%.[133] This difference in the level of shrinkage caused excessive shear stress and might have contributed to delamination.

Three factors responsible for mechanical properties of the scaffold

The mechanical properties of the designed collagen scaffolds are a function of three factors as follows[127]:

1) Relative density of the sponge

2) A constant related to the pore geometry

3) Elastic modulus of struts (solid materials that scaffolds are made of)

$$\frac{E_{scaffold}}{E_{solid}} = C_1 \emptyset^2 (\frac{\rho}{\rho_{solid}})^2 + C2(1-\emptyset)\frac{\rho}{\rho_{solid}}$$

(Equation 4.1)

In the abovementioned equation, $\frac{\rho}{\rho_{col}}$ is the relative density of the cell, ρ is the density of the scaffold and ρ_{solid} is the density of the solid that the pore matrix consists of.

C1 and C2 include all geometric constants.

$\emptyset$ is the variable fraction of collagen in the pore.

$E_{scaffold}$ is the elastic modulus of the pore matrix.

E_{solid} is the elastic modulus of the pure solid (for example, for cartilage layer, E_{solid} is the elastic modulus of the composite with 50% type II collagen and 50% CS).

As elastic distortion increases, axial load on the pore wall increases. During compression, if this axial load reaches the Euler load (critical load), it buckles and decreases the modulus. Moreover, axial load strain is very small and can be mathematically ignored[164]. This phenomenon was also reported by Gibson as beam–column interaction[163]. Therefore, the modulus is dominated by buckling during compression (**Figure 4.19**).

$$\frac{E_{compression}}{E_{Solid}} = C_1\emptyset^2(\frac{\rho}{\rho_{Solid}})^2 + C2(1-\emptyset)\frac{\rho}{\rho_{col}}$$

(Equation 4.2)

$C2(1-\emptyset)\frac{\rho}{\rho_{col}}$ only applies to a negligible strain. Therefore,

$$\frac{E_{compression}}{E_{Solid}} = C_1\emptyset^2(\frac{\rho}{\rho_{Solid}})^2$$

(Equation 4.3)

Substituting E_{solid} for its equivalent based on the rule of mixtures,

$$\frac{E_{compression}}{E_{col\ II}V_{col\ II} + V_{CS}E_{CS}} = C_1\emptyset^2(\frac{\rho}{\rho_{Solid}})^2$$

(Equation 4.4)

Or

$$E_{compression} = C_1\emptyset^2(\frac{\rho}{\rho_{Solid}})^2(E_{col\ II}V_{col\ II} + V_{CS}E_{CS})$$

(Equation 4.5)

First, the relative density $\frac{\rho}{\rho_{Solid}}$ can be calculated as follows:

$$\frac{\rho}{\rho_{Solid}} = \frac{\frac{m}{v}}{\frac{1}{\frac{X_{solid1}}{\rho_{solid1}} + \frac{X_{solid2}}{\rho_{solid2}}}}$$

(Equation 4.6)

In the abovementioned equation, ρ is the density of the scaffold and can be calculated from the mass and volume of the scaffold.

ρ_{Solid} is the density of the solid. According to the rule of mixtures, ρ_{Solid} can be calculated from the composition of solid materials. X is the mass fraction.

For example, for the cartilage layer in this study that is made of 50% collagen II and 50% CS.

$$\rho_{Cartilage\ layer\ solid} = \frac{1}{\frac{50\%}{\rho_{collagen\ II}} + \frac{50\%}{\rho_{CS}}}$$ (Equation 4.6)

Another factor affecting mechanical modulus is the geometric constant or pore anisotropy. Caliari et al. demonstrated the relationship between elastic modulus and geometry.[165]

$$E_a^* = E_i^* \left(\frac{2R^2}{1 + \left(\frac{1}{R}\right)^3}\right)$$

(Equation 4.7)

In this equation, E_i^* is the elastic modulus of the isotropic foam, and R is the aspect ratio of pores.

Based on the findings of the study by Caliari et al.[165], aligned collagen scaffolds have a significantly higher tensile modulus than that of isotropic controls (800 kPa versus 300 kPa, respectively). Aligned scaffolds were fabricated via directional solidification in their study. However, this method was not used in our study, and the scaffolds that we designed are more similar to an isotropic cell. In our future study, we may consider increasing anisotropy to increase the compressive/tensile modulus, especially for the bone layer of the designed scaffold, which has relatively weak tensile strength.

The third factor is the modulus of the solid strut. According to the rule of mixtures, the modulus for composite scaffolds can be calculated as follows:

$$E_{comp-bone\ layer} = E_{col\ I} V_{col\ I} + V_{HAP} E_{HAP}$$

(Equation 4.8)

In this equation $E_{comp-cartilage\ layer}$, $E_{comp-middle\ layer}$ and $E_{comp-bone\ layer}$ are the compression elastic moduli of the cartilage, middle and bone layers, respectively.

$V_{col\ II}$, $V_{col\ I}$, V_{CS} and V_{HAP} are the volume fractions of these solid materials.

In this study, the composite scaffolds (all three individual layers) contained a higher amount of solid material in the initial suspension than that in pure collagen suspension, which may result in higher density and thicker pore walls and edges that contributed to the higher compression modulus of the scaffold. For example the compression modulus of pure type I collagen scaffold was only 4.1 kPa (**Section 4.3.1**). After HAP was added, according to **Equation 4.8**, the volume fraction of HAP increased, and E_{HAP} was higher than $E_{col\ I}$ (HAP was denser and stiffer) [166]; therefore, the E_{comp} of the bone layer of the composite scaffold increased to 141.6 kPa after HAP was added to the suspension.

4.5 Summary

The tri-layered scaffold designed in this study demonstrated that it could not only provide sufficient leeway for surgeons during surgery but also withstand the load from joint movement and prevent delamination better than the controls under both dry and wet conditions.

In conclusion, the main findings are summarised as follows:

1. The compression modulus of each layer and composite layers (COL II + CS, COL II + HAP and COL I + HAP) was much larger than the modulus of homogenous

collagen scaffolds (both COL I and COL II) owing to the crosslinking effect and interaction between CS/HAP and collagen.

2. The compression modulus of the tri-layered scaffolds (dry condition) was determined, and a maximum press-fitting force of 0.68 N was calculated. This leeway range of 0–0.68 N seems achievable for surgeons.

3. The tensile and delamination tests confirmed that the designed tri-layered scaffolds were mechanically superior to the control scaffolds because the control scaffolds delaminated owing to a lack of interface.

Given that the tri-layered scaffold had strong mechanical properties, we further aimed to assess its biological function to determine whether it can be used to repair ODs.

Chapter 5. In vitro performance evaluation of the scaffolds

5.1 Introduction

We performed in vitro studies to evaluate the clinical effectiveness of the tri-layered scaffold. Cell studies were first conducted to test the biological properties such as biocompatibility and differentiation in the scaffolds in vitro.

Section 5.2 illustrates the experimental procedures, including cell seeding (section 5.2.1), cell viability and cell attachment assays performed to assess the biocompatibility of the designed scaffold (Section 5.2.2). Cell proliferation assay (Section 5.2.3), q-PCR (Section 5.2.4), and histological analysis (Section 5.2.5) were performed to evaluate whether the three individual layers could guide bone marrow stem cells to differentiate into desired individual components, i.e. cartilage, calcified cartilage and bone. The results are demonstrated in Section 5.3 and discussed in Section 5.4. The main findings are summarised in Section 5.5.

5.2 Methods

5.2.1 Isolation and culture of rabbit-derived BMSCs

After anaesthetising rabbits via intravenous injection of 5% pentobarbital sodium (0.5 mL/kg), 15 mL of bone marrow aspirate was extracted from the ilium and placed in a 50-mL heparinised centrifuge tube. The aspirate was resuspended with a regular culture medium and centrifuged at 200 g for 8 min; the supernatant was removed, resulting in purified BMSCs. Thereafter, the cells were resuspended again, transferred to culture dishes and cultured at 37°C and 5% CO_2. After 5 days, the medium was

changed to remove non-adherent cells. BMSCs at passage 2 were used for subsequent experiments.

5.2.2 In vitro cell seeding

Each mono-layered cylindrical scaffold (cartilage, middle and bone layers), 5 mm in diameter and 2 mm in thickness, was placed in a non-treated 24-well plate (Thermo Fisher Scientific), and 400 µL of BMSC suspension (approximately 2 x 10^5 cells) was added onto the surface of each scaffold for cell seeding. Thereafter, the scaffolds were incubated for 4 hours at 37°C and 5% CO_2 to allow cell attachment.

The chondrogenic culture medium contained high-glucose DMEM, 10-ng/mL transforming growth factor beta-1 (TGF-β1, R&D Systems Inc., Minneapolis, USA), 50-ng/mL insulin-like growth factor-I (IGF-I, R&D Systems Inc.), insulin-transferrin-selenium (ITS-X, GIBCO, Life Technologies, Grand Island, NY, USA) and ascorbic acid (Sigma-Aldrich, USA). The osteogenic culture medium contained 39.25-mg/L dexamethasone (Sigma-Aldrich, USA), 17.612-mg/L vitamin C (Sigma-Aldrich, USA) and 30.611-g/L β-sodium glycerophosphate (Sigma-Aldrich, USA). For the experiment, 2 mL of the chondrogenic medium was added to the upper and middle layer of the scaffolds kept in the cell culture dish, and 2 mL of the osteogenic medium was added to the bottom layer. The scaffolds were cultured for 21 days, and the medium was changed every 2 days.

To test the in vitro cell seeding efficiency of individual layers (including the upper, middle and bone layers), BMSCs at passage 2 were seeded onto the surface of each mono-layered scaffold at a density of 1×10^8 cells/mL. After 24 h of incubation, the cell–scaffold constructs were gently rinsed with PBS to remove the dead cells. The

cells were counted, and the result was expressed as N. The cell seeding efficiency of the scaffolds was calculated using the following formula: [134]

$$\frac{Total\ cell\ number - N}{Total\ cell\ number} \times 100\% \qquad \text{(Equation 5.1)}$$

5.2.3 In vitro cell viability

The cell viability of rBMSCs was examined using a Live/Dead® Cell Viability assay kit on days 1, 7 and 21 of culture. The scaffolds were rinsed twice with PBS for 20 min. Subsequently, live and dead cells were stained with calcein-AM and ethidium bromide, respectively. Cells were imaged using an ApoTome 2 microscope (Zeiss, Germany) at a wavelength of 450 nm.

5.2.4 In vitro cell proliferation (DNA quantification)

The rBMSC–scaffold constructs were cultured for 1, 4 and 7 days. Total DNA was extracted from the samples and quantified using a PicoGreen dsDNA assay kit (Invitrogen, USA). The experiment was performed in triplicate.

DNA quantification was performed using the papain solution (Sigma-Aldrich). Briefly, the collected samples were digested with a proteinase K solution (250 μg/mL, 1 mL) at 56 °C for 12 h and centrifuged at 12,000 rpm for 10 min to collect the supernatant. Subsequently, 28.7 μL of the standard solutions and supernatants were added to a 96-well plate, followed by the addition of 71.3 μL of PicoGreen solution and 100 μL of tris−EDTA buffer. The samples were then incubated for 10 min in the dark, and fluorescence was measured on a microplate ELISA reader (BioTek, Winooski, VT, USA) at an emission wavelength of 490 nm and absorbance wavelength of 520 nm. A

standard curve was created based on the measured absorbances of the standard solutions, and DNA was quantified.[135]

5.2.5 In vitro real-time polymerase chain reaction

After 21 days of culture, total RNA was isolated/extracted from the scaffolds using TRIzol™ reagent (Life Technologies). Briefly, TRIzol (3 mL/100 mg of tissue, better more than less) was added to samples and placed in a glass homogeniser for homogenisation and then in an ice bath for 10–15 min. The samples were transferred to 1.5-ml Eppendorf (EP) tubes and centrifuged at 13,000 g at 4 ºC for 10 min. The supernatant was transferred to another EP tube and placed at room temperature for 10–15 min. Subsequently, 0.2 mL of chloroform/1 mL of Trizol was added, and the suspension was shaken for 15 s and incubated at room temperature for 5 min. The suspension was centrifuged at 12,000 g at 4 ºC for 15 min, and the upper aqueous phase was carefully removed and transferred to a new EP tube. Thereafter, 0.5 mL of isopropanol/1 mL of Trizol was added and incubated at room temperature for 10 min. The sample was centrifuged again at 12,000 g at 4 ºC for 10 min, and a white sediment was obtained at the bottom of the EP tube. The supernatant was then discarded, and the precipitate was dissolved in 1 mL of 75% ethanol. The sample was centrifuged at 11,000 g at 4 ºC for 5 min. Ethanol was removed, and the sample was air-dried for 10 min (centrifugal drying can be accelerated, and centrifugal liquid should be removed as much as possible). When the RNA sample turned translucent, it was dissolved in 20 uL of nuclease-free water (can be blown and mixed evenly) and stored at -20 ºC. The content and purity of the extracted total RNA were analysed using a nucleic acid–protein analyser. The absorbance of all samples at 260/280 nm was 1.8–2.0. The extracted RNA was subjected to agarose gel electrophoresis (1% gels), resulting in

clear 28s and 18S rRNA bands. The quality of the isolated RNA was then verified on a NanoDrop spectrophotometer (LabTech). cDNA was synthesised from RNA via reverse transcription using Master Mix reagent (Agilent) and a thermal cycler (Bio-Rad, T100). Gene expression was analysed via q-PCR on a BioRad CFX96 machine. Primers were purchased from Sigma-Aldrich, and their sequences are provided below:

Chondrogenic markers:

1. Type I or II collagen

Forward, 5′-CACGCTCAAGTCCCTCAACA-3′; reverse, 5′-TCTATCCAGTAGTCACCGCTCT-3′;

2. Aggrecan or cartilage-specific proteoglycan core protein

Forward, 5′-GGAGGAGCAGGAGTTTGTCAA-3′; reverse, 5′-TGTCCATCCGACCAGCGAAA-3′;

3. Sox-9 or transcription factor SOX-9

Forward, 5′-GCGGAGGAAGTCGGTGAAGAAT-3′; reverse, 5′-AAGATGGCGTTGGGCGAGAT-3′

Osteogenic makers:

1. Alkaline phosphatase (ALP)

   Forward, 5′-CCGAATTCATGTTGGCCTGTTCAACT-3′; reverse, 5′-ATGTCGACTTAGTTATTTTCATAATACCAAATTCC-3′

2. Osteoblast-specific transcription factor osterix (OSX)

Forward, 5′-AGAGATCTGAGCTGGGTAG-3′; reverse, 5′-AAGAGAGCCTGGCAAGAGG-3’

3. Runt-related transcription factor 2 (Runx2)

Forward, 5′-TCAGGCATGTCCCTCGGTAT-3′; reverse: 5′-

TGGCAGGTAGGTATGGTAGTGG-3′

5.2.6 In vitro histological analysis

After 4 weeks of in vitro culture of cell–scaffold constructs, histological analysis was performed to assess cartilage regeneration. The constructs were fixed with 4% paraformaldehyde for 24 h and embedded in paraffin using standard histological procedures. Briefly, a sharp scalpel was used to carefully and quickly remove a section of suitable size (1.5 × 0.2 cm), which was immediately placed in 10% formalin for internal fixation for 24 h (preferably no more than 48 hours). After dehydration, 70% (2H), 80% (2H), 90% (2H) and 95% alcohol (2H for I and II) and anhydrous alcohol (1H for I and II) were used to remove xylene (1H for I and II) from the tissue slices. The transparent tissue block was embedded in paraffin melted in an incubator (58–60 ℃) (I and II for 2 hours each) to remove xylene. A layer of glycerin was added to the inner wall of the embedder, melted paraffin was poured and the tissue block was soaked in paraffin (with the section facing down). Furthermore, spacing and orientation were arranged, and the embedder was placed in a cold water bath to solidify paraffin. For slicing, the wax block was cut into 5-μm-thick slices, which were flattened on the water surface at 45℃. The slices were transferred to slides coated with an anti-stripping agent and placed in the oven at 60℃ for 2 h. For dewaxing, xylene was removed using alcohol solutions of gradient concentrations (100%, 95%, 80% and 70%) (15 min for Ⅰ and Ⅱ), and the slices were stained after hydration with distilled water. The histological sections (6-μm thick) were stained with haematoxylin and eosin (H&E), safranin O, collagen type II and alizarin red S.

H&E is a combination of two histological stains: haematoxylin stains the cell nuclei blue, and eosin stains the ECM and cytoplasm pink, with other structures taking on different shades, hues and combinations of these colours.[136] The purpose of H&E staining was to evaluate the cell structure and ECM deposition of the regenerated tissue. Briefly, the slices were incubated in a 70℃ incubator for 1–2 h. For dewaxing and hydration, the slices were immersed in xylene I, II and III solutions for 15 min each and hydrated with 100%, 95%, 85% and 75% gradient alcohol solutions. Subsequently, the slices were rinsed with running water for 5 min. Haematoxylin was added to stain the nucleus for 8 min, and the slices were rinsed with tap water for 1 min. After differentiation with 75% hydrochloric acid and ethanol for 1 s, the slices were rinsed with running water for 30 min, followed by dehydration using 95% ethanol for 1 min. Thereafter, the slices were incubated in acidified eosin ethanol for 90 s, followed by dehydration using 75%, 85%, 95% and 100% gradient alcohol solutions. Subsequently, the slices were immersed in xylene. After the slices turned transparent, the slices were sealed with neutral resin and evaluated under a microscope.

Safranin O stains the growth plate cartilage and articular cartilage (proteoglycans, chondrocytes and type II collagen) varying shades of red. The intensity of safranin O staining is proportional to the proteoglycan content in the cartilage tissue.[137] The purpose of safranin O staining was to evaluate the content and distribution of proteoglycans. Fixed, dewaxing, hydration and H&E staining were performed as described in the previous section. After differentiation with 0.5% hydrochloric acid alcohol for several seconds, the slices were rinsed with distilled water for 2 min and flushed with running water for 25 min. The cells were stained with safranin O stain for

3 min, followed by rapid dehydration with 95% and 100% alcohol. The slices were immersed in xylene. After the slices turned transparent, neutral resin was used to seal the slices, followed by microscopic observation.

Alizarin red S is a dye used for staining calcium deposits in tissues; it binds with calcium to form a lake pigment that is orange–red.[138] Tissue samples were fixed in 4% paraformaldehyde, embedded in paraffin and sectioned. The purpose of alizarin red S was to evaluate the content and distribution of calcium.

5.2.7 Statistical analysis

All experiments were repeated at least thrice, and the results were expressed as the mean ± standard error. All data were analysed using the SPSS software 17.0. The differences between the experimental and control groups were considered statistically significant when $P < 0.05$.

5.3 Results

5.3.1 In vitro cell viability

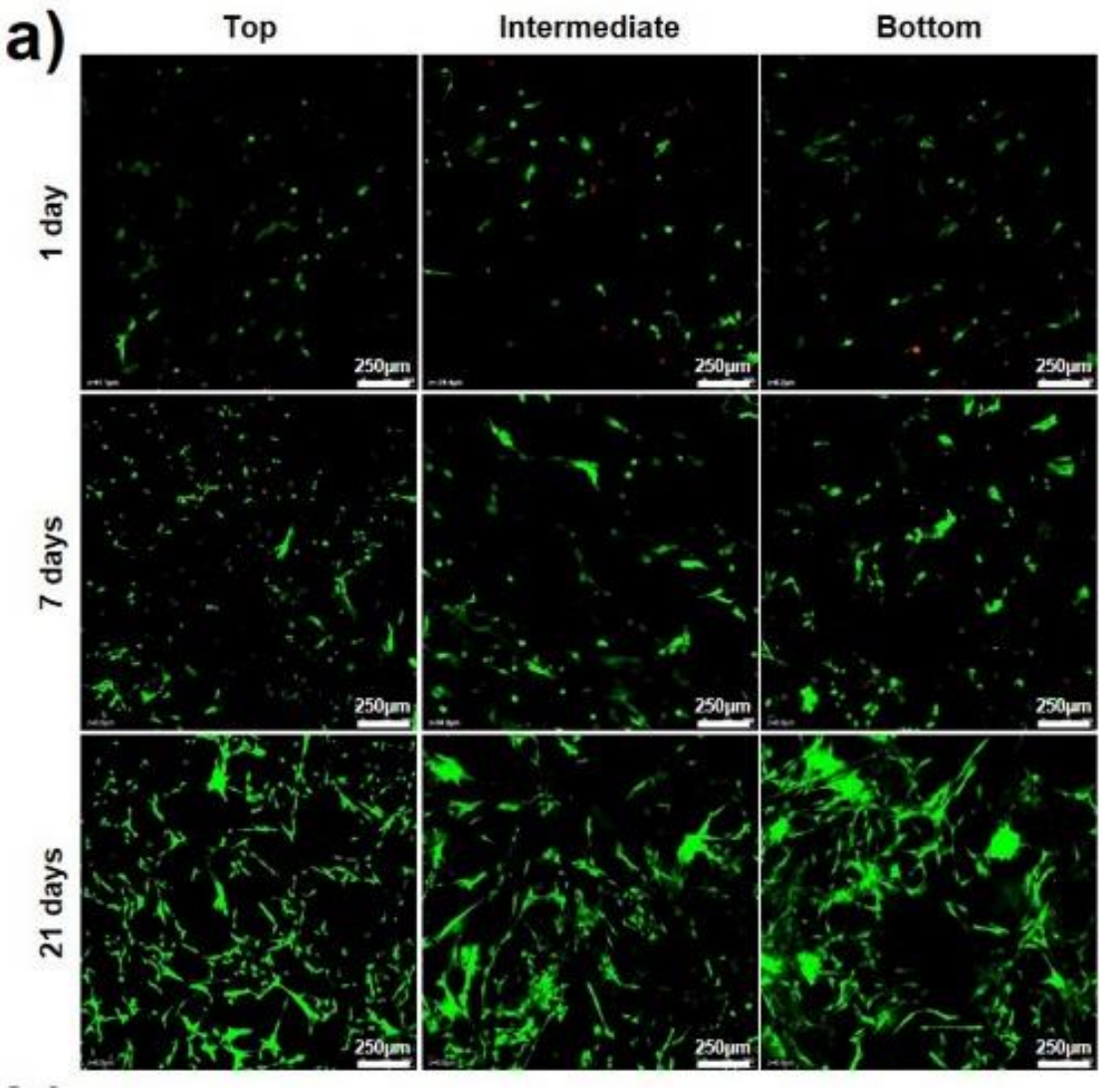

Figure 5.1 Live and dead staining shows that most cells remained viable after 1, 7 and 21 days of cell seeding in the in vitro culture condition (scale bar = 250 μm). The top surface of the scaffolds was used for observation.

Cell viability was examined using a Live/Dead assay kit on days 1, 7 and 21. Viable cells were stained bright green, and dead cells were stained red. **Figure 5.1** demonstrates that most cells were alive on day 1 and remained viable after 7 and 21

days in all three mono-layered scaffolds. Cell proliferation was observed on days 7 and 21 via flow cytometry, and the screen was occupied by the growing number of cells. These results indicated that all three mono-layered scaffolds promoted the adherence, survival and proliferation of rBMSCs.

5.3.2 In vitro cell seeding efficiency

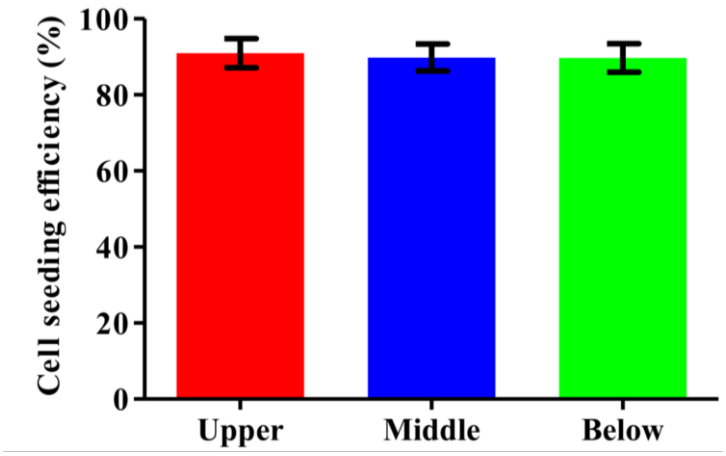

Figure 5.2 Quantitative analysis of cell seeding efficiency. All three individual layers had approximately 90% cell seeding efficiency after 24 h of cell seeding.

Cell seeding efficiency was measured to evaluate cell adherence within the three mono-layered scaffolds. As demonstrated in **Figure 5.2**, approximately 90% cell seeding efficiency was achieved at 24 h in all mono-layered scaffolds, which was likely attributed to the optimal pore size distribution and porosity.

5.3.3 In vitro cell proliferation (DNA quantification)

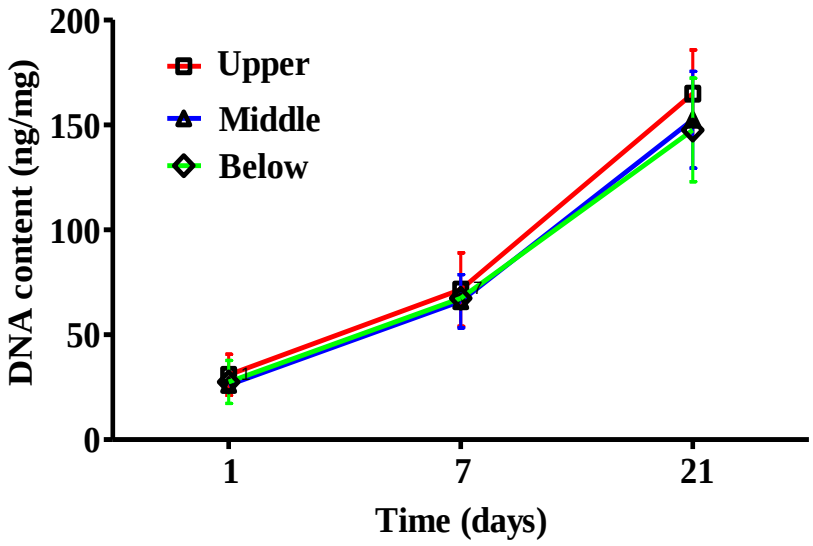

Figure 5.3 Quantitative analysis of cell proliferation. DNA content was increased in all groups.

The cell proliferation assay (**Figure 5.3**) revealed rapid cell growth in each layer of the scaffold. In addition, all mono-layered scaffolds had increased DNA content during in vitro cultivation, indicating that the scaffolds possessed good cytocompatibility. These results were consistent with those of the Live/Dead assay.

5.3.4 In vitro real-time polymerase chain reaction

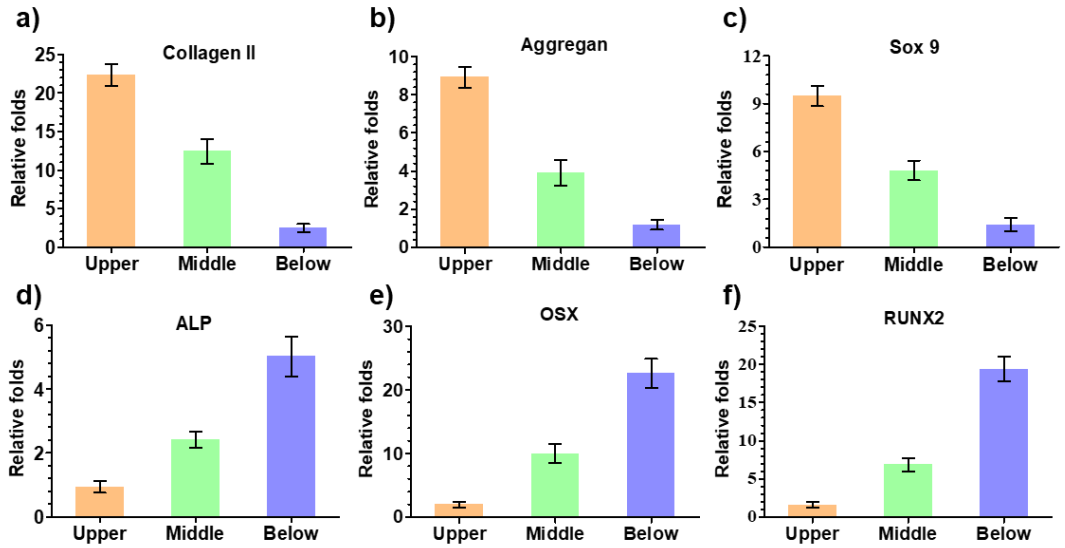

Figure 5.4 Evaluation of the differentiation of rabbit bone marrow stem cells (rBMSCs) cultured on each layer of the tri-layered scaffold 21 days after cell seeding. Relative gene expression (normalised to GAPDH) of the chondrogenic markers: a) collagen type II, b) cartilage-specific proteoglycan protein aggrecan and c) transcription factor SOX-9. Relative gene expression (normalised to GAPDH) of the osteogenic markers: d) alkaline phosphatase (ALP), e) osteoblast-specific transcription factor osterix (OSX) and f) runt-related transcription factor 2 (Runx2). All data are expressed as mean ± standard deviation (n = 4). Relative folds indicate the gene expression of the experimental group normalised to that of the reference gene GAPDH.

The chondrogenic differentiation of rBMSCs seeded on the scaffolds was determined via gene expression of three cartilage-specific markers after 21 days of cell culture.

As shown in **Figure 5.4a, 5.4b and 5.4c**, the expression of all chondrogenic markers was significantly higher in the upper layer than in the middle and bottom layers. The middle layer exhibited a medium expression level of chondrogenic markers, indicating a medium level of chondrogenic differentiation.

As shown in **Figure 5.4d, 5.4e and 5.4f**, the results of osteogenic differentiation were opposite of those of chondrogenic differentiation. A significantly higher expression

level of all three osteogenic markers was observed in the bottom layer than in the other two layers, indicating strong osteogenic differentiation in the bottom layer. The upper layer exhibited a relatively low expression level of all three markers, particularly that of OSX and RUNX2. In addition, the middle layer exhibited a medium expression level of all three markers, indicating moderate osteogenic differentiation. Furthermore, q-PCR results suggested that medium levels of both osteogenesis and chondrogenesis were observed in the middle layer, which was expected to form calcified cartilage.

5.3.5 In vitro histological analysis

Based on the promising results of q-PCR, we further performed histological analysis for each in vitro-cultured mono-layered collagen scaffold.

Histological examination (including H&E, safranin O, COL II and alizarin red S staining) revealed that features of preliminary osteochondral-like tissue were formed after 4 weeks of in vitro culture, with distinctive features observed in each layer.

H&E staining

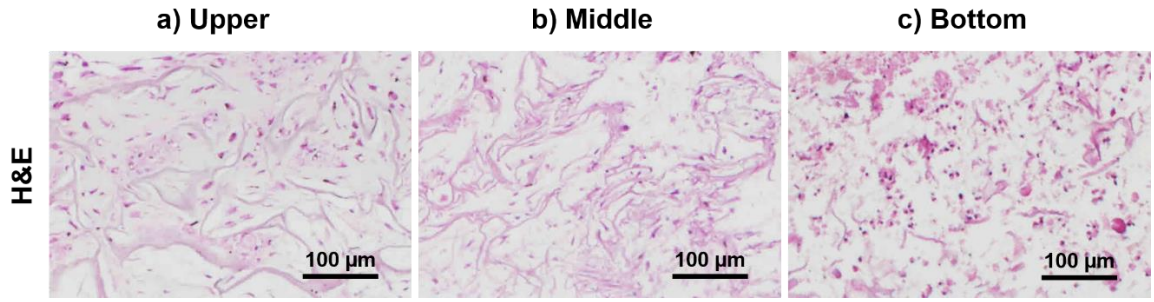

Figure 5.5 H&E staining of three individual layers. a) The upper layer (cartilage layer) demonstrates flattened cartilage-like cells, b) The middle layer (calcified cartilage layer) demonstrates intermediate features of the cartilage and bone layers, c) The bottom layer (bone layer) demonstrates round cells (scale bar = 100 µm).

As shown in **Figure 5.5**, flattened cells were observed in the upper layer (cartilage layer), which is probably a chondrogenic indicator.[25] Moreover, chondrocyte-like cells were observed in the surrounding region of the cell nucleus (**Figure 5.5a**).[139, 140] However, spherical cell morphology was observed in the bottom layer (**Figure 5.5c**), which may indicate osteogenic differentiation [25]. Moreover, cells in the middle layer had intermediate morphological features of the cells in the upper and bottom layers. With a mixture of both flattened and spherical cells (**Figure 5.5b**), the middle layer represented a transition between chondrogenic and osteogenic features.

Safranin O and collagen II staining

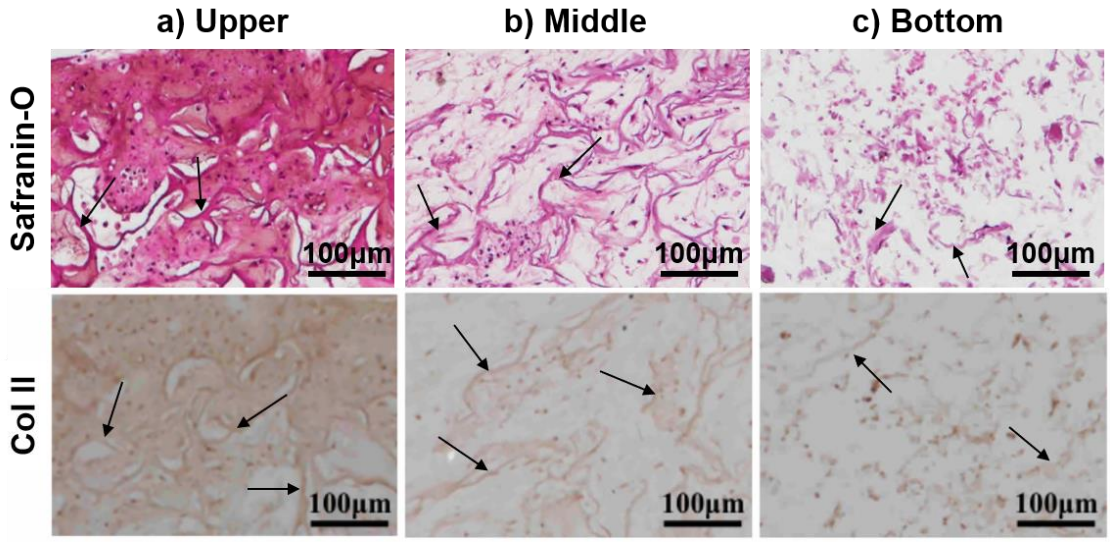

Figure 5.6 In vitro chondrogenic regeneration. (a) The upper layer is positively stained with safranin O and collagen II. (b) The middle layer exhibits some extent of chondrogenic differentiation. (c) The bottom layer exhibits minimal staining. The black arrow indicates the intact scaffold matrix stained with the two dyes.

Strong positive staining of both safranin O and collagen II was observed in the upper layer (**Figure 5.6**), indicating that GAG and collagen type II were regenerated in sufficient amounts, and chondrogenic differentiation was evident in the upper layer. However, the cartilage layer of the designed scaffolds was made of collagen type II,

which may have interfered with staining. Moreover, there was minimal staining in the bottom layer for both safranin O and collagen II, indicating no observable chondrogenic differentiation in the bone layer., The staining intensity of the middle layer was the intermediate of the cartilage and bone layers, with a few safranin O- and collagen type II-positive cells, indicating that chondrogenic differentiation occurred to some extent. The scaffold matrix was intact after 4 weeks of in vitro culture, and the matrix backbone was stained with the two corresponding dyes as well.

Alizarin red S staining

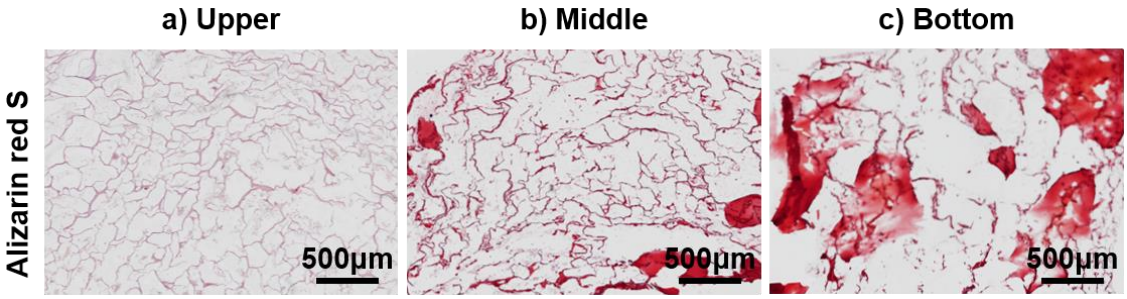

Figure 5.7 In vitro osteogenic regeneration. (a) The upper layer is not stained with alizarin red S. The middle (b) and bottom (c) layers exhibit high staining intensity.

Alizarin (**Figure 5.7**) stains the calcium deposits red.[141] As shown in **Figure 5.7c**, the bottom layer demonstrated strong staining intensity, which may indicate the formation of calcium clusters during osteogenic differentiation. However, because HAP was already present in the scaffold matrix, it is unclear whether the calcium deposit resulted from the matrix or cell differentiation. Moreover, the upper layer was not stained because it underwent chondrogenesis instead of osteogenesis. The middle layer was stained with alizarin red S, indicating the occurrence of osteogenesis, although to a less extent as compared with that in the bottom layer. Moreover, for both

the middle and bottom layers, the remaining scaffold network was also stained red because the scaffold matrix in the middle and bottom layers contained HAP.

5.4 Discussion

Cell differentiation of MSCs in multi-layered scaffolds and regeneration of layer-specific ECM

Developing a scaffold to guide cell differentiation and regenerate cartilage and bone for OD repair simultaneously is challenging. Recently, extensive studies have shown that the composition, mechanical properties and porosity of scaffolds play an important role in osteochondral tissue regeneration [142]. A study showed that fish collagen (FC) is considered an alternative to mammalian collagen (MC) because of its safety, accessibility, low price and similar biological characteristics. Therefore, bi-layered FC-based composite scaffolds with different components and pore sizes have been developed to regulate the differentiation of BMSCs. In a study, FC-containing CS (FC-CS) scaffold was used as the top layer with small pore size (about 128 μm), and HAP-containing FC scaffold (FC-HAP) with large pores (about 326μm) was used as the bottom layer. FC-CS and FC-HAP scaffolds had good cell compatibility, good water absorption, suitable biodegradability and high cell inoculation efficiency. The results of in vitro experiments revealed that FC-CS and FC-HAP promoted chondrogenesis and osteogenesis in BMSCs, respectively, which was confirmed based on gene expression and histological examination. In addition, compared with the control group, the bi-layered scaffold significantly induced simultaneous regeneration of cartilage and subchondral bone 6 and 12 weeks after implantation, which was confirmed based on gross, histological and micro-CT assessments.[143] However, FC was not ideal for

mimicking the composition and microenvironment of the natural cartilage and bone tissue. In addition, the bi-layered scaffold composed of FC-CS and FC-HAP failed to achieve concurrent regeneration of cartilage, calcified cartilage and bone tissues. The tri-layered scaffold fabricated in this study has advantages over the abovementioned FC-based bi-layered scaffold because the tri-layered scaffold is a biomimetic model of the natural composition and microenvironment of cartilage, calcified cartilage and bone tissue, successfully achieving their concurrent regeneration.

Based on the composition of ECM and the structure of collagen fibres in the natural bone and cartilage tissue, a tri-layered scaffold (shallow cartilage, deep cartilage and subchondral bone layers) was designed and manufactured, which contained gelatin-methylacrylamide (GelMA) hydrogels of MSCs. The hydrogel with region-specific growth factor was combined with the three-block polymer of polycaprolactone and polyethylene glycol (PCEC) network with deeply dependent fibrous tissue. Introducing PCEC fibres in weak GelMA hydrogels significantly improved mechanical strength. In vitro biological experiments revealed that the layered fibres and growth factor-loaded hydrogel constructs induced MSCs to differentiate into cells of cartilage and osteogenic lineages, and engineering complexes revealed phenotypic and matrix accumulation profiles similar to those of natural tissues. In addition, simultaneous regeneration of cartilage and subchondral bone was achieved in vivo using the tri-layered integrated scaffolds. More importantly, the addition of a surface layer provided a more lubricating and wear-resistant surface for cartilage regeneration.[15] However, the scaffold was complicated and failed to achieve an integrated structure to mimic the natural composition and microenvironment of cartilage, calcified cartilage and bone tissues. In addition, the applicability of the scaffold was limited by inflammatory

responses. Given that the scaffold fabricated in this study was composed of atelocollagen, it was considered inert to immune responses.

Biological macromolecules with poor mechanical properties cannot meet the strict loading requirements of bioscaffolds. Another study showed that a biodegradable high-molecular-weight supramolecular polymer hydrogel was successfully constructed via photoinitiated polymerisation. The hydrogel was composed of degradable poly (N-acryl-2-glycine) (PACG) and GelMA (PACG-GelMA). The introduction of hydrogen bonds to enhance PACG significantly improved the mechanical strength of gelatin hydrogels, with high tensile strength (up to 1.1 MPa), excellent compressive strength (up to 12.4 MPa), large Yang's modulus (up to 320 kPa) and high compression modulus (up to 837 kPa). In addition, GelMA crosslinking stabilised the temporary PACG network and exhibited biodegradability by adjusting the ACG/GelMA ratio. In addition, a biohybrid gradient scaffold consisting of PACG-GelMA hydrogel–Mn^{2+} in the top layer and PACG-GelMA hydrogel bioactive glass was prepared using 3D printing technology to repair bone and cartilage defects. In vitro biological experiments revealed that the biocrossbred gradient hydrogel scaffolds not only supported cell attachment and proliferation but also enhanced cartilage-related and osteogenic differentiation in human BMSCs. After 12 weeks of in vivo implantation, biocrossbred gradient hydrogel scaffolds significantly promoted the simultaneous regeneration of cartilage and subchondral bone in a rat model.[144] However, the study overlooked the regeneration of intermediate calcified cartilage and failed to mimic the natural composition and microenvironment of cartilage, calcified cartilage, and bone tissues. Therefore, the scaffold fabricated in this study has advantages over scaffolds developed in previous studies.

In this study, the tri-layered scaffolds implanted in the defect site not only provided adequate mechanical support (biodegradable) but also helped to guide the differentiation of MSCs into specific cell types and hence specific tissue types. Therefore, the biomimetic microenvironment of the tri-layered scaffolds helped osteochondral joint regeneration.[58, 145] Stem cell research plays a central role in the further development of medicine, which is mainly dependent on the advances in regenerative medicine (RM), specifically in the disciplines of tissue engineering (TE) and cellular therapeutics. All RM strategies depend on the harnessing, stimulation or guidance of endogenous developmental or repair processes in which cells play an important role. One of the most clinically challenging disorders is cartilage degeneration, which also affects subchondral bone, leading to OD. Although primary cells have been used in clinical settings, stem cells have recently emerged as promising tools for RM-related research because of their availability, in vitro proliferation ability, pluripotency and immunosuppressive features. MSCs are the main focus for osteochondral regeneration.[146]

A study developed BMSC spheroids to support the regeneration of articular cartilage. After 6 months of implantation, the regenerated articular cartilage was 3 times larger than that in untreated animals, and regeneration of the osteochondral tissue occurred during the formation of hyaline-like cartilage. The results demonstrated a positive impact of this advanced combined therapy with stem cells and implantation, which met the requirement of promising osteochondral regeneration in critical-size articular defects in a large animal model.[147]

The response of rBMSCs is affected by the stiffness and composition of the culture environment. The tri-layered scaffolds designed in this study provided an ideal microenvironment for cell growth and independently promoted the chondrogenic, osteogenic and ‘mix-genic’ differentiation of the cartilage, bone and calcified cartilage layers, respectively, thus resulting in the regenerating of osteochondral joint with accurate composition. Moreover, in the in vivo experiments, the control group resulted in minimal fibrocartilage formation and disorganised bone regeneration.

Impact of stiffness on cell differentiation

Substrate stiffness plays a vital role in guiding the differentiation of MSCs, that is, stiffer scaffolds promote osteogenesis, and less stiff scaffolds promote chondrogenesis.[148] Cellular response to the mechanical properties of the scaffold matrix involves a feedback loop, where cells apply force on the matrix and produce strain in the substrate. This strain can then be received by the surrounding cells, which respond by adapting and changing their overall state and cytoskeleton. [149] Engler et al. showed (**Figure 5.8**) that human MSCs differentiated to neuron cells on soft substrates, to myogenic cells on substrates with moderate stiffness and to osteogenic cells on rigid substrates.[150] In addition, it is challenging to develop a bi-phasic scaffold with biomimetic compositional, structural and functional properties to achieve concomitant repair of superficial cartilage and subchondral bone in ODs. Another study developed a biomimetic bi-phasic scaffold for OD repair via an iterative layered lyophilisation technique that controlled the composition, substrate stiffness and pore size in each phase of the scaffold. The bi-phasic scaffold consisted of a superficial decellularised cartilage matrix (DCM) and the underlying decalcified bone matrix (DBM) with distinct but seamlessly integrated phases that mimicked the composition and structure of

osteochondral tissue, in which the DCM phase had relatively low stiffness and small pores (approximately 134 μm), and the DBM phase had relatively high stiffness and larger pores (approximately 336 μm). In vitro experiments revealed that the bi-phasic scaffold was biocompatible for adhesion and proliferation of BMSCs, and the superficial DCM phase promoted chondrogenic differentiation of BMSCs, as indicated by the up-regulation of cartilage-specific gene expression (ACAN, collagen II and SOX9) and GAG secretion. However, the DBM phase induced osteogenic differentiation of BMSCs, as indicated by the up-regulation of bone-specific gene expression (collagen I, OCN and RUNX2) and ALP deposition. Furthermore, compared with the control group, the bi-phasic scaffold significantly enhanced concomitant repair of superficial cartilage and underlying subchondral bone in a rabbit OD model as evidenced by the ICRS macroscopic and O'Driscoll histological assessments.[11]

BMSCs perceive matrix elasticity and translate this information into morphological changes and lineage norms. At the molecular level, the matrix sensor is first required to pull the matrix, and the cell mechanical sensor is subsequently required to generate a signal depending on the force that must be produced to deform the matrix. In the cytoskeletal movement of cells, one or all non-muscle myosin II subtypes are candidates because they are related to the stretching cortical actin structure. These actin structures are, in turn, connected to a focal adhesion complex, which provides a transmission pathway from the interior of the cell to the elastic matrix, and many well-known signalling molecules are associated with the focal adhesion complex, which are well positioned as mechanical sensors. Using BMSCs, we demonstrated that one or all NMM IIA–C may drive matrix elastic sensing following specification.[151]

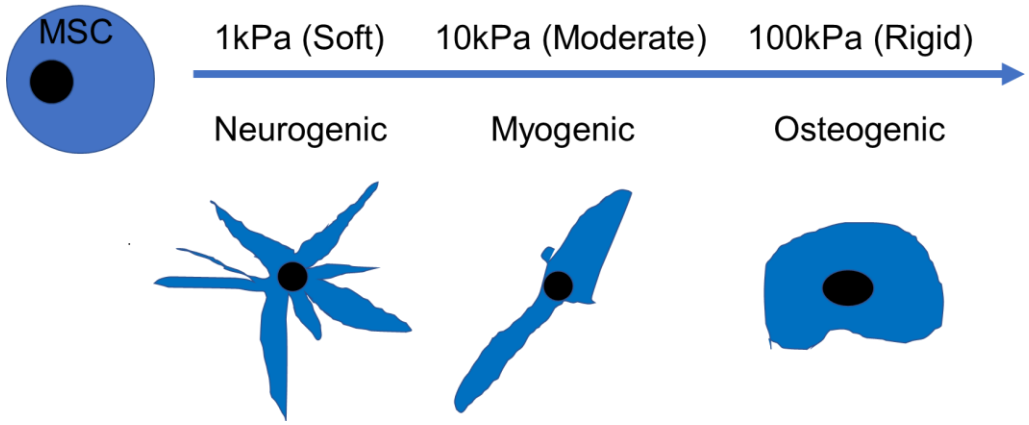

Figure 5.8. Effects of matrix elasticity on mesenchymal stem cell (MSC) fate, adapted from a study by Engler.[150] MSCs are initially small and round, but their shape changes after differentiation when growing on substrates such as soft tissue (brain, 0.1–1 kPa), moderately soft tissue (muscle, approximately 10 Kpa) or hard tissue (collagenous bone, apprximately100 kPa).

The simple one-step liquid-phase co-synthesis fabrication approach used in this study allowed controlling the stiffness in each region of the tri-layered scaffold. The bottom layer (bone layer) had an average dry elastic compressive modulus of 142 kPa (>100 kPa) and favoured osteogenic differentiation. The upper layer (cartilage layer), with an average elastic compressive modulus of 30 kPa, favoured chondrogenic differentiation. The middle layer, with an average elastic compressive modulus of 78 kPa (intermediate of myogenic and osteogenic differentiation), underwent both chondrogenesis and osteogenesis. The novel approach resulted in the development of a scaffold with three distinguished layers with seamless integration. However, our results revealed that the three individual layers significantly softened and exhibited similar wet compressive modulus in the culture medium (approximately 2 kPa); therefore, the influence of different compressive moduli on the individual layers of the scaffold was negligible. Therefore, the differentiation of BMSCs into the cells of cartilage, calcified cartilage and bone lineages is mainly ascribed to the specific microenvironment created by the individual layers of the tri-layered scaffold.

5.5 Summary

The three layers of the tri-layered scaffold exhibited clinical-friendly characteristics as follows:

1) The layers showed excellent biocompatibility to support cell attachment, growth and proliferation.
2) The middle layer exhibited apparent bioactivity to separate the upper and bottom layers.
3) Differentiation of BMSCs into the cells of cartilage, calcified cartilage and bone lineages is mainly ascribed to the specific microenvironment created by each layer of the tri-layered scaffold.

Given the excellent in vitro potential of the tri-layered scaffold, an animal model was used to further determine the actual repair quality of the scaffold.

Chapter 6. In vivo studies

6.1 Introduction

To further evaluate the clinical effectiveness of the tri-layered scaffold, a rabbit model of OD was used. The tri-layered scaffolds were implanted into the knee of the rabbits, and the results were compared with the control group after 2 and 4 months.

The procedure for implanting the scaffold into the rabbit knee is illustrated in Section 6.2.1. Several in vivo studies were performed to evaluate the quality of osteochondral repair in rabbits, including ICRS scores (Section 6.2.2). Micro-CT 3D reconstruction (Section 6.2.3) was used to assess the material aspect quality of the regenerated joints both qualitatively and quantitatively, and follow-up histological examination (Section 6.2.4) was conducted to evaluate osteochondral regeneration biologically. The control group had an empty defect site (without scaffold implantation). The results are illustrated in Section 6.3 and discussed in Section 6.4.

6.2 Methods

6.2.1 In vivo implantation

In vivo assessment of the scaffolds was performed on the rabbit trochlear groove. The study was approved by The Animal Care and Use Committee of Shanghai Jiao Tong University of Medicine, China (No. SH9H-2019-A655-SB). New Zealand white rabbits were purchased from Shanghai Jiagan Experimental Animal Raising Farm (Shanghai, China). A total of 16 skeletally mature (3 months old) New Zealand white rabbits weighing 2.6 kg (range, 2.5–2.7 kg) were used in the study.

To test the in vivo efficiency of the tri-layered scaffold, the following five steps were performed (**Figure 6.2**):

1) The knee skin of the rabbits was peeled off to expose their trochlear groove.
2) ODs were generated in the centre of the trochlear groove of the left knee using an electric drill. A cylindrical hole of 4 mm in diameter and 4 mm in height was created with as illustrated in **Figure 6.1**. These dimensions were determined based on previous studies on rabbit models, which usually reported a diameter and depth of 3–5 mm.

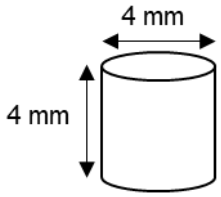

Figure 6.1 Cylindrical defect (4 × 4 mm) created in the trochlear groove in the left knee via an electric drill.

3) Bleeding was induced automatically owing to the perforation of subchondral bone.
4) The tri-layer scaffolds were sterilised with ethylene oxide and implanted into the trochlear groove in the left knee to fill the defect site.
5) Eventually, the skin was sutured to close the lesion. The rabbits were allowed to recover for 12 weeks for in vivo osteochondral regeneration.

The defect site was left empty in the control group (the scaffold was not implanted).

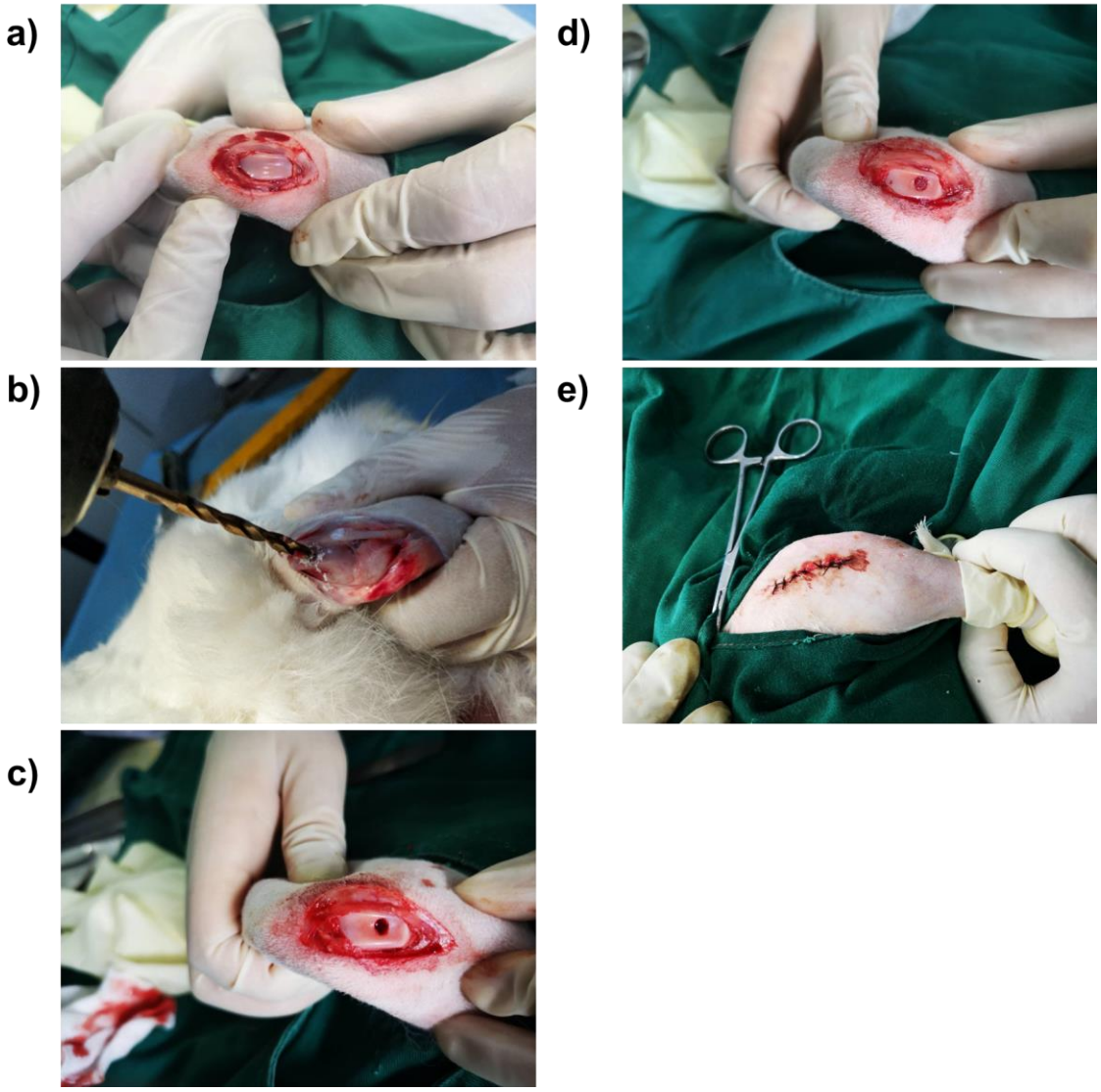

Figure 6.2 Operation procedure. a) The knee skin was peeled off, b) A hole (defect) was created in the centre of the trochlear groove in the left knee, c) Bleeding was automatically induced owing to the perforation of subchondral bone, 4) Tri-layered scaffolds were implanted into the defect site, 5) The knee skin was sutured to close the lesion.

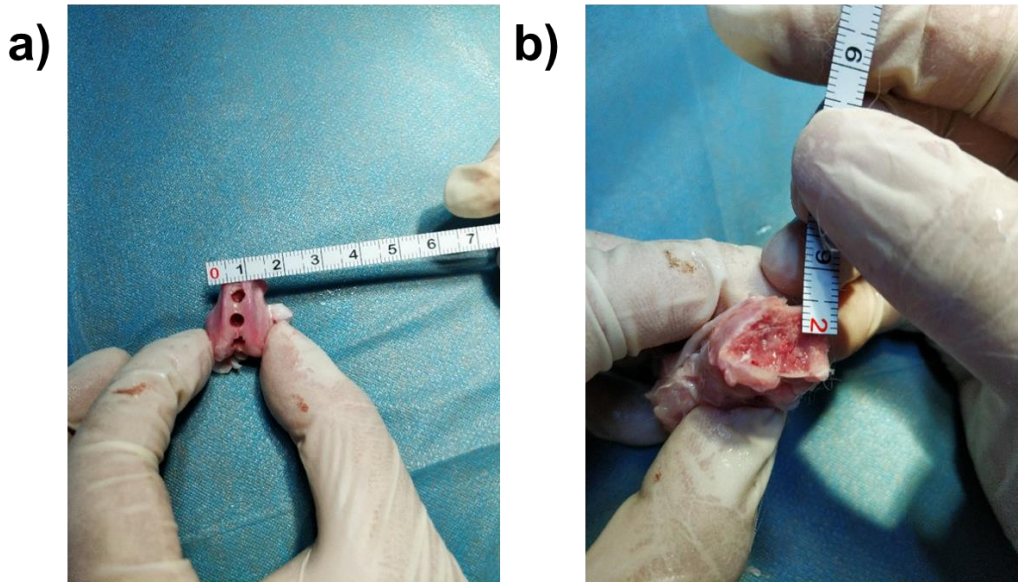

Figure 6.3 Osteochondral defect had a cylindrical shape with a diameter (a) and height (b) of 4 mm.

6.2.2 In vivo evaluation of the regenerated osteochondral joint: Macroscopic observation and ICRS scoring of cartilage repair

The rabbits were sacrificed after 2 and 4 months of implantation, and their knee joints were removed. The samples were assessed by the naked eye, and their diameter was measured.

The repair quality was elevated based on the established cartilage repair assessment criteria recommended by ICRS (**Table 6.1**).

Table 6.1 Criteria for the assessment of cartilage repair established by International Cartilage Regeneration and Joint Preservation Society (ICRS).

	Criteria	Points
Degree of defect repair	*In level with the surrounding cartilage	4
	*75% repair of defect depth	3

	*50% repair of defect depth	2
	*25% repair of defect depth	1
	*0% repair of defect depth	0
Integration to the border zone	*Complete integration with the surrounding cartilage	4
	*Demarcating border < 1 mm	3
	*3/4 of the graft integrated, 1/4 with a noticeable border > 1 mm in width	2
	*1/2 of graft integrated with the surrounding cartilage,1/2 with a noticeable border > 1 mm in width	1
	*From no contact to 1/4 of graft integrated with the surrounding cartilage	0
Macroscopic appearance	*Intact smooth surface	4
	*Fibrillated surface	3
	*Small, scattered fissures or cracks	2
	*Several, small or few but large fissures	1
	*Total degeneration of the grafted area	0
Overall repair assessment	Grade I: normal	12
	Grade II: nearly normal	8–11
	Grade III: abnormal	4–7
	Grade IV: severe	1–3

6.2.3 In vivo evaluation of the regenerated osteochondral joint: Micro-computed tomography

The rabbit joints were further analysed using micro-CT, both qualitatively (3D reconstruction and cross-section evaluation) and quantitatively (evaluation of bone

volume fraction, porosity and mineral density). Zeiss Xradia 510 at the David Cockayne Centre for Electron Microscopy was used for micro-CT characterisation. ImageJ and Avizo (version 9.7.0) were used for subsequent image reconstruction and data processing.

3D reconstruction

For each micro-CT experiment, 2048 TIFF images were obtained. These images were then saved as a single RAW file, which was imported in AVIZO to process a 3D imaging model. The 3D image was exported as a TIFF image.

Cross-sectional imaging

A 3D imaging model was segmented in half using the Avizo crop function to obtain the cross-sectional imaging model. The cross-sectional image was exported as a TIFF image.

Bone volume/total volume Fraction

Bone volume/total volume (BV/TV) fraction indicates the fraction of a given volume of interest (VOI, i.e. TV) that is occupied by the mineralised bone (BV). Both BV and TV were obtained using the AVIZO internal space calculation function. BV/TV is usually expressed as % and can be calculated using the following formula:

$$\frac{Bone\ Volume}{Total\ Volume} \times 100\%$$

(Equation 6.1)

Pore size distribution

Pore size distribution was evaluated via the AVIZO internal pore size identification and calculation function. Briefly, the 3D pore was first identified and labelled with colour, and diameter distribution was calculated and plotted as count versus size (um).

6.2.4 In vivo histological analysis

After 2 and 4 months of implantation, histological analysis was performed to assess cartilage regeneration. The cell–scaffold construct was fixed in 4% paraformaldehyde for 24 h, embedded in paraffin and processed using standard histological procedures. Briefly, the bone tissue was fixed with 10% formalin for 24 h, then saw the bone slice with a thickness of about 0.5 cm and fixed with 10% formalin for 2 days. The tissue was incubated with a decalcifying agent, and the solution was replaced every day until the tissue softened. The tissue slices were rinsed with running water for 24 h and neutralised with 2% sodium sulfite aqueous solution for at least 3 h and washed with water for at least 1 h (acid removal). Subsequently, routine dehydration, wax dipping, slicing and clearing were performed. The histological sections (8-µm thick) were stained with H&E, safranin O/Fast Green, toluidine blue, collagen type II and collagen type I.

Safranin O/Fast Green

Safranin O stains cartilage red in proportion to its proteoglycan content, and Fast Green stains bone green. Coupled with a haematoxylin nuclei counterstain, safranin O/Fast Green is the standard stain for assessing OA.[152]

Toluidine blue

Toluidine blue is a well-established stain for the histological assessment of chondrogenic differentiated tissues. Toluidine blue helps to visualise proteoglycans in the tissue owing to its high affinity for the sulfate groups in proteoglycans. The degree of positive staining corresponds to the proteoglycan content.[153]

Collagen II

Cartilage-specific matrix can be identified based on the expression of collagen type II via immunohistochemical analysis.

Expression of type II collagen was detected using mouse anti-human monoclonal type II collagen (1:100 in PBS, Santa Cruz, CA, USA), followed by the addition of horseradish peroxidase (HRP)-conjugated anti-mouse antibody (1:200 in PBS, Santa Cruz, CA, USA) and colour development with diaminobenzidine tetrahydrochloride (DAB, Santa Cruz, CA, USA).

Collagen I

Bone-specific matrix can be identified based on the expression of collagen type I via immunohistochemical analysis.

Expression of type I collagen was detected using mouse anti-human monoclonal type I collagen (1:100 in PBS, Santa Cruz, CA, USA), followed by the addition of HRP-conjugated anti-mouse antibody (1:200 in PBS, Santa Cruz, CA, USA) and colour development with diaminobenzidine tetrahydrochloride (DAB, Santa Cruz, CA, USA).

6.2.5 Statistical analysis

Analysis of variance (ANOVA) was performed using SPSS for each test. Post-hoc Bonferroni correction was used for multiple comparisons. Significance was accepted at an alpha of 0.05. If sphericity was violated, the Greenhouse–Geisser correction values for ANOVA were considered (n = 4).

6.3 Results

6.3.1 Macroscopic observation of the regenerated osteochondral tissue

Based on the gross assessment of the regenerated osteochondral joints, no inflammatory reaction and synovial hyperplasia were detected in all rabbits. The original scaffold was no longer visible in the experimental group 2 months after implantation. A big empty hole was seen in the control group, with few newly formed tissues (**Figure 6.4b**). The experimental group with the tri-layered scaffold exhibited a certain degree of cartilage repair, although an empty hole was observed in the centre (approximately 1.4 mm, **Figure 6.4a**).

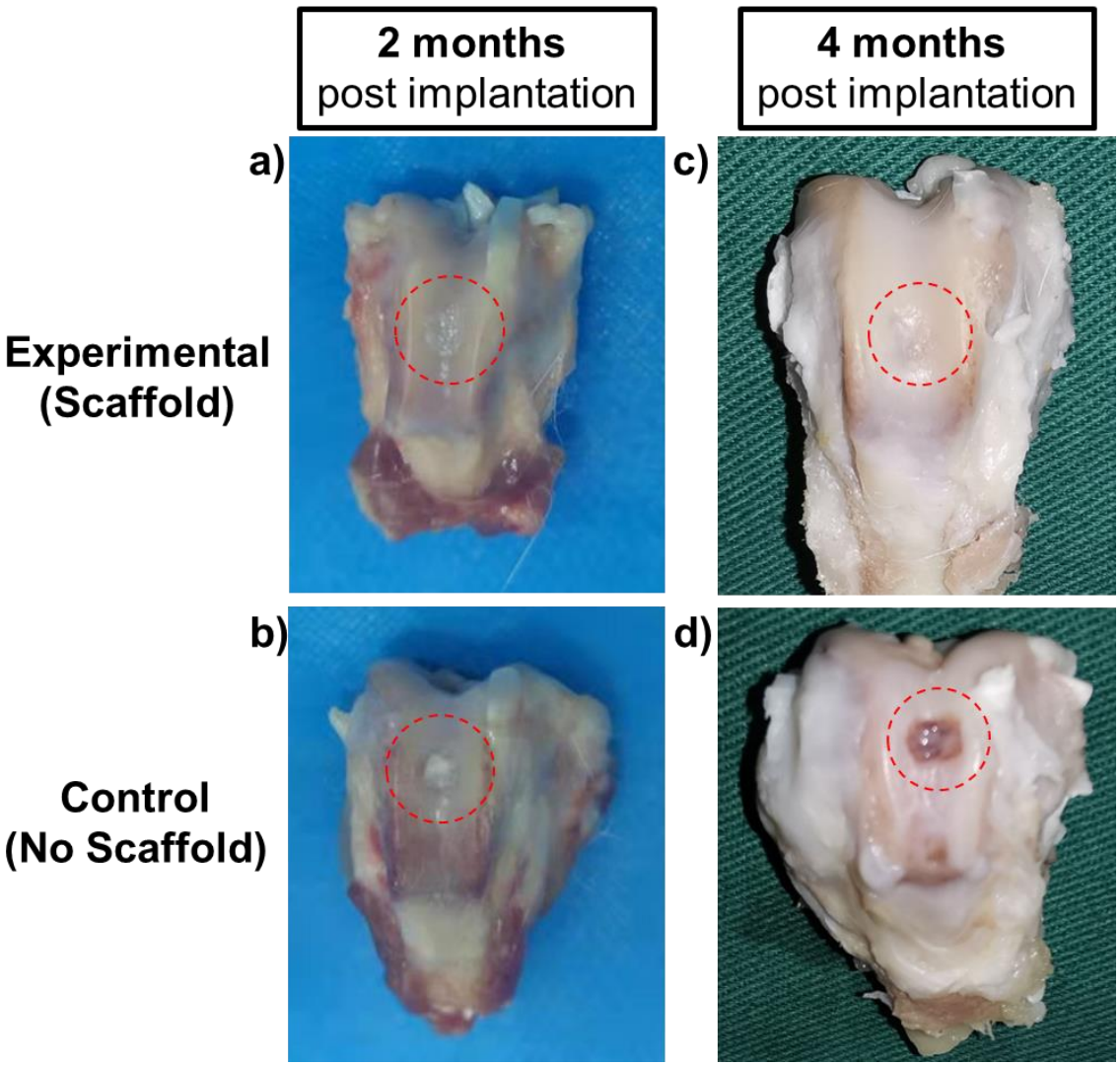

Figure 6.4 The repaired rabbit joint. Joints of the (a) experimental group and (b) control group after 2 months of implantation. Joints of the (c) experimental group and (d) control group after 4 months of implantation.

After 4 months of implantation, hyaline-like cartilage was observed in the experimental group, with no observable hole. In addition, the newly regenerated cartilage and bone integrated well with the surrounding healthy tissue, with the boundary of the original defect merely being visible (**Figure 6.4c**). However, a few newly grown fibrocartilage-like tissues were seen in the control group around the defect, although a large empty hole was observed in the centre (**Figure 6.4d**).

Semi-quantitative scoring results are demonstrated in **Figure 6.5** (with a detailed grading process illustrated in **Table 6.2**). The results were correlated with those of the gross qualitative assessment mentioned above. After 2 months of implantation, the scores of both experimental and control groups were below a good cartilage bar (the scores did not reach level II, which is considered nearly normal based on the ICRS standard). However, the scores of the experimental group were better than those of the control group after 2 months (level III versus level IV, respectively). After 4 months of implantation, the score of the experimental group was 9.2 (level II, nearly normal), and that of the control group was 6.0 (level III, abnormal).

Table 6.2 ICRS scoring for the regenerated osteochondral joints in the experimental and control groups after 2 and 4 months of implantation (n = 4).

	Criteria	Points	Exp (2 months)	Con (2 months)	Exp (4 months)	Con (4 months)
Degree of defect repair	*In level with the surrounding cartilage	4	2.5± 0.3	**0.7**± 0.1	**3.6**± 0.5	**2.4**± 0.7
	*75% repair of defect depth	3				
	*50% repair of defect depth	2				
	*25% repair of defect depth	1				
	*0% repair of defect depth	0				
Integration to the	*Complete integration with the surrounding cartilage	4	**1.4**± 0.4	**0.6**± 0.1	**2.3**± 0.7	**1.5**± 0.2
	*Demarcating border < 1 mm	3				

border zone	*3/4 of graft integrated, 1/4 with a notable border > 1 mm in width	2				
	*1/2 of graft integrated with the surrounding cartilage,1/2 with a notable border > 1 mm in width	1				
	*From no contact to 1/4 of graft integrated with the surrounding cartilage	0				
Macroscopic appearance	*Intact smooth surface	4	**2.5**± 0.3	**1.3**± 0.4	**3.3**± 0.4	**2.1**± 0.2
	*Fibrillated surface	3				
	*Small, scattered fissures or cracks	2				
	*Several, small or few but large fissures	1				
	*Total degeneration of the grafted area	0				
Overall repair assessment	**Grade I: normal**	**12**				
	Grade II: nearly normal	**8–11**			**9.2**± 0.6	
	Grade III: abnormal	**4–7**	**6.4**± 0.3			**6.0**± 0.3
	Grade IV: severe	**1–3**		**2.6**± 0.2		

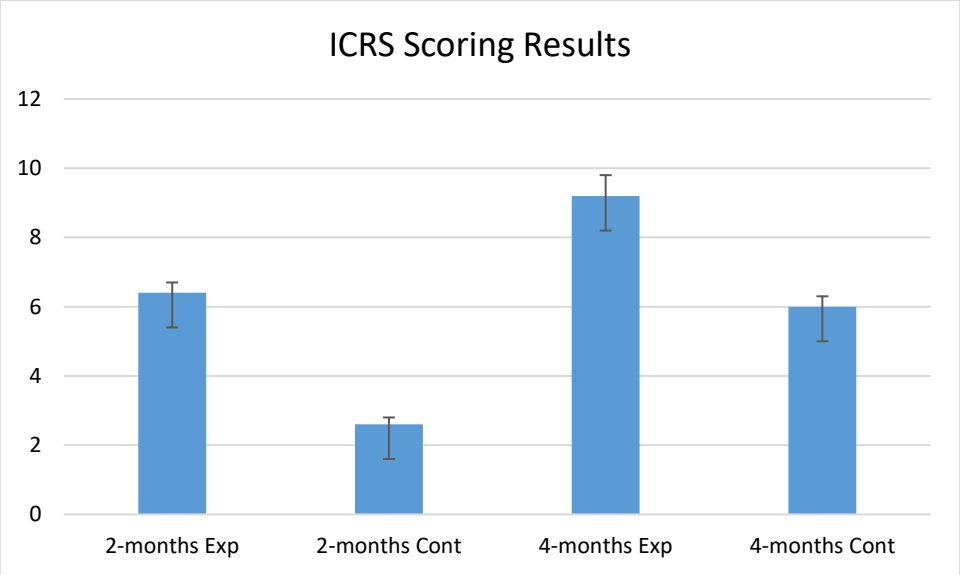

Figure 6.5 ICRS scores for the experimental and control groups after 2 and 4 months of implantation (n = 4).

6.3.2 Micro-computed tomography

3D reconstruction: Qualitative analysis

After 2 months of implantation, glossy white cartilage tissue appeared inside the defect region (**Figure 6.6a**). Micro-CT imaging from the top view (**Figure 6.6c**) demonstrated that the defect was covered by the neotissue. However, an empty hole was seen in the middle of the defect region. The 2D cross-sectional image (**Figure 6.6e**) demonstrated that the neocartilage was formed in the cartilage region, although one-third of the length was yet to be covered by the new tissue. The bone region was quite empty, although some hidden networks were observed.

To identify the detailed structure of the bone, a 3D cross-sectional image was produced using Avizo (**Figure 6.7**). In the 3D cross-sectional image, the neotissue

formation was observed in the bone region, although these networks were not as dense as the normal/healthy bone networks.

Furthermore, a big hole in the defect region was found in the control group (**Figure 6.6b**), although a few white-coloured newly grown tissues was observed on the boundary. The micro-CT top-view image (**Figure 6.6d**) demonstrated that the defect was significantly visible after 2 months. The 2D cross-sectional image (**Figure 6.6f**) revealed a few neotissues in the boundary area in the control group; however, the cartilage was hardly repaired. A more comprehensive 3D cross-sectional image (**Figure 6.7b**) was produced using Avizo, which supported the finding revealed by the 2D cross-sectional image.

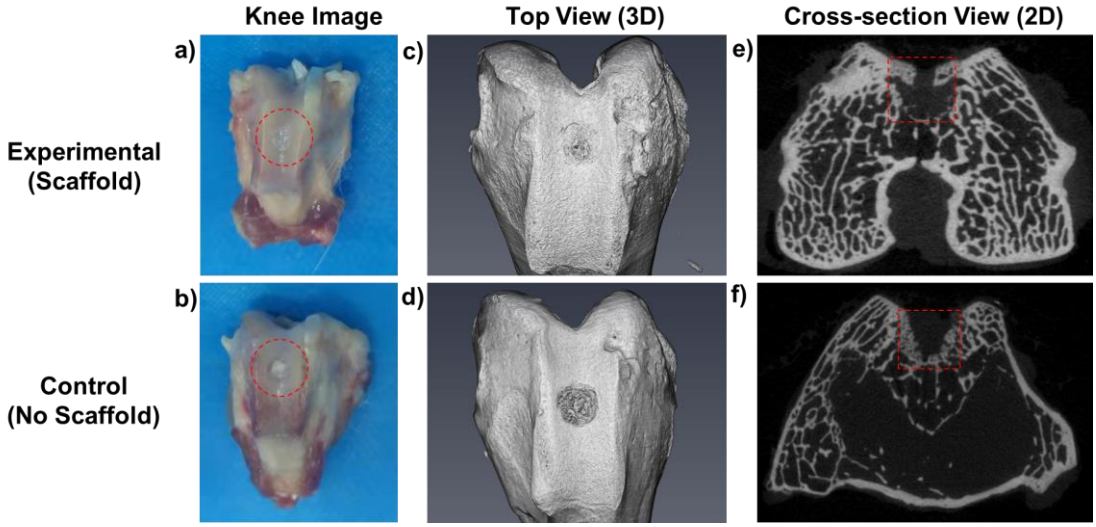

Figure 6.6 Regenerated knee osteochondral joint (2 months after implantation). Micro-CT 3D reconstruction and 2D cross-sectional evaluation of the experimental and control groups.

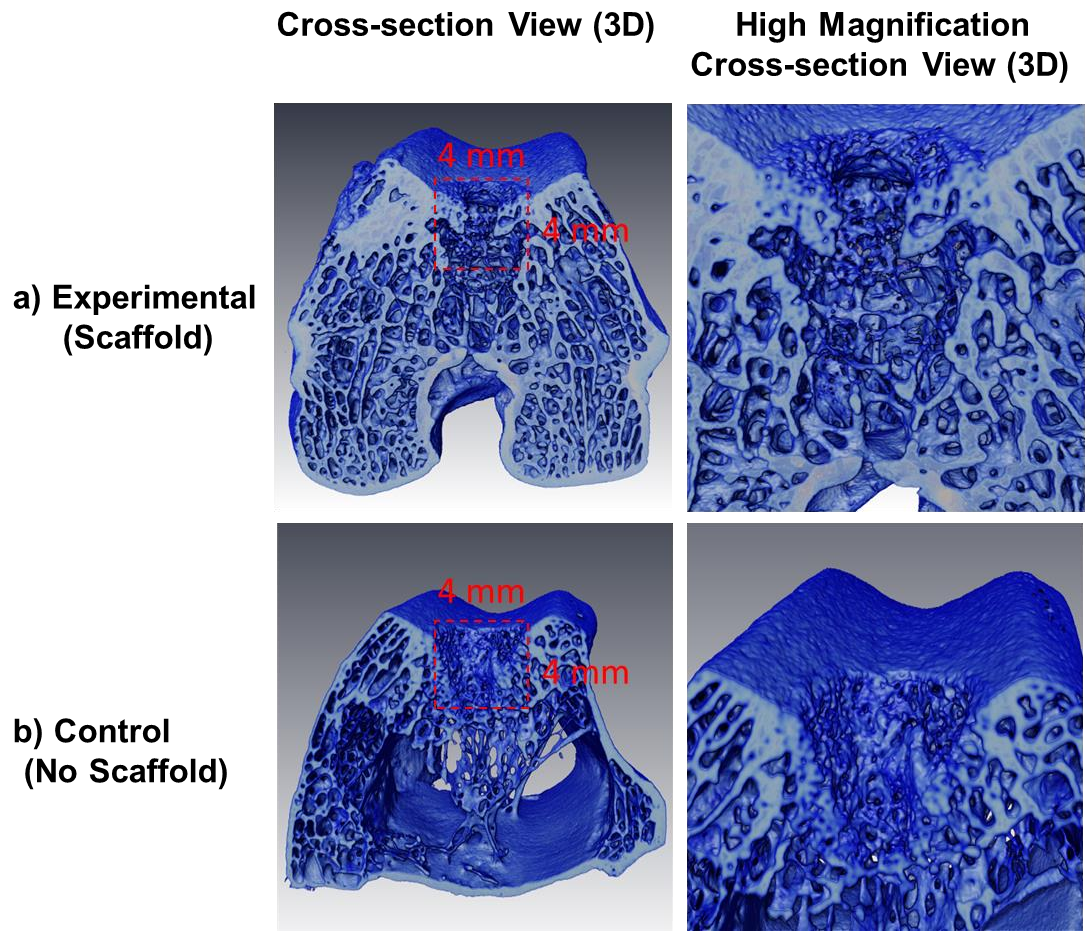

Figure 6.7 Micro-CT 3D cross-sectional evaluation and enlargement (high magnification) of the regenerated osteochondral joint (2 months after implantation) in the experimental (a) and control (b) groups.

After 4 months of implantation, cartilage-like tissue appeared in the defect region (**Figure 6.8a**). The micro-CT top-view image (**Figure 6.8b**) revealed that the newly generated tissue completely covered the defect hole, although a tiny pinhole was observed. The 2D cross-sectional image (**Figure 6.8c**) confirmed that neotissue was formed in both cartilage and bone (**Figure 6.8a**).

To reveal a more detailed structure inside the joint, a 3D cross-sectional image was produced using Avizo (**Figure 6.9a**). In this image, the regenerated tissue was characterised three-dimensionally, and no observable difference in structure was found when compared with the surrounding healthy tissue.

Furthermore, a big hole was found in the control group (**Figure 6.8b**), with no significant improvement compared with that observed after 2 months. The micro-CT top-view image (**Figure 6.8d**) demonstrated that the defect was significant even after 4 months. The 2D cross-sectional image of the control group (**Figure 6.8f**) revealed a few newly generated tissues on the boundary; however, the cartilage was hardly repaired. A more comprehensive 3D cross-sectional image (**Figure 6.9b**) was produced using Avizo, which supported the findings revealed by the 2D cross-sectional image.

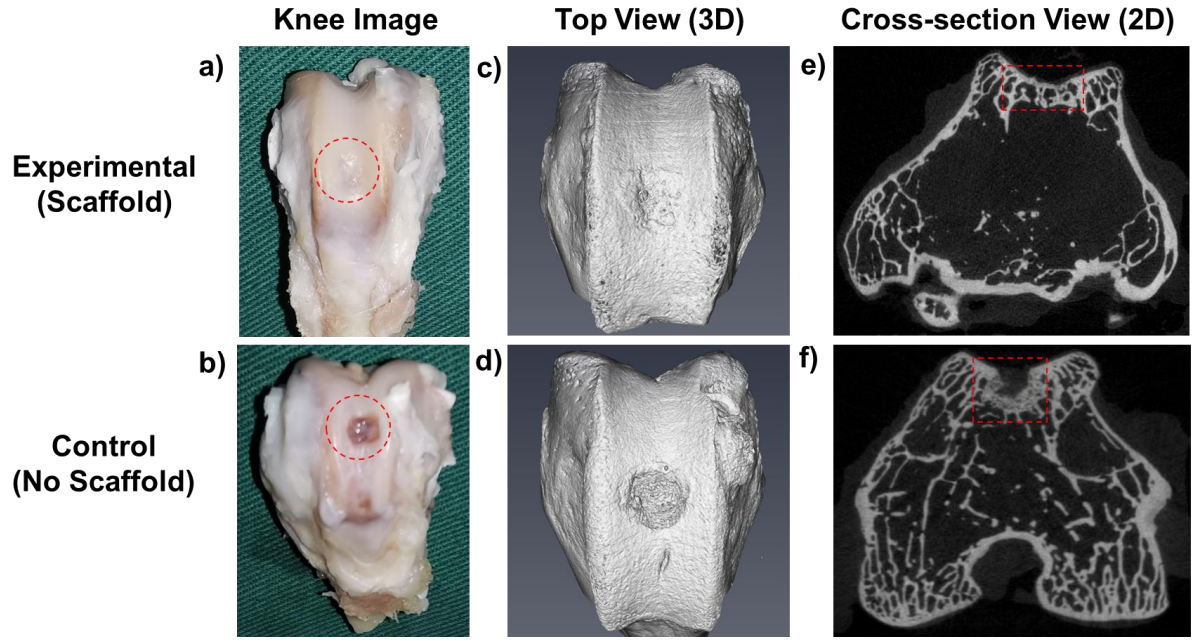

Figure 6.8 Regenerated knee osteochondral joints (4 months after implantation). Micro-CT 3D reconstruction and 2D cross-sectional evaluation of the experimental and control groups.

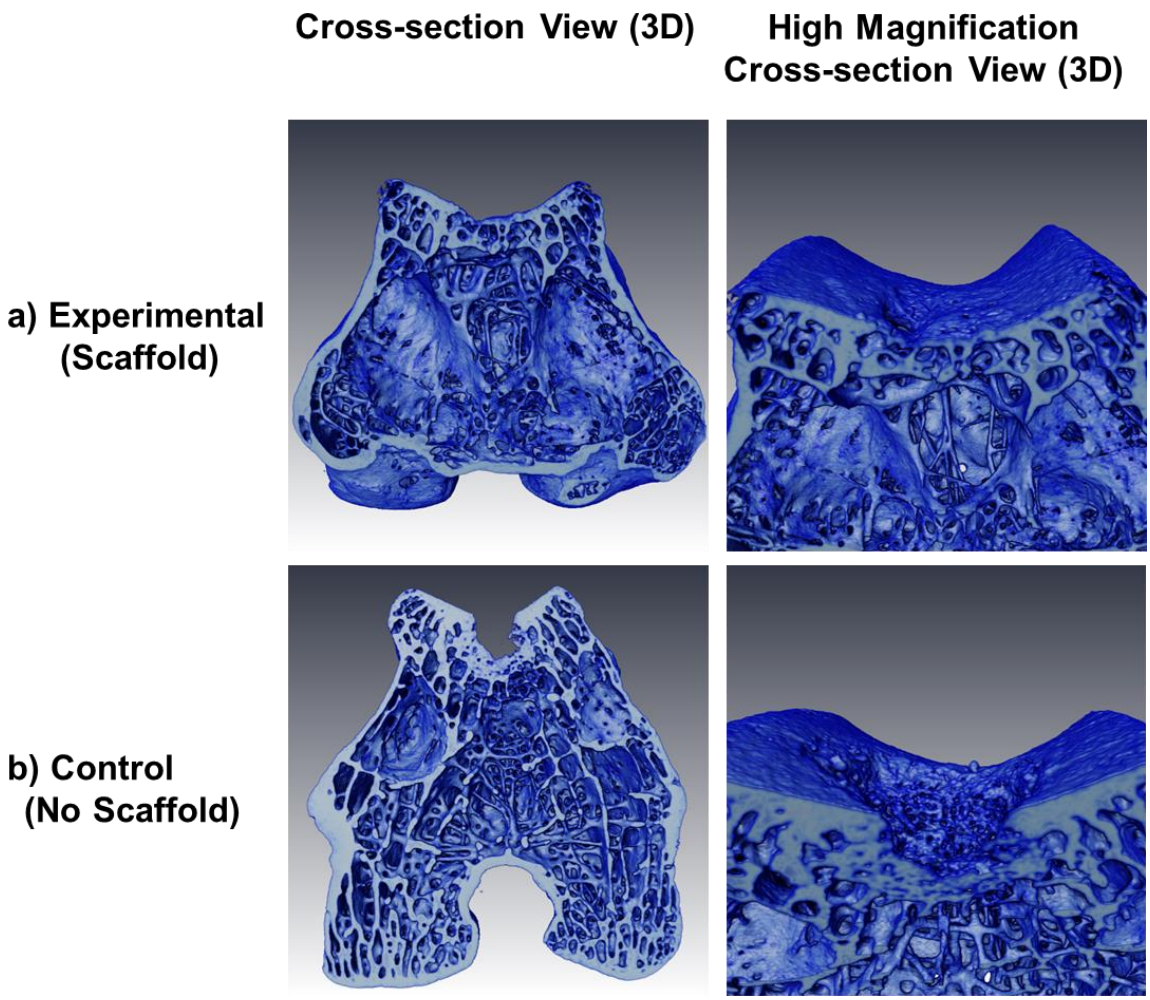

Figure 6.9 Micro-CT 3D cross-sectional images of the regenerated osteochondral joints and their enlargement (high magnification) (4 months after implantation) in the experimental (a) and control (b) groups.

3D reconstruction: Quantitative analysis

Evaluation of bone volume/total volume after 2 months of implantation

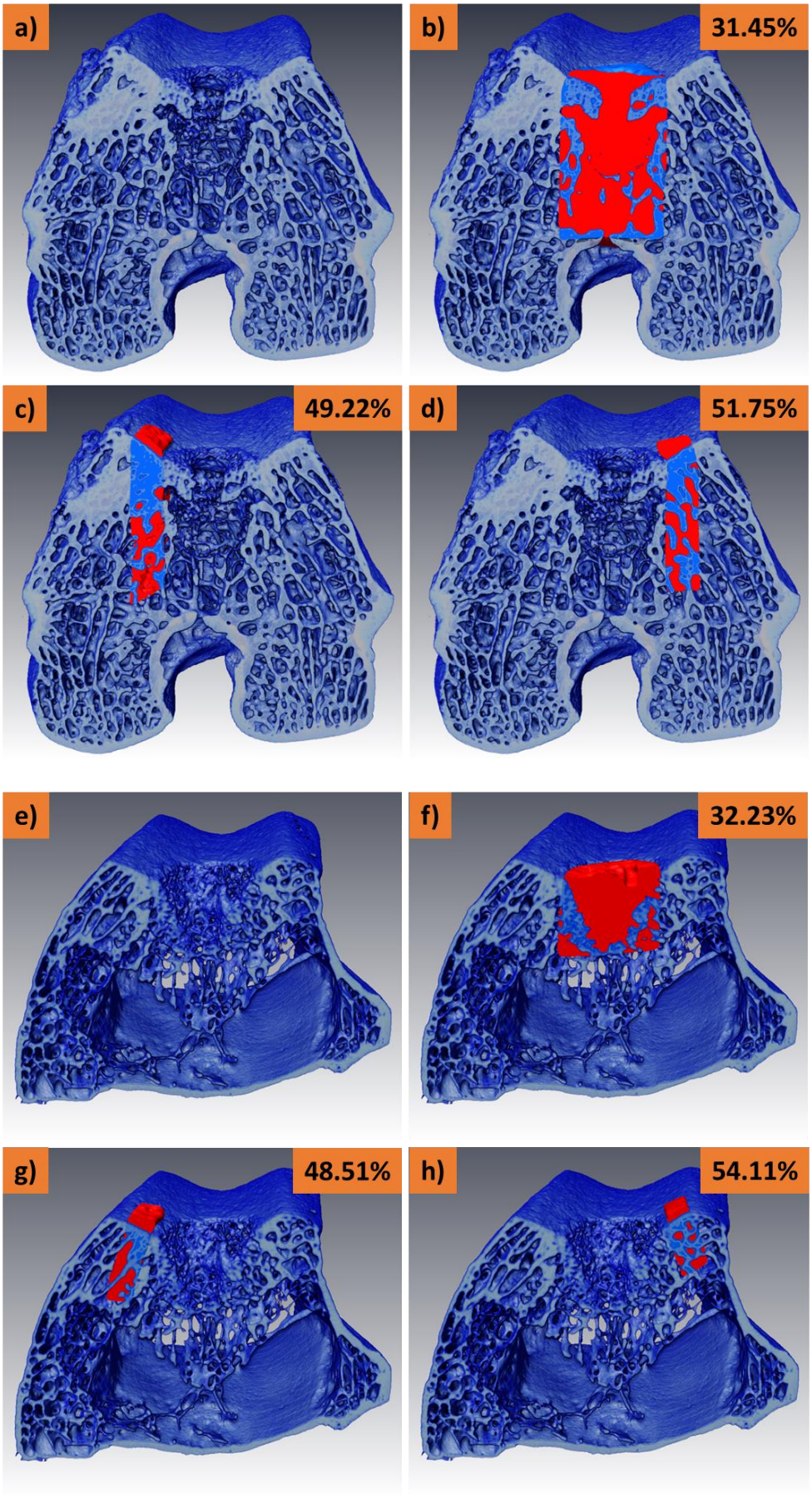
a)
b)
31.45%
c)
49.22%
d)
51.75%
e)
f)
32.23%
g)
48.51%
h)
54.11%

Figure 6.10 BV/TV after 2 months of implantation. a) The cross-section image of the experimental group from **Figure 6.7a**, b) BV/TV calculation of the defect area using Avizo in the experimental group, c) and d) BV/TV calculation of the healthy joint area using Avizo in the experimental group, e) The cross-section image of the control group from **Figure 6.7b**, f) BV/TV calculation of the defect area using Avizo in the control group, g) and h) BV/TV calculation of the healthy joint area using Avizo in the control group.

After 2 months of implantation, although some improvement was observed in the experimental group compared with the control group, as evidenced via qualitative micro-CT assessment, the BV/TV value was similar in both groups, i.e. 31.45% in the experimental group (**Figure 6.10b**) and 32.23% in the control group (**Figure 6.10f**). The BV/TV value of the two groups was significantly smaller than that of the healthy joint (approximately 50%, as shown in **Figure 6.10c**, **6.10d**, **6.10g** an**d 6.10h**). This finding indicated that a longer regeneration time might be required.

Evaluation of bone volume/total volume after 4 months of implantation

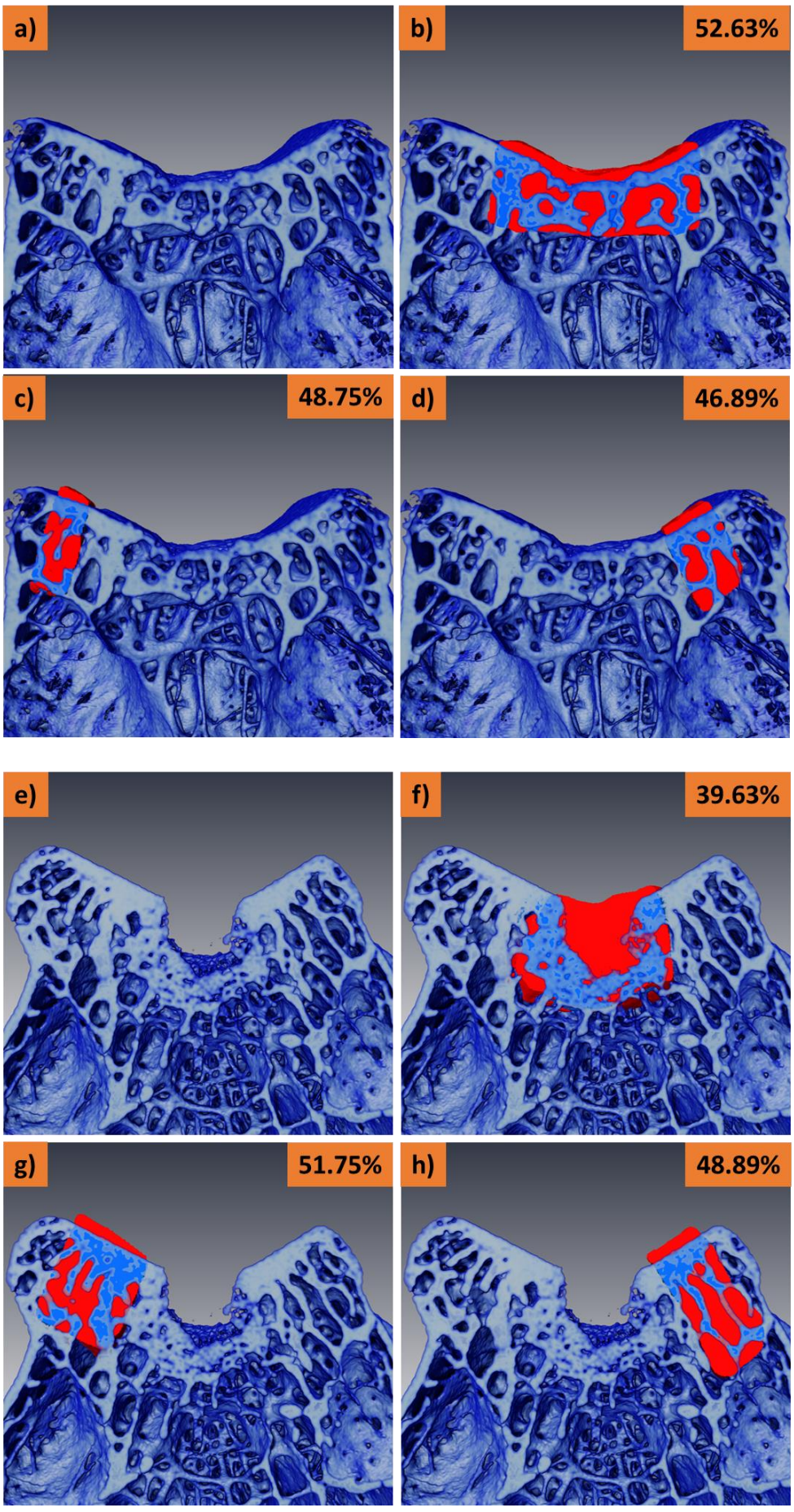
a)
b)
52.63%
c)
48.75%
d)
46.89%
e)
f)
39.63%
g)
51.75%
h)
48.89%

Figure 6.11 BV/TV after 4 months of implantation. a) The cross-sectional image of the experimental group from **Figure 6.9**, b) BV/TV calculation of the defect area using Avizo in the experimental group, c) and d) BV/TV calculation of the healthy joint area using Avizo in the experimental group, e) The cross-sectional image of the control group from **Figure 6.9**, f) BV/TV calculation of the defect area using Avizo in the control group, g) and h) BV/TV calculation of the healthy joint area using Avizo in the control group.

After 4 months of implantation, the BV/TV value was significantly increased in the experimental group, from 31.45% (after 2 months of implantation) to 52.63% (**Figure 6.11b**), which was approximately the same as BV/TV of the healthy joint (approximately 50% [**Figure 6.11c** and **6.11d**]). However, the BV/TV value was only slightly increased in the control group after 4 months, i.e. from 32.23% (after 2 months of implantation) to 39.63% (**Figure 6.11f**).

<u>3D evaluation of pore size distribution after 2 months of implantation</u>

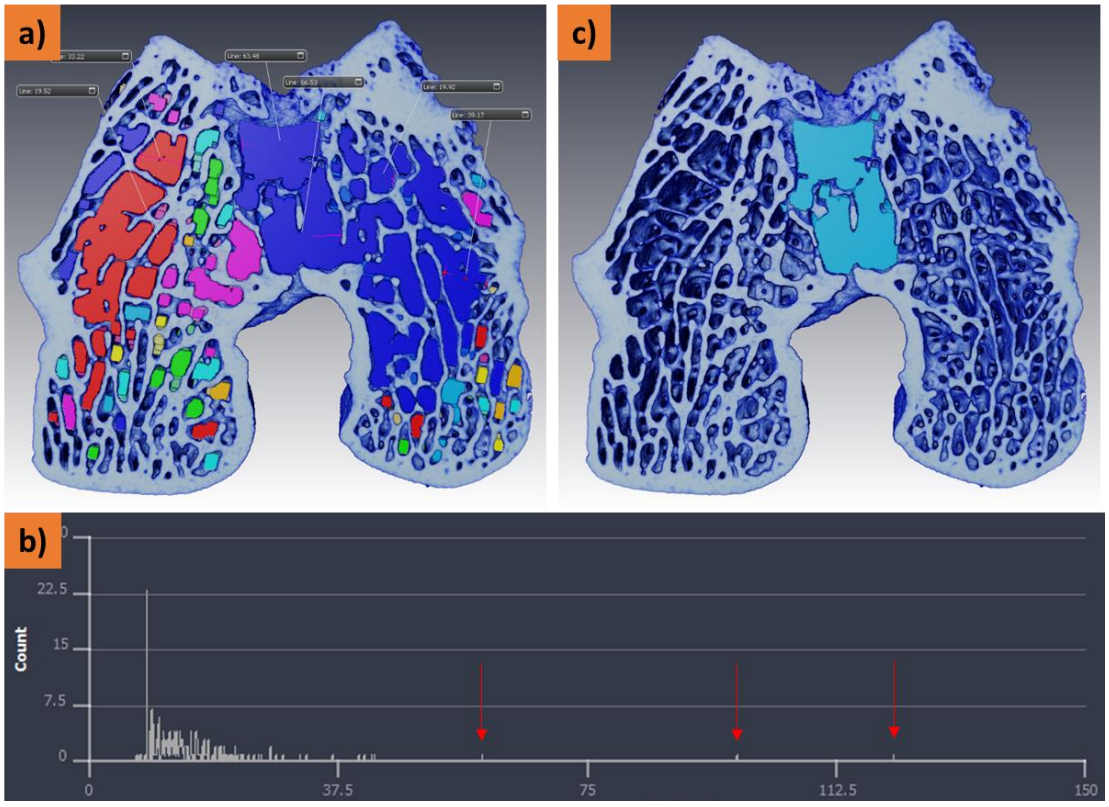

Figure 6.12 3D pore size determination of the repaired joint using Avizo. a) Hole filling, labelling and size calculation, b) Plot showing pore size distribution (count versus arbitrary unit), c) Pore size calculation in the defect region.

Pore size was determined using the segmentation function of Avizo. The results are demonstrated in **Figure 6.12**, which shows that most pores (number of pores = number of counts) were in the range of 0–40 arbitrary units. However, three pores had a significantly larger arbitrary unit as demonstrated by the red arrow in **Figure 6.12b**, which were later confirmed to be the pores from the defect region as shown in **Figure 6.12c**. The pore size of the defect region was significantly larger than that of the healthy region. This finding indicated that pore size distribution could be further improved after 2 months of implantation.

3D evaluation of pore size distribution after 4 months of implantation

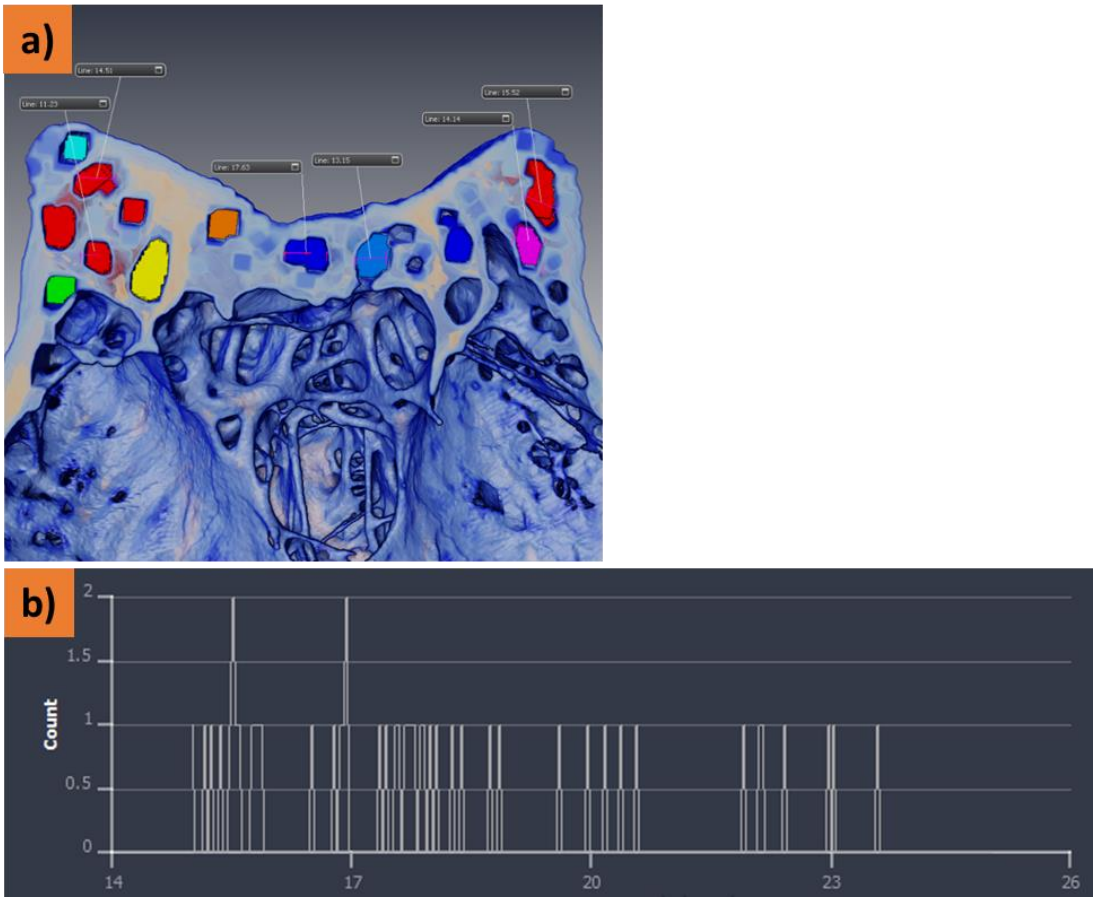

Figure 6.13 3D pore size determination using Avizo. a) Hole filling, labelling and size calculation, b) Plot showing pore size distribution (count versus arbitrary unit).

The pore size distribution after 4 months of implantation is shown in **Figure 6.13**; all pores were in the range of 14–26 arbitrary units in an evenly distributed pattern. This finding indicated that the pore size distribution was significantly improved as compared with that observed after 2 months of implantation. In addition, the pore size of the defect region was almost the same as that of the healthy region, which indicated a regenerated osteochondral joint with an even pore size distribution similar to that of the healthy tissue.

6.3.3 In vivo histological analysis

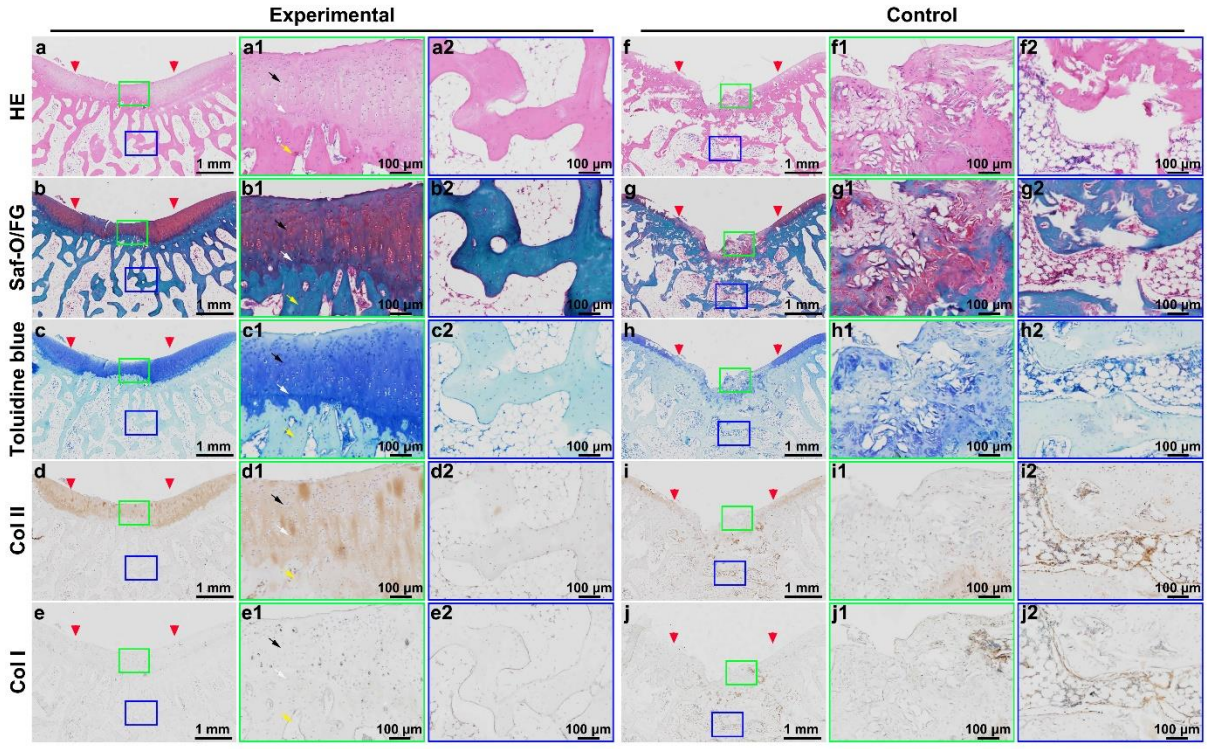

Figure 6.14 Histological evaluation of repaired tissue after 4 months of implantation in the experimental and control groups. H&E staining in the experimental (a–a2) and control (f–f2) groups. Safranin O/Fast Green staining in the experimental (b–b2) and control (g–g2) groups. Toluidine blue staining in the experimental (c–c2) and control (h–h2) groups. Collagen II staining in the experimental (d–d2) and control (i–i2)

groups. Collagen I staining in the experimental (e–e2) and control (j–j2) groups. The black arrows indicate the neocartilage, the white arrows indicate the neocalcified cartilage, the yellow arrows indicate the neobone and the red arrows indicate the repaired and normal tissue.

H&E staining

The morphology of the newly generated osteochondral matrix was assessed using H&E staining. In the experimental group (**Figure 6.14A1)**, two distinct structural regions were observed. Cells exhibited distinct morphological features depending on their location, gradually transitioning from saturated staining in the superficial region to even distribution of staining in the cartilage region. In addition, higher porosity was observed in the bone region. However, in the control group (**Figure 6.14A2**), both cartilage and bone regions were irregularly stained. In addition, fissures, residual void spaces and poor bone repair were observed. Moreover, it was hard to distinguish between the two regions in the control group.

In addition, cells were homogeneously distributed throughout the scaffold, which indicated an advantage over the cell-based scaffold approach that requires two surgeries with a long in vitro cell culture period to ensure cellularisation before implantation.[154]

Safranin O/Fast Green staining

As demonstrated in **Figure 6.14B1**, H&E staining of the cartilage region was confirmed based on the high intensity of safranin O staining in the region. The bone region, however, was only stained with Fast Green. The interface region that demonstrated some colour overlap was stained both red (safranin O) and blue (Fast Green). This mixed staining of the interface region was also observed in the surrounding healthy region, confirming that both chondrogenesis and osteogenesis occurred in the

interface region. However, as shown in **Figure 6.14B2**, safranin O-stained red region was irregular and not uniform corresponding to the fibrous cartilage tissue observed via microscopic evaluation.

Toluidine blue and type II collagen

As shown in **Figure 6.14C1** and **6.14D1**, the cartilage region was stained blue (toluidine blue) and yellow (type II collagen) at a high intensity, confirming the regeneration of proteoglycans and type II collagen.

Magnified images

H&E staining

To further explore the microstructural features of the repaired joints, images of H&E staining (**Figure 6.14**) were magnified and are illustrated in **Figure 6.15**.

As shown in **Figure 6.15a**, typical features of cartilage were observed in the healthy tissue. In the superficial layer, flattened/elongated cells were found near the cartilage surface, which contributed to the mechanical property of the cartilage matrix. In the middle layer, cell density was relatively low. Unlike the cells in the superficial layer, the cells in the middle layer were round.

In the experimental group (**Figure 6.15b**), many features similar to those of the healthy tissue were observed, including high cell density and flattened/elongated cells in the superficial layer and lower cell density in the middle layer. However, cells were not observed in a region of the top layer. We speculated that cartilage regeneration in this

region was the formation of fibrocartilage instead of healthy cartilage. In the control group (**Figure 6.15c**), however, an unstructured cartilage landscape was found; however, it was difficult to identify any interface layer between the superficial and middle layers, and any specific cell morphological features were not observed.

a) Healthy Tissue

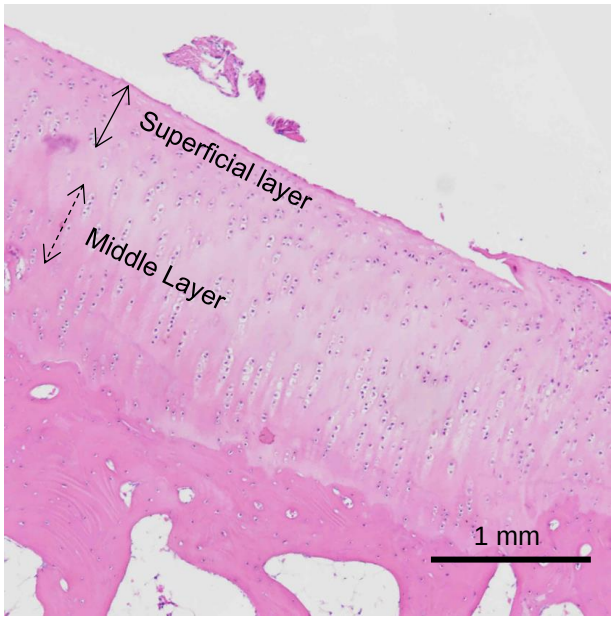

b) Experimental Group

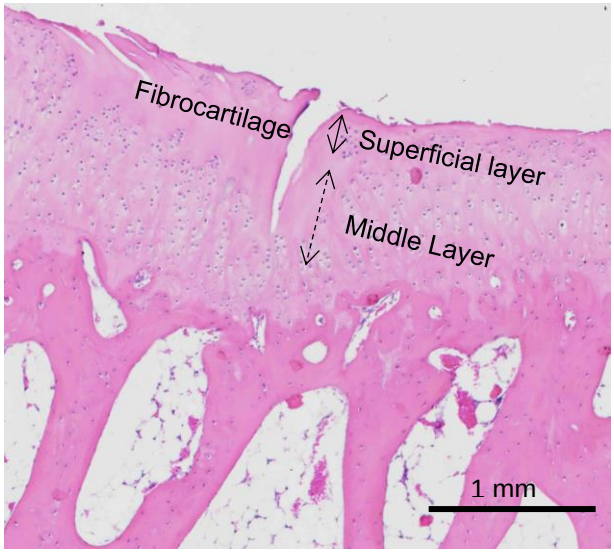

c) Control Group

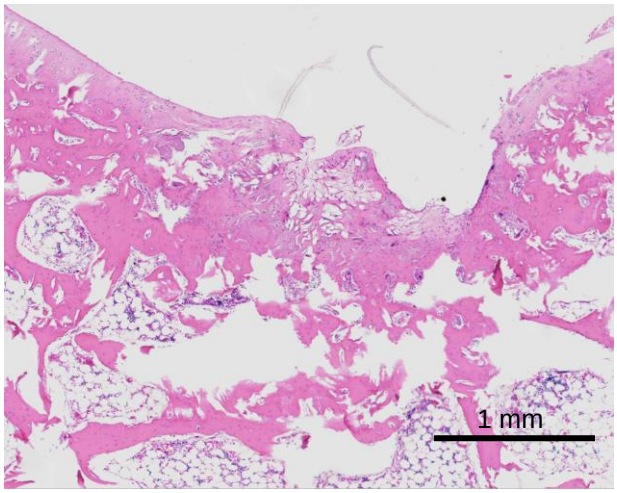

Figure 6.15 Magnification (100x) of the images of H&E staining from **Figure 6.15**. a) H&E staining of the healthy tissue, b) H&E staining of the regenerated region in the experimental group, c) H&E staining in the control group.

Safranin O/Fast Green staining

To further investigate the differentiation features in both cartilage and bone regions, images in **Figure 6.14** were magnified.

In the healthy tissue, a purple-coloured calcified layer was observed (**Figure 6.16a**). This partially calcified layer provided a buffer with intermediate mechanical properties between the uncalcified cartilage and subchondral bone layers. Cells in this calcified cartilage layer were unique because they could synthesise collagen type X and calcify the ECM. This interface layer contributed to excellent structural integration. In addition, tidemark was observed (**Figure 6.16a**, the distinguishing line between the deep cartilage and calcified cartilage layers) that played an important role in limiting vascularisation from bone to cartilage.

In the experimental group, as shown in **Figure 6.16b**, the features of the calcified cartilage layer and tidemark were similar to those of the healthy tissue, demonstrating that the regenerated tissue had a sophisticated multi-layered structure. In addition, the

morphological features and pore size of the regenerated bone were similar to those of the healthy bone. In the control group (**Figure 6.16c**), however, the repaired matrix was unstructured, and the interfacial layer was hardly observed. Moreover, tidemark was not observed, and the subchondral bone repair was incomplete.

a) Healthy Tissue

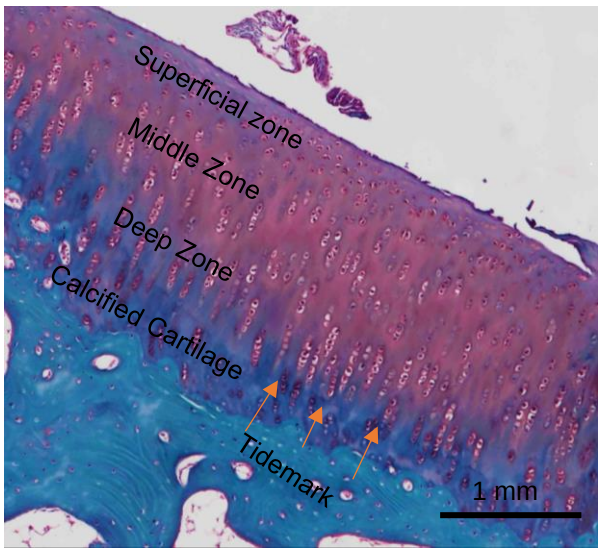

b) Experimental group

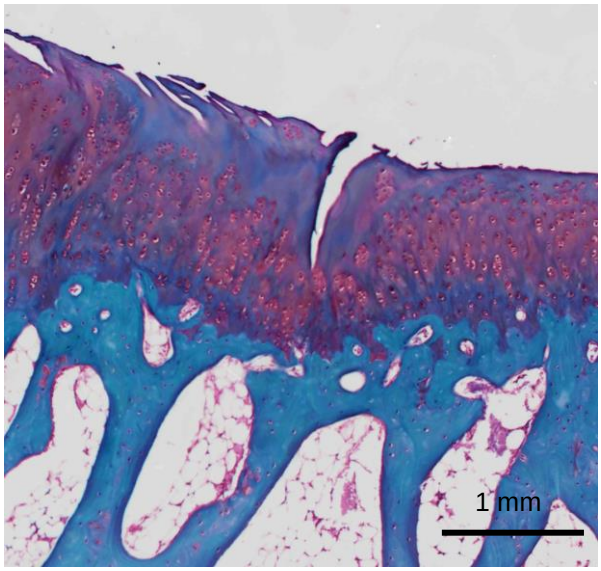

c) Control group

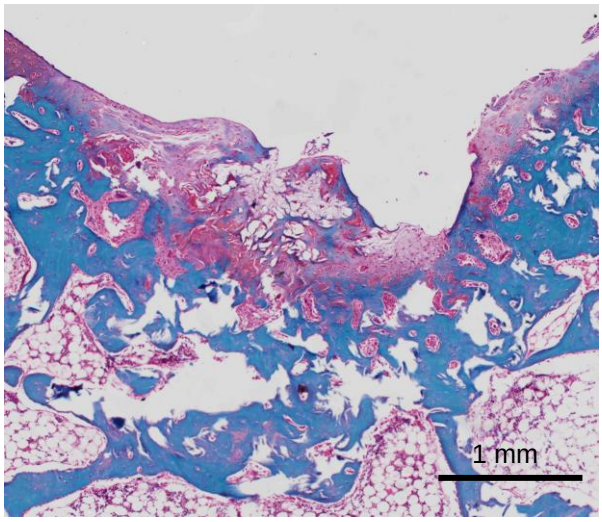

Figure 6.16 Magnified Safranin O/FG staining images from **Figure 6.15**, a) Safranin O/FG staining of the healthy tissue, b) Safranin O/FG staining of the regenerated tissue in the experimental group, c) Safranin O/FG staining in the control group.

Collagen type II staining

To further investigate the collagen content and its distribution, images from **Figure 6.14** were magnified. In the healthy tissue (**Figure 6.17a**), the content of collagen type II was the highest in the calcified cartilage layer, which is consistent with the findings of other related studies [25, 155]. In the experimental group (**Figure 6.17b**), the collagen content in the experimental group showed a roughly even distribution, unlike that in the healthy tissue. In the control group (**Figure 6.17c**), however, collagen type II staining was not observed.

a) Healthy Tissue

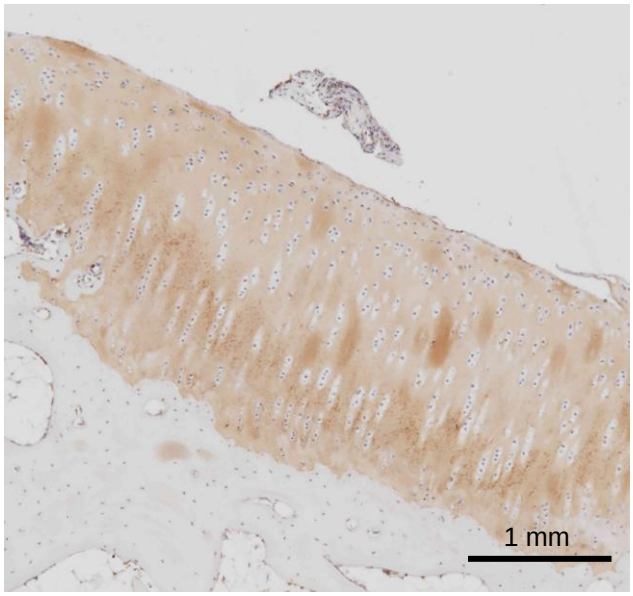

b) Experimental group

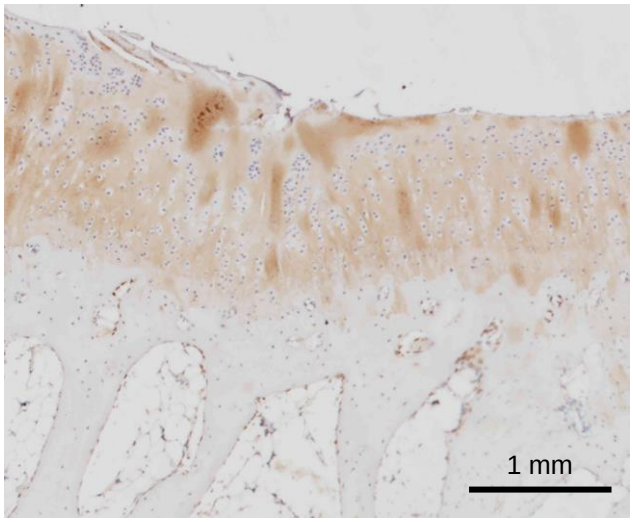

c) Control

No observable collagen type II staining results.

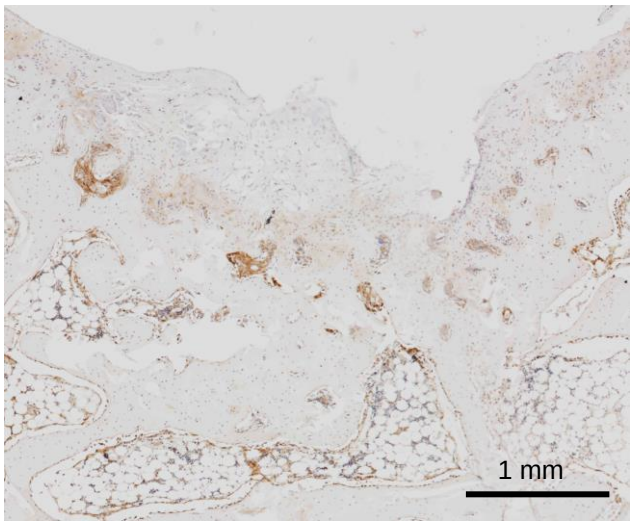

Figure 6.17 Magnified images of collagen type II staining from **Figure 6.14**. a) Collagen type II staining of the healthy tissue, b) Collagen type II staining of the

regenerated region in the experimental group, c) Collagen type II staining in the control group.

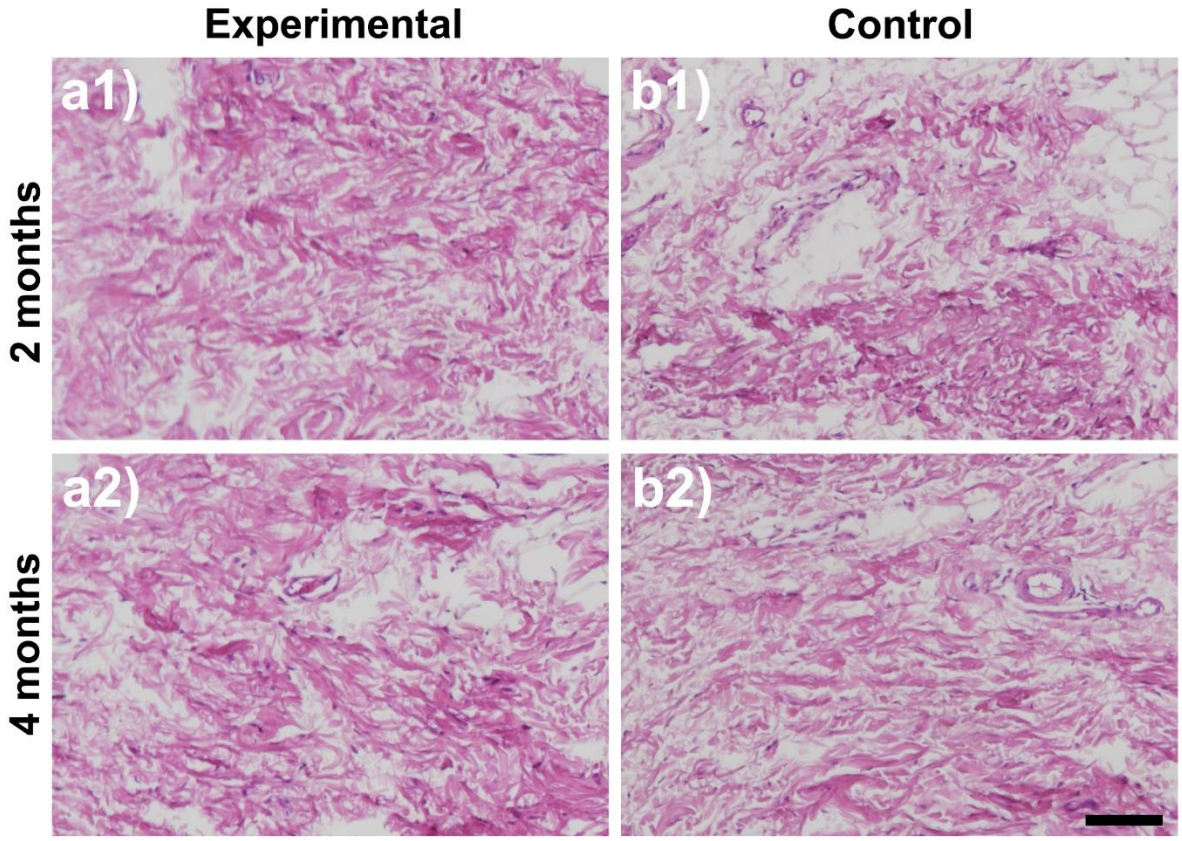

Figure 6.18. H&E staining of synovial membrane close to the regenerated joint after 2 and 4 months of implantation. Samples in both experimental and control groups revealed no inflammatory cells (scale bar = 100 μm).

Immune responses

We used monomeric collagen instead of fibrillar collagen to reduce immune responses against the scaffold. Unlike many previous studies that used fibrillar collagen from Sigma-Aldrich for making scaffolds, the scaffolds in this study were synthesised using monomeric collagen devoid of immunogenic peptides that elicit immune responses. For in vivo experiments, the scaffolds were implanted into rabbit knees at the defect region, and the results demonstrated that the scaffolds could aid in regenerating osteochondral joint with no signs of inflammation or synovial hyperplasia. Both gross

and histological evaluation further confirmed that no inflammatory responses were apparent after 2 and 4 months of implantation (**Figure 6.18**).

6.4 Discussion

The last and most important objective of this study was to determine whether the tri-layered scaffold could repair ODs in vivo. To date, studies in this field have focussed on regenerating a single tissue type, either bone or cartilage (Table 2.6, Chapter 2). Only a few studies have reported the simultaneous repair and regeneration of cartilage, calcified cartilage and bone (Table 2.7 and 2.8, Chapter 2).

After 2 months of implantation, the experimental group treated with the tri-layered scaffolds exhibited cartilage and bone repair to some extent, although a hole in the centre of the OD was visible. However, a large empty hole was visualised in the control group, with few newly formed tissues. Two-dimensional images of the cross-sections of the rabbit knees in the experimental group demonstrated that neocartilage was formed on the surface of the scaffold; however, approximately one-third of the scaffold length was yet to be covered with neotissue. Moreover, there was hardly any new tissue growth on the boundary, and the cartilage was barely repaired. Three-dimensional images of the knee joint cross-sections produced using Avizo were used to visualise bone regeneration in the bottom layer of the experimental group scaffolds and the control group without scaffolds. In the experimental group, neotissue formation was apparent in the bottom layer of the scaffold, although these new tissue networks were not as dense as those of the normal bone. However, bone regeneration was not observed in the control group. Furthermore, qualitative micro-CT assessment indicated that the BV/TV values were similar between the two groups (31.45% in the experimental group and 32.23% in the control group); however, the BV/TV values of

the two groups were significantly lower than those of the healthy joints (approximately 50%). This finding indicates that even with a scaffold, knees with ODs require longer than 2 months to regenerate tissues. These results were consistent with those of a previous study, which reported that more than 2 months are required to achieve a more satisfactory repair effect.[156]

After 4 months of implantation, hyaline-like repaired cartilage was found in the experimental group, and a hole was not observed. The regenerated cartilage and bone tissues were well integrated with the surrounding healthy tissue, and the boundary of the original defect was barely visible. However, a few newly grown fibrocartilage-like tissues surrounding the OD were observed in the control group, and a large hole was still visible in the OD region. The 2D cross-sectional images of ODs in the experimental group confirmed that the neotissue completely formed cartilaginous and osseous tissues, with no differences observed between the neotissue and the surrounding normal tissue. However, a large hole was visualised in the control group, and no significant improvement in tissue repair was observed since the 2-month post-surgery evaluation. The 2D cross-sectional images of the tissue in the control group revealed that a few new tissues were formed at the boundary of the OD, and the cartilage was hardly repaired after 4 months of implantation. This finding was similar to that observed after 2 months of implantation. Furthermore, the BV/TV value was significantly increased (from 31.45% after 2 months of implantation to 52.63% after 4 months of implantation) in the experimental group, and the value was similar to that of the healthy joints (approximately 50%). The control group, however, only showed little improvement in the BV/TV values (from 32.23% after 2 months of implantation to 39.63% after 4 months of implantation). Pore size distribution in the experimental group after

4 months of implantation is shown in Figure 6.10–6.14; all pores had a diameter of 14–26 μm and were evenly distributed throughout the scaffold. This significant improvement in pore size distribution after 4 months of implantation compared with 2 months of implantation indicated that the regenerated osteochondral tissue had features similar to those of the natural osteochondral tissue and developed between 2 and 4 months of implantation.

Micro-CT 3D reconstruction

To the best of our best knowledge, Avizo was used for the first time in this study to reconstruct 3D images of the regenerated osteochondral joint, particularly for a 3D cross-sectional view. To date, most researchers in this field have illustrated cross-sectional views of the repaired osteochondral joint using ImageJ (an image processing software), as shown in **Figure 6.19a**. However, in this study, we used Avizo to produce 3D cross-sectional images (**Figure 6.19b**). This novel approach benefited the results both qualitatively and quantitatively.

For qualitative assessment, Avizo was used to reconstruct images with better image quality so that a clear edge could be seen. The reconstructed images (reconstructed using all raw images produced via micro-CT, approximately several hundred images), demonstrated more intricate details than those revealed by 2D images processed via ImageJ (only selected as a single selected image). For example, in **Figure 6.19**, although the 2D image demonstrated some main features such as the regenerated cartilage, it failed to illustrate the regenerative process in the bone region (the regenerative bone region appeared empty in the 2D image, **Figure 6.19a**). Moreover,

the 3D reconstructed image demonstrated an ongoing bone regenerative process (the dark blue network in the red box in the 3D reconstructed image, **Figure 6.19b**).

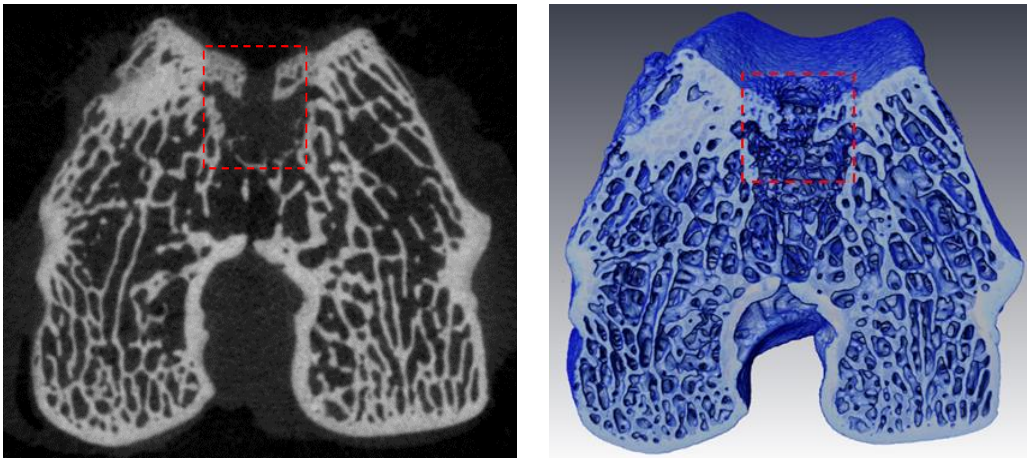

Figure 6.19 a) Two-dimensional cross-sectional image of the regenerated osteochondral joint of a rabbit model. The red dash-line box represents the regenerative region (scale = 4 mm × 4 mm), where the regenerated bone can hardly be seen, b) Three-dimensional cross-sectional image of the regenerative osteochondral joint in the same rabbit. The red dash-line box represents the regenerative region (scale = 4 mm × 4 mm), where the regenerated bone can be observed (the dark blue network in the red box is considered the newly regenerated bone tissue).

For quantitative assessment, Avizo was used for all mathematical calculations (including 3D-based BV/TV and pore size distribution mentioned previously) using all images/data produced via micro-CT (approximately several hundred images) instead of using a single selected 2D image in ImageJ. The enormously increased data input substantially contributed to the increased accuracy of the numerical results and reduced the level of selective biases.

Histological analysis

The newly regenerated osteochondral matrix was histologically characterised by H&E staining. Osteochondral regeneration with newly formed cartilage and bone was observed in the experimental group. The control group, however, showed irregular

staining in both cartilage and bone regions accompanied by fissures, residual void spaces and poor bone repair. In addition, it was difficult to distinguish between the cartilaginous and osseous regions in the control group.

To further explore the microstructural features of the repaired joints, magnified images of H&E-stained tissues were examined. In normal tissues, typical characteristics of cartilage were easily distinguishable owing to the presence of flattened/elongated cells near the cartilage surface. In the intermediate layer, cell density was relatively low, and the cells were round, unlike the flattened cells in the superficial layer. In the experimental group, cell density was high and cells were flat/elongated in the superficial layer, and cell density was low and cells were round in the intermediate layer. In the control group, however, an unstructured cartilage landscape was found, with unclear cell morphological features and almost no distinguishable differences between the superficial and intermediate layers. Moreover, previous studies have failed to achieve concurrent regeneration of the top cartilage, intermediate calcified cartilage and bottom bone layers[156], which was the remarkable advantage of the scaffold fabricated in this study.

Comparison with other studies

To achieve concurrent regeneration of cartilage, calcified cartilage and bone tissues, previous studies have designed several kinds of scaffolds, such as hydrogels, electrospinning film and 3D bio-printed scaffolds, to repair ODs [157-159]. However, the hydrogel scaffolds had several inherent drawbacks, including poor mechanical properties to withstand the stringent mechanical requirements during surgical implantation and in vivo incubation. In addition, most hydrogel scaffolds had low

porosity and resulted in insufficient cell infiltration, which prevented significant OD repair. Furthermore, electrospun membranes are limited by a compact structure and small pore size. In addition, it was difficult to fabricate a tri-layered scaffold to mimic the composition and microenvironment of cartilage, calcified cartilage and bone tissues using this approach, which hindered their simultaneous regeneration. Although 3D bioprinting is a precise technique to prepare tuneable and tailored scaffolds, it is complicated, time-consuming and laborious, which limited the ability of 3D bioprinted scaffolds to achieve a satisfactory OA repair effect. However, in the present study, we proposed a simple method to prepare a scaffold that can meet the requirements for OA regeneration.

In some studies, matured cartilage or cartilage–bone tissues were formed in vitro to repair ODs. However, the procedure for in vitro cultivation was complicated, time-consuming and laborious, and pollution was likely to be caused during cultivation. In addition, it was difficult to develop a tri-layered scaffold for concurrent regeneration of cartilage, calcified cartilage and bone tissues using this approach.[9, 160] Consequently, the scaffold designed in this study offers advantages over scaffolds developed in previous studies to effectively achieve concurrent regeneration of cartilage, calcified cartilage and bone tissues.

Effective tissue regeneration requires the successful identification of a suitable scaffolding strategy. An optimal tissue engineering scaffold should mimic both structure and composition of the tissue being regenerated. Both fibrous tissue and cartilage are primarily composed of collagen. Most currently available commercial collagen preparations are composed of animal tissue-derived type I collagen, which

has the potential to be immunogenic when implanted *in vivo*.[161] Atelocollagen is a theoretically non-immunogenic form of collagen that is prepared using pepsin to facilitate telopeptide removal. In addition, atelocollagen is insoluble and can be readily purified, exhibiting physical properties similar to those of natural collagen, which make it ideal for use in tissue regeneration applications.

Limitations and future improvements for in vivo studies

Although this study yielded significant results, it has some limitations that need to be investigated further. For example, it may be possible to develop scaffolds with more than three layers to mimic the structure of natural joints more precisely. For instance, the cartilage layer in the natural joint tissues can be further divided into three sublayers (superficial, middle and deep layers) with different collagen and CS contents, and the subchondral bone layer can be further divided into two sublayers (subchondral bone plate and subchondral spongiosa). In addition, fabrication process used in this study for making the interface layer can be further optimised. Although clear evidence of the formation of the interface layer was found using a simple liquid-co-synthesis interdiffusion method for scaffold fabrication, a more quantitative approach to evaluate these interfaces should be developed to reduce batch-to-batch variations in scaffold formation. Furthermore, the elastic properties of the calcified cartilage and subchondral bone layers of the tri-layered scaffold should be improved. Both these layers in the designed scaffold could handle approximately 3% elastic strain, suggesting that surgeons only have a 3% leeway while press-fitting the scaffold during implantation. Moreover, the performance of the tri-layered scaffold requires to be validated in higher animals. Although we have successfully demonstrated that the

scaffold can help to repair ODs in rabbits, we need to further assess the ability of these scaffolds to repair ODs in higher animals such as horses and sheep.

6.5 Summary

Based on in vivo studies, we found that the tri-layered scaffold repaired ODs in rabbits. The results of qualitative and quantitative analyses were much better in the experimental group than in the control group after 2 and 4 months of implantation. The key findings are summarised as follows:

1. The scaffold demonstrated excellent clinical effectiveness in terms of both morphological features (micro-CT imaging) and biological components (histological analysis) in a rabbit model after 4 months of implantation.

2. The repair effect after 4 months of in vivo implantation was elevated compared with 2 months of in vivo implantation.

3. Three-dimensional micro-CT image reconstruction is a very effective technique for knee observation, which is much better than the traditional 2D image processed using ImageJ. It specifically reflected the extent of bone repair in the experimental and control groups.

Therefore, higher animals and longer duration of study should be used to assess the clinical potential of the tri-layered scaffold designed in this study.

Chapter 7. Conclusions

The main findings of this thesis are summarised as following:

- Scaffold design and manufacturing

  Although multi-layered scaffolds have been developed by quite a few researchers in this field, integration between scaffold layers is still not widely adopted. We successfully designed and manufactured a tri-layered scaffold with gradient interface that is essential for suppressing delamination by providing cohesion between layers.

- Mechanics

  The tri-layered scaffold with gradient interfaces was proven mechanically superior to the scaffolds in the control group. Scaffolds in the control group delaminated at the interface between the bottom and middle layers, whereas the tri-layered scaffolds delaminated at their weakest bottom layer under the stress of 4.64 kPa (Section 4.3.5).

- In-vitro studies

  Each layer of the scaffold exhibited directional differentiation into three tissues. The cartilage layer promoted chondrogenic differentiation, the middle layer enhanced calcified cartilage formation and the bone layer promoted osteogenic differentiation (Section 5.3.4 and 5.3.5). Notably, the distinguished middle layer exhibited apparent bioactive activity that was different from that of the cartilage and bone layers, which indicated that the middle layer not only contributed to mechanical superiority but also promoted biological function for precise osteochondral repair.

- In-vivo studies

  After 4 months of implantation, hyaline-like cartilage was formed in the experimental group with no observable hole. However, a large hole was found in

the OD of the control group (Section 6.3.1). Histological analysis (Section 6.3.3) revealed excellent clinical repair effect in the rabbit osteochondral tissue after 4 months of implantation.

Although this study yielded significant results, the following aspects of this study can be investigated further:

Scaffold design and manufacturing

- Scaffolds with more layers can be developed to imitate the natural joint more precisely. For example, the cartilage layer can be further divided into three sublayers including the superficial, middle and deep layers with different collagen and CS contents. The subchondral bone layer can be further divided into two sublayers including the subchondral bone plate and subchondral spongiosa.
- The scaffold fabrication process for making the interface can be further optimised. Although an interface can be formed using a simple liquid-phase co-synthesis interdiffusion method, a more quantitative controlled approach should be developed to reduce batch-to-batch variations.

Mechanical properties

- The elastic property of the calcified cartilage and subchondral bone layers of the tri-layered scaffold (type I collagen + HAP) should be improved.

Biological properties

- The tri-layered scaffold should be validated in larger animals. We successfully demonstrated that the scaffold demonstrated repair effects in rabbits. Therefore, further studies should be conducted to assess the ability of the scaffold to repair ODs in higher animals such as horses and sheep.

References

[1] G. Jacob, K. Shimomura, N. Nakamura, Osteochondral Injury, Management and Tissue Engineering Approaches, Front Cell Dev Biol 8 (2020) 580868.

[2] M. Lemoine, S.M. Casey, J.M. O'Byrne, D.J. Kelly, F.J. O'Brien, The development of natural polymer scaffold-based therapeutics for osteochondral repair, Biochem Soc Trans 48(4) (2020) 1433-1445.

[3] J. Liao, T. Tian, S. Shi, X. Xie, Q. Ma, G. Li, Y. Lin, The fabrication of biomimetic biphasic CAN-PAC hydrogel with a seamless interfacial layer applied in osteochondral defect repair, Bone research 5(1) (2017) 1-15.

[4] A. Sibilska, A. Goralczyk, K. Hermanowicz, K. Malinowski, Spontaneous osteonecrosis of the knee: what do we know so far? A literature review, Int Orthop 44(6) (2020) 1063-1069.

[5] E.A. Makris, A.H. Gomoll, K.N. Malizos, J.C. Hu, K.A. Athanasiou, Repair and tissue engineering techniques for articular cartilage, Nature Reviews Rheumatology 11(1) (2015) 21.

[6] M.L. Redondo, A.J. Beer, A.B. Yanke, Cartilage Restoration: Microfracture and Osteochondral Autograft Transplantation, J Knee Surg 31(3) (2018) 231-238.

[7] L. Andriolo, G. Merli, G. Filardo, M. Marcacci, E. Kon, Failure of Autologous Chondrocyte Implantation, Sports Med Arthrosc Rev 25(1) (2017) 10-18.

[8] D.L. Richter, J.A. Tanksley, M.D. Miller, Osteochondral Autograft Transplantation: A Review of the Surgical Technique and Outcomes, Sports Med Arthrosc Rev 24(2) (2016) 74-8.

[9] A. He, L. Liu, X. Luo, Y. Liu, Y. Liu, F. Liu, X. Wang, Z. Zhang, W. Zhang, W. Liu, Y. Cao, G. Zhou, Repair of osteochondral defects with in vitro engineered cartilage

based on autologous bone marrow stromal cells in a swine model, Sci Rep 7 (2017) 40489.

[10] A. Sessa, F. Perdisa, A. Di Martino, S. Zaffagnini, G. Filardo, Cell-Free Biomimetic Osteochondral Scaffold: Implantation Technique, JBJS Essent Surg Tech 9(3) (2019) e27.

[11] R. Cao, A. Zhan, Z. Ci, C. Wang, Y. She, Y. Xu, K. Xiao, H. Xia, L. Shen, D. Meng, C. Chen, A Biomimetic Biphasic Scaffold Consisting of Decellularized Cartilage and Decalcified Bone Matrixes for Osteochondral Defect Repair, Front Cell Dev Biol 9 (2021) 639006.

[12] T.J. Levingstone, E. Thompson, A. Matsiko, A. Schepens, J.P. Gleeson, F.J. O'Brien, Multi-layered collagen-based scaffolds for osteochondral defect repair in rabbits, Acta biomaterialia 32 (2016) 149-160.

[13] Y. Zhao, X. Ding, Y. Dong, X. Sun, L. Wang, X. Ma, M. Zhu, B. Xu, Q. Yang, Role of the Calcified Cartilage Layer of an Integrated Trilayered Silk Fibroin Scaffold Used to Regenerate Osteochondral Defects in Rabbit Knees, ACS Biomater Sci Eng 6(2) (2020) 1208-1216.

[14] Y. Huang, H. Fan, X. Gong, L. Yang, F. Wang, Scaffold With Natural Calcified Cartilage Zone for Osteochondral Defect Repair in Minipigs, Am J Sports Med 49(7) (2021) 1883-1891.

[15] Z. Qiao, M. Lian, Y. Han, B. Sun, X. Zhang, W. Jiang, H. Li, Y. Hao, K. Dai, Bioinspired stratified electrowritten fiber-reinforced hydrogel constructs with layer-specific induction capacity for functional osteochondral regeneration, Biomaterials 266 (2021) 120385.

[16] Y. Qi, W. Zhang, G. Li, L. Niu, Y. Zhang, R. Tang, G. Feng, An oriented-collagen scaffold including Wnt5a promotes osteochondral regeneration and cartilage interface integration in a rabbit model, FASEB J 34(8) (2020) 11115-11132.

[17] F. Poutoglidou, C. Pourzitaki, I. Dardalas, E. Manthou Mu, E. Samoladas, D. Kouvelas, The Use of Collagen-Induced Arthritis Animal Model on Studying Bone Metabolism, Calcif Tissue Int 107(2) (2020) 109-120.

[18] M. Zhu, X. He, C. Xin, Y. Zhu, Z. Liu, 3D printing of an integrated triphasic MBG-alginate scaffold with enhanced interface bonding for hard tissue applications, J Mater Sci Mater Med 31(12) (2020) 113.

[19] L.Q. Lin, Y.W. Xu, Y.Q. Li, X.D. Gong, M. Wei, W. Zhang, X. Zhang, Y. Xu, Nanofibrous Wharton's jelly scaffold in combination with adipose-derived stem cells for cartilage engineering, Mater Design 186 (2020).

[20] Y. Xu, D. Li, Z. Yin, A. He, M. Lin, G. Jiang, X. Song, X. Hu, Y. Liu, J. Wang, X. Wang, L. Duan, G. Zhou, Tissue-engineered trachea regeneration using decellularized trachea matrix treated with laser micropore technique, Acta Biomater 58 (2017) 113-121.

[21] A. Di Luca, C. Van Blitterswijk, L. Moroni, The osteochondral interface as a gradient tissue: from development to the fabrication of gradient scaffolds for regenerative medicine, Birth Defects Research Part C: Embryo Today: Reviews 105(1) (2015) 34-52.

[22] P.D. Tatman, W. Gerull, S. Sweeney-Easter, J.I. Davis, A.O. Gee, D.-H. Kim, Multiscale biofabrication of articular cartilage: bioinspired and biomimetic approaches, Tissue Engineering Part B: Reviews 21(6) (2015) 543-559.

[23] Y. Yang, Z. Chen, X. Song, Z. Zhang, J. Zhang, K.K. Shung, Q. Zhou, Y. Chen, Biomimetic Anisotropic Reinforcement Architectures by Electrically Assisted Nanocomposite 3D Printing, Adv Mater 29(11) (2017).

[24] K. Marycz, A. Smieszek, S. Targonska, S.A. Walsh, K. Szustakiewicz, R.J. Wiglusz, Three dimensional (3D) printed polylactic acid with nano-hydroxyapatite doped with europium(III) ions (nHAp/PLLA@Eu(3+)) composite for osteochondral defect regeneration and theranostics, Mater Sci Eng C Mater Biol Appl 110 (2020) 110634.

[25] A.R. Poole, T. Kojima, T. Yasuda, F. Mwale, M. Kobayashi, S. Laverty, Composition and structure of articular cartilage: a template for tissue repair, Clinical Orthopaedics and Related Research® 391 (2001) S26-S33.

[26] L. Henao-Murillo, M.I. Pastrama, K. Ito, C.C. van Donkelaar, The Relationship Between Proteoglycan Loss, Overloading-Induced Collagen Damage, and Cyclic Loading in Articular Cartilage, Cartilage (2019) 1947603519885005.

[27] S.D. Ulrich, B.G. Parks, M.A. Tsai, S.D. Miller, Distribution of Subchondral Bone Puncture Strength in the Talus and Tibial Plafond: A Biomechanical Study, Foot Ankle Spec 11(1) (2018) 44-48.

[28] M.L. Vainieri, D. Wahl, M. Alini, G. van Osch, S. Grad, Mechanically stimulated osteochondral organ culture for evaluation of biomaterials in cartilage repair studies, Acta Biomater 81 (2018) 256-266.

[29] M. Boi, G. Marchiori, M. Berni, A. Gambardella, F. Salamanna, A. Visani, M. Bianchi, M. Fini, G. Filardo, Nanoindentation: An advanced procedure to investigate osteochondral engineered tissues, J Mech Behav Biomed Mater 96 (2019) 79-87.

[30] I. Redler, V. Mow, M.L. Zimny, J. Mansell, The ultrastructure and biomechanical significance of the tidemark of articular cartilage, Clinical orthopaedics and related research (112) (1975) 357-362.

[31] M.K. Boushell, C.T. Hung, E.B. Hunziker, E.J. Strauss, H.H. Lu, Current strategies for integrative cartilage repair, Connective tissue research 58(5) (2017) 393-406.

[32] T.J. Levingstone, A. Ramesh, R.T. Brady, P.A.J. Brama, C. Kearney, J.P. Gleeson, F.J. O'Brien, Cell-free multi-layered collagen-based scaffolds demonstrate layer specific regeneration of functional osteochondral tissue in caprine joints, Biomaterials 87 (2016) 69-81.

[33] T.J. Levingstone, E. Thompson, A. Matsiko, A. Schepens, J.P. Gleeson, F.J. O'Brien, Multi-layered collagen-based scaffolds for osteochondral defect repair in rabbits, Acta Biomater 32 (2016) 149-160.

[34] G. Chen, N. Kawazoe, Porous Scaffolds for Regeneration of Cartilage, Bone and Osteochondral Tissue, Adv Exp Med Biol 1058 (2018) 171-191.

[35] D.R. Pereira, R.L. Reis, J.M. Oliveira, Layered Scaffolds for Osteochondral Tissue Engineering, Adv Exp Med Biol 1058 (2018) 193-218.

[36] F. Gao, Z. Xu, Q. Liang, H. Li, L. Peng, M. Wu, X. Zhao, X. Cui, C. Ruan, W. Liu, Osteochondral Regeneration with 3D-Printed Biodegradable High-Strength Supramolecular Polymer Reinforced-Gelatin Hydrogel Scaffolds, Adv Sci (Weinh) 6(15) (2019) 1900867.

[37] S. Chen, P. Fu, H. Wu, M. Pei, Meniscus, articular cartilage and nucleus pulposus: a comparative review of cartilage-like tissues in anatomy, development and function, Cell Tissue Res 370(1) (2017) 53-70.

[38] H. Madry, C.N. van Dijk, M. Mueller-Gerbl, The basic science of the subchondral bone, Knee surgery, sports traumatology, arthroscopy 18(4) (2010) 419-433.

[39] Y. Xu, H. Duan, Y.Q. Li, Y.L. She, J.J. Zhu, G.D. Zhou, G.N. Jiang, Y. Yang, Nanofibrillar Decellularized Wharton's Jelly Matrix for Segmental Tracheal Repair, Adv Funct Mater 30(14) (2020).

[40] Y. Xu, Y.F. Guo, Y.Q. Li, Y.Y. Huo, Y.L. She, H. Li, Z.H. Jia, G.N. Jiang, G.D. Zhou, Z.W. You, L. Duan, Biomimetic Trachea Regeneration Using a Modular Ring Strategy Based on Poly(Sebacoyl Diglyceride)/Polycaprolactone for Segmental Trachea Defect Repair, Adv Funct Mater 30(42) (2020).

[41] W.M. Chen, Y. Xu, Y.Q. Li, L.T. Jia, X.M. Mo, G.N. Jiang, G.D. Zhou, 3D printing electrospinning fiber-reinforced decellularized extracellular matrix for cartilage regeneration, Chem Eng J 382 (2020).

[42] Y. Luo, D. Sinkeviciute, Y. He, M. Karsdal, Y. Henrotin, A. Mobasheri, P. Onnerfjord, A. Bay-Jensen, The minor collagens in articular cartilage, Protein Cell 8(8) (2017) 560-572.

[43] R. Dong, Y.Y. Wu, L. Fang, J. Ying, L. Zhang, S.B. Xu, P.E. Wang, H.T. Jin, L.W. Xiao, P.J. Tong, [Research status of correlation between type IX collagen gene and musculoskeletal diseases], Zhongguo Gu Shang 32(1) (2019) 92-96.

[44] C.A. Knuth, E. Andres Sastre, N.B. Fahy, J. Witte-Bouma, Y. Ridwan, E.M. Strabbing, M.J. Koudstaal, J. van de Peppel, E.B. Wolvius, R. Narcisi, E. Farrell, Collagen type X is essential for successful mesenchymal stem cell-mediated cartilage formation and subsequent endochondral ossification, Eur Cell Mater 38 (2019) 106-122.

[45] A. Li, Y. Wei, C. Hung, G. Vunjak-Novakovic, Chondrogenic properties of collagen type XI, a component of cartilage extracellular matrix, Biomaterials 173 (2018) 47-57.

[46] W.M. Chen, Y. Xu, Y.Q. Liu, Z.X. Wang, Y.Q. Li, G.N. Jiang, X.M. Mo, G.D. Zhou, Three-dimensional printed electrospun fiber-based scaffold for cartilage regeneration, Mater Design 179 (2019).

[47] G. Han, U. Boz, M. Eriten, C.R. Henak, Glycosaminoglycan depletion increases energy dissipation in articular cartilage under high-frequency loading, J Mech Behav Biomed Mater 110 (2020) 103876.

[48] H. Osago, M. Kobayashi-Miura, Y. Hamasaki, N. Hara, M. Hiyoshi, M. Tsuchiya, Complete solubilization of cartilage using the heat-stable protease thermolysin for comprehensive GAG analysis, Anal Biochem 548 (2018) 115-118.

[49] X. Xu, Y. Liang, X. Li, K. Ouyang, M. Wang, T. Cao, W. Li, J. Liu, J. Xiong, B. Li, J. Xia, D. Wang, L. Duan, Exosome-mediated delivery of kartogenin for chondrogenesis of synovial fluid-derived mesenchymal stem cells and cartilage regeneration, Biomaterials 269 (2021) 120539.

[50] B.T. Graham, A.C. Moore, D.L. Burris, C. Price, Sliding enhances fluid and solute transport into buried articular cartilage contacts, Osteoarthritis Cartilage 25(12) (2017) 2100-2107.

[51] A. He, H. Xia, K. Xiao, T. Wang, Y. Liu, J. Xue, D. Li, S. Tang, F. Liu, X. Wang, W. Zhang, W. Liu, Y. Cao, G. Zhou, Cell yield, chondrogenic potential, and regenerated cartilage type of chondrocytes derived from ear, nasoseptal, and costal cartilage, J Tissue Eng Regen Med 12(4) (2018) 1123-1132.

[52] K. Athanasiou, M. Rosenwasser, J. Buckwalter, T. Malinin, V.C. Mow, Interspecies comparisons of in situ intrinsic mechanical properties of distal femoral cartilage, Journal of Orthopaedic Research 9(3) (1991) 330-340.

[53] R.Y. Hori, L. Mockros, Indentation tests of human articular cartilage, Journal of Biomechanics 9(4) (1976) 259-268.

[54] W. Hayes, L. Mockros, Viscoelastic properties of human articular cartilage, Journal of applied physiology 31(4) (1971) 562-568.

[55] M. Stolz, R. Raiteri, A. Daniels, M.R. VanLandingham, W. Baschong, U. Aebi, Dynamic elastic modulus of porcine articular cartilage determined at two different levels of tissue organization by indentation-type atomic force microscopy, Biophysical journal 86(5) (2004) 3269-3283.

[56] W.E. Brown, G.D. DuRaine, J.C. Hu, K.A. Athanasiou, Structure-function relationships of fetal ovine articular cartilage, Acta Biomater 87 (2019) 235-244.

[57] K. Athanasiou, C.-F. Zhu, D. Lanctot, C. Agrawal, X. Wang, Fundamentals of biomechanics in tissue engineering of bone, Tissue engineering 6(4) (2000) 361-381.

[58] V. Karageorgiou, D. Kaplan, Porosity of 3D biomaterial scaffolds and osteogenesis, Biomaterials 26(27) (2005) 5474-5491.

[59] Y.M. SuchanekW, Processingandpropertiesof 070502015 年第 5 期 (46) 卷 hydroxyapatiteGbasedbiomaterialsforuseashardtissue replacementimplants, JMaterRes 13(1) (1998) 94G117.

[60] A.C. Lawson, J. Czernuszka, Collagen-calcium phosphate composites, Proceedings of the Institution of Mechanical Engineers, Part H: Journal of Engineering in Medicine 212(6) (1998) 413-425.

[61] R.K. Roeder, G.L. Converse, R.J. Kane, W. Yue, Hydroxyapatite-reinforced polymer biocomposites for synthetic bone substitutes, Jom 60(3) (2008) 38-45.

[62] S. Lopa, H. Madry, Bioinspired scaffolds for osteochondral regeneration, Tissue engineering Part A 20(15-16) (2014) 2052-2076.

[63] C.L. Wu, N.S. Harasymowicz, M.A. Klimak, K.H. Collins, F. Guilak, The role of macrophages in osteoarthritis and cartilage repair, Osteoarthritis Cartilage 28(5) (2020) 544-554.

[64] P. Chen, L. Zheng, Y. Wang, M. Tao, Z. Xie, C. Xia, C. Gu, J. Chen, P. Qiu, S. Mei, L. Ning, Y. Shi, C. Fang, S. Fan, X. Lin, Desktop-stereolithography 3D printing of a radially oriented extracellular matrix/mesenchymal stem cell exosome bioink for osteochondral defect regeneration, Theranostics 9(9) (2019) 2439-2459.

[65] S.B. Goodman, M.A. Wimmer, H.L. Ploeg, Recent advances in total joint replacement, J Orthop Res 38(7) (2020) 1413.

[66] H. Mistry, M. Connock, J. Pink, D. Shyangdan, C. Clar, P. Royle, R. Court, L.C. Biant, A. Metcalfe, N. Waugh, Autologous chondrocyte implantation in the knee: systematic review and economic evaluation, Health Technol Assess 21(6) (2017) 1-294.

[67] M. Krill, N. Early, J.S. Everhart, D.C. Flanigan, Autologous Chondrocyte Implantation (ACI) for Knee Cartilage Defects: A Review of Indications, Technique, and Outcomes, JBJS Rev 6(2) (2018) e5.

[68] B.B. Hinckel, A.H. Gomoll, Autologous Chondrocytes and Next-Generation Matrix-Based Autologous Chondrocyte Implantation, Clin Sports Med 36(3) (2017) 525-548.

[69] Y. Lin, T. Li, Y. Xiong, J. Li, W. Fu, [Research progress of rehabilitation after autologous chondrocyte implantation on knee], Zhongguo Xiu Fu Chong Jian Wai Ke Za Zhi 32(6) (2018) 758-763.

[70] S.P. Vajapey, R.E. Blackwell, A.J. Maki, T.L. Miller, Treatment of Extensor Tendon Disruption After Total Knee Arthroplasty: A Systematic Review, J Arthroplasty 34(6) (2019) 1279-1286.

[71] H. Khawar, S. Craxford, B. Ollivere, Radial head fractures, Br J Hosp Med (Lond) 81(4) (2020) 1-6.

[72] A.J. Krych, D.B.F. Saris, M.J. Stuart, B. Hacken, Cartilage Injury in the Knee: Assessment and Treatment Options, J Am Acad Orthop Surg 28(22) (2020) 914-922.

[73] Y.Q. Li, Y.Q. Liu, X.W. Xun, W. Zhang, Y. Xu, D.Y. Gu, Three-Dimensional Porous Scaffolds with Biomimetic Microarchitecture and Bioactivity for Cartilage Tissue Engineering, Acs Appl Mater Inter 11(40) (2019) 36359-36370.

[74] H.M. Aydin, A three‐layered osteochondral plug: Structural, mechanical, and in vitro biocompatibility analysis, Advanced Engineering Materials 13(12) (2011) B511-B517.

[75] H. Petite, K. Vandamme, L. Monfoulet, D. Logeart-Avramoglou, Strategies for improving the efficacy of bioengineered bone constructs: a perspective, Osteoporosis international 22(6) (2011) 2017-2021.

[76] H. Xuan, H. Hu, C. Geng, J. Song, Y. Shen, D. Lei, Q. Guan, S. Zhao, Z. You, Biofunctionalized chondrogenic shape-memory ternary scaffolds for efficient cell-free cartilage regeneration, Acta Biomater 105 (2020) 97-110.

[77] Y. Xu, Y. Li, Y. Liu, H. Li, Z. Jia, Y. Tang, G. Jiang, X. Zhang, L. Duan, Surface modification of decellularized trachea matrix with collagen and laser micropore technique to promote cartilage regeneration, Am J Transl Res 11(9) (2019) 5390-5403.

[78] M. Tamaddon, CHARACTERISATION OF COLLAGEN TYPE I / TYPE II COMPOSITE SCAFFOLDS FOR OSTEOCHONDRAL TISSUE ENGINEERING, (2014) 89.

[79] S. Yunoki, H. Sugiura, T. Ikoma, E. Kondo, K. Yasuda, J. Tanaka, Effects of increased collagen-matrix density on the mechanical properties and in vivo absorbability of hydroxyapatite–collagen composites as artificial bone materials, Biomedical Materials 6(1) (2011) 015012.

[80] E. Prosecká, M. Rampichová, A. Litvinec, Z. Tonar, M. Králíčková, L. Vojtova, P. Kochová, M. Plencner, M. Buzgo, A. Míčková, Collagen/hydroxyapatite scaffold enriched with polycaprolactone nanofibers, thrombocyte ‐ rich solution and mesenchymal stem cells promotes regeneration in large bone defect in vivo, Journal of Biomedical Materials Research Part A 103(2) (2015) 671-682.

[81] M. Tamaddon, R. Walton, D. Brand, J. Czernuszka, Characterisation of freeze-dried type II collagen and chondroitin sulfate scaffolds, Journal of Materials Science: Materials in Medicine 24(5) (2013) 1153-1165.

[82] J. Pieper, P. Van Der Kraan, T. Hafmans, J. Kamp, P. Buma, J. Van Susante, W. Van Den Berg, J. Veerkamp, T. Van Kuppevelt, Crosslinked type II collagen matrices: preparation, characterization, and potential for cartilage engineering, Biomaterials 23(15) (2002) 3183-3192.

[83] T. Fujisato, T. Sajiki, Q. Liu, Y. Ikada, Effect of basic fibroblast growth factor on cartilage regeneration in chondrocyte-seeded collagen sponge scaffold, Biomaterials 17(2) (1996) 155-162.

[84] W.-C. Chen, C.-L. Yao, Y.-H. Wei, I.-M. Chu, Evaluating osteochondral defect repair potential of autologous rabbit bone marrow cells on type II collagen scaffold, Cytotechnology 63(1) (2011) 13-23.

[85] W.C. Chen, Y.H. Wei, I.M. Chu, C.L. Yao, Effect of chondroitin sulphate C on the in vitro and in vivo chondrogenesis of mesenchymal stem cells in crosslinked type II collagen scaffolds, Journal of tissue engineering and regenerative medicine 7(8) (2013) 665-672.

[86] E. Kon, A. Mutini, E. Arcangeli, M. Delcogliano, G. Filardo, N. Nicoli Aldini, D. Pressato, R. Quarto, S. Zaffagnini, M. Marcacci, Novel nanostructured scaffold for

osteochondral regeneration: pilot study in horses, Journal of tissue engineering and regenerative medicine 4(4) (2010) 300-308.

[87] E. Kon, G. Filardo, F. Perdisa, A. Di Martino, M. Busacca, F. Balboni, A. Sessa, M. Marcacci, A one-step treatment for chondral and osteochondral knee defects: clinical results of a biomimetic scaffold implantation at 2 years of follow-up, Journal of Materials Science: Materials in Medicine 25(10) (2014) 2437-2444.

[88] J.-H. Ahn, T.-H. Lee, J.-S. Oh, S.-Y. Kim, H.-J. Kim, I.-K. Park, B.-S. Choi, G.-I. Im, A novel hyaluronate–atelocollagen/β-TCP–hydroxyapatite biphasic scaffold for the repair of osteochondral defects in rabbits, Tissue Engineering Part A 15(9) (2009) 2595-2604.

[89] T. Gotterbarm, W. Richter, M. Jung, S.B. Vilei, P. Mainil-Varlet, T. Yamashita, S.J. Breusch, An in vivo study of a growth-factor enhanced, cell free, two-layered collagen–tricalcium phosphate in deep osteochondral defects, Biomaterials 27(18) (2006) 3387-3395.

[90] Y. Qi, T. Zhao, K. Xu, T. Dai, W. Yan, The restoration of full-thickness cartilage defects with mesenchymal stem cells (MSCs) loaded and cross-linked bilayer collagen scaffolds on rabbit model, Molecular biology reports 39(2) (2012) 1231-1237.

[91] S.R. Frenkel, B. Toolan, D. Menche, M.I. Pitman, J.M. Pachence, Chondrocyte transplantation using a collagen bilayer matrix for cartilage repair, The Journal of bone and joint surgery. British volume 79(5) (1997) 831-836.

[92] A.M. Getgood, S.J. Kew, R. Brooks, H. Aberman, T. Simon, A.K. Lynn, N. Rushton, Evaluation of early-stage osteochondral defect repair using a biphasic scaffold based on a collagen–glycosaminoglycan biopolymer in a caprine model, The Knee 19(4) (2012) 422-430.

[93] A.K. Lynn, S.M. Best, R.E. Cameron, B.A. Harley, I.V. Yannas, L.J. Gibson, W. Bonfield, Design of a multiphase osteochondral scaffold. I. Control of chemical composition, Journal of Biomedical Materials Research Part A: An Official Journal of The Society for Biomaterials, The Japanese Society for Biomaterials, and The Australian Society for Biomaterials and the Korean Society for Biomaterials 92(3) (2010) 1057-1065.

[94] D. Grevenstein, D. Schafigh, S. Oikonomidis, P. Eysel, C. Brochhausen, C.K. Spies, J. Oppermann, Short-term radiological results after spheroid-based autologous chondrocyte implantation in the knee are independent of defect localisation, Technol Health Care (2021).

[95] D.R. Krueger, A.D.J. Baur, C. Perka, J.H. Schroeder, Injectable autologous chondrocyte implantation in acetabular cartilage defects: 2-year minimum clinical and MRI results, Arch Orthop Trauma Surg (2021).

[96] N.-J. Chang, C.-C. Lin, M.-Y. Shie, M.-L. Yeh, C.-F. Li, P.-I. Liang, K.-W. Lee, P.-H. Shen, C.-J. Chu, Positive effects of cell-free porous PLGA implants and early loading exercise on hyaline cartilage regeneration in rabbits, Acta biomaterialia 28 (2015) 128-137.

[97] T.J. Levingstone, A. Ramesh, R.T. Brady, P.A. Brama, C. Kearney, J.P. Gleeson, F.J. O'Brien, Cell-free multi-layered collagen-based scaffolds demonstrate layer specific regeneration of functional osteochondral tissue in caprine joints, Biomaterials 87 (2016) 69-81.

[98] S. Jia, J. Wang, T. Zhang, W. Pan, Z. Li, X. He, C. Yang, Q. Wu, W. Sun, Z. Xiong, Multilayered scaffold with a compact interfacial layer enhances osteochondral defect repair, ACS applied materials & interfaces 10(24) (2018) 20296-20305.

[99] T.J. Levingstone, A. Matsiko, G.R. Dickson, F.J. O'Brien, J.P. Gleeson, A biomimetic multi-layered collagen-based scaffold for osteochondral repair, Acta biomaterialia 10(5) (2014) 1996-2004.

[100] N.P. Camacho, P. West, P.A. Torzilli, R. Mendelsohn, FTIR microscopic imaging of collagen and proteoglycan in bovine cartilage, Biopolymers 62(1) (2001) 1-8.

[101] S. Saarakkala, L. Rieppo, J. Rieppo, J. Jurvelin, Fourier transform infrared (FTIR) microspectroscopy of immature, mature and degenerated articular cartilage, Microscopy: science, technology, applications and education 1 (2010) 403-14.

[102] M. Tamaddon, CHARACTERISATION OF COLLAGEN TYPE I / TYPE II COMPOSITE SCAFFOLDS FOR OSTEOCHONDRAL TISSUE ENGINEERING, (2014) 182-184.

[103] B.B. Doyle, E. Bendit, E.R. Blout, Infrared spectroscopy of collagen and collagen‐like polypeptides, Biopolymers: Original Research on Biomolecules 14(5) (1975) 937-957.

[104] B.A. Harley, A.K. Lynn, Z. Wissner‐Gross, W. Bonfield, I.V. Yannas, L.J. Gibson, Design of a multiphase osteochondral scaffold III: Fabrication of layered scaffolds with continuous interfaces, Journal of biomedical materials research Part A 92(3) (2010) 1078-1093.

[105] J. Bella, B. Brodsky, H.M. Berman, Hydration structure of a collagen peptide, Structure 3(9) (1995) 893-906.

[106] J. Bella, B. Brodsky, H.M. Berman, Disrupted collagen architecture in the crystal structure of a triple-helical peptide with a Gly→ Ala substitution, Connective tissue research 35(1-4) (1996) 401-406.

[107] F. Jiang, H. Hörber, J. Howard, D.J. Müller, Assembly of collagen into microribbons: effects of pH and electrolytes, Journal of structural biology 148(3) (2004) 268-278.

[108] J.H. Bowes, R. Kenten, The swelling of collagen in alkaline solutions. 1. Swelling in solutions of sodium hydroxide, Biochemical Journal 46(1) (1950) 1.

[109] S. Hattori, E. Adachi, T. Ebihara, T. Shirai, I. Someki, S. Irie, Alkali-treated collagen retained the triple helical conformation and the ligand activity for the cell adhesion via α2β1 integrin, The Journal of Biochemistry 125(4) (1999) 676-684.

[110] J.A. Wilson, W.H. Wilson, COLLOIDAL PHENOMENA AND THE ADSORPTION FORMULA, Journal of the American Chemical Society 40(6) (1918) 886-895.

[111] H. Susi, D.M. Byler, Protein structure by Fourier transform infrared spectroscopy: second derivative spectra, Biochemical and biophysical research communications 115(1) (1983) 391-397.

[112] M. Jackson, P.H. Watson, W.C. Halliday, H.H. Mantsch, Beware of connective tissue proteins: assignment and implications of collagen absorptions in infrared spectra of human tissues, Biochimica et Biophysica Acta (BBA)-Molecular Basis of Disease 1270(1) (1995) 1-6.

[113] S. Saarakkala, L. Rieppo, J. Rieppo, J. Jurvelin, Fourier transform infrared (FTIR) microspectroscopy of immature, mature and degenerated articular cartilage, Microscopy 1 (2010) 403-414.

[114] S. Akhshabi, E. Biazar, V. Singh, S.H. Keshel, N. Geetha, The effect of the carbodiimide cross-linker on the structural and biocompatibility properties of collagen–chondroitin sulfate electrospun mat, International journal of nanomedicine 13 (2018) 4405.

[115] A. Ficai, E. Andronescu, C. Ghitulica, G. Voicu, V. Trandafir, D. Mânzu, M. Ficai, S. Pall, Colagen/hydroxyapatite interactions in composite biomaterials, Materiale Plastice 46(1) (2009) 11-15.

[116] M.J. Gupte, W.B. Swanson, J. Hu, X. Jin, H. Ma, Z. Zhang, Z. Liu, K. Feng, G. Feng, G. Xiao, N. Hatch, Y. Mishina, P.X. Ma, Pore size directs bone marrow stromal cell fate and tissue regeneration in nanofibrous macroporous scaffolds by mediating vascularization, Acta Biomater 82 (2018) 1-11.

[117] Z. Chen, X. Yan, S. Yin, L. Liu, X. Liu, G. Zhao, W. Ma, W. Qi, Z. Ren, H. Liao, M. Liu, D. Cai, H. Fang, Influence of the pore size and porosity of selective laser melted Ti6Al4V ELI porous scaffold on cell proliferation, osteogenesis and bone ingrowth, Mater Sci Eng C Mater Biol Appl 106 (2020) 110289.

[118] A.I. Itälä, H.O. Ylänen, C. Ekholm, K.H. Karlsson, H.T. Aro, Pore diameter of more than 100 μm is not requisite for bone ingrowth in rabbits, Journal of Biomedical Materials Research: An Official Journal of The Society for Biomaterials, The Japanese Society for Biomaterials, and The Australian Society for Biomaterials and the Korean Society for Biomaterials 58(6) (2001) 679-683.

[119] N. Davidenko, C. Schuster, D. Bax, N. Raynal, R.W. Farndale, S.M. Best, R.E. Cameron, Control of crosslinking for tailoring collagen-based scaffolds stability and mechanics, Acta biomaterialia 25 (2015) 131-142.

[120] L.D. Guillen-Romero, M.T. Oropeza-Guzman, E.A. Lopez-Maldonado, A.L. Iglesias, J.A. Paz-Gonzalez, T. Ng, E. Serena-Gomez, L.J. Villarreal-Gomez, Synthetic hydroxyapatite and its use in bioactive coatings, J Appl Biomater Funct Mater 17(1) (2019) 2280800018817463.

[121] R.J. Kane, R.K. Roeder, Effects of hydroxyapatite reinforcement on the architecture and mechanical properties of freeze-dried collagen scaffolds, Journal of the mechanical behavior of biomedical materials 7 (2012) 41-49.

[122] E. Colaco, D. Brouri, N. Aissaoui, P. Cornette, V. Dupres, R.F. Domingos, J.F. Lambert, E. Maisonhaute, K.E. Kirat, J. Landoulsi, Hierarchical Collagen-Hydroxyapatite Nanostructures Designed through Layer-by-Layer Assembly of Crystal-Decorated Fibrils, Biomacromolecules 20(12) (2019) 4522-4534.

[123] B.A. Harley, J.H. Leung, E.C. Silva, L.J. Gibson, Mechanical characterization of collagen–glycosaminoglycan scaffolds, Acta biomaterialia 3(4) (2007) 463-474.

[124] F.T. Moutos, L.E. Freed, F. Guilak, A biomimetic three-dimensional woven composite scaffold for functional tissue engineering of cartilage, Nature materials 6(2) (2007) 162.

[125] W.H. Liang, B.L. Kienitz, K.J. Penick, J.F. Welter, T.A. Zawodzinski, H. Baskaran, Concentrated collagen ‐ chondroitin sulfate scaffolds for tissue engineering applications, Journal of Biomedical Materials Research Part A 94(4) (2010) 1050-1060.

[126] D.A. Wahl, Collagen-Hydroxyapatite Scaffolds for Bone Tissue Engineering, (2007) 132.

[127] B.A. Harley, A.K. Lynn, Z. Wissner ‐ Gross, W. Bonfield, I.V. Yannas, L.J. Gibson, Design of a multiphase osteochondral scaffold. II. Fabrication of a mineralized collagen–glycosaminoglycan scaffold, Journal of Biomedical Materials Research Part A: An Official Journal of The Society for Biomaterials, The Japanese Society for Biomaterials, and The Australian Society for Biomaterials and the Korean Society for Biomaterials 92(3) (2010) 1066-1077.

[128] G.S. Offeddu, J.C. Ashworth, R.E. Cameron, M.L. Oyen, Multi-scale mechanical response of freeze-dried collagen scaffolds for tissue engineering applications, journal of the mechanical behavior of biomedical materials 42 (2015) 19-25.

[129] Y.I. Matveev, V.Y. Grinberg, V. Tolstoguzov, The plasticizing effect of water on proteins, polysaccharides and their mixtures. Glassy state of biopolymers, food and seeds, Food Hydrocolloids 14(5) (2000) 425-437.

[130] G.A. Ateshian, H. Wang, A theoretical solution for the frictionless rolling contact of cylindrical biphasic articular cartilage layers, Journal of biomechanics 28(11) (1995) 1341-1355.

[131] G. Ateshian, W. Lai, W. Zhu, V. Mow, An asymptotic solution for the contact of two biphasic cartilage layers, Journal of biomechanics 27(11) (1994) 1347-1360.

[132] A. Giannakopoulos, Indentation of graded substrates, Thin Solid Films 332(1-2) (1998) 172-179.

[133] J.K. Sherwood, S.L. Riley, R. Palazzolo, S.C. Brown, D.C. Monkhouse, M. Coates, L.G. Griffith, L.K. Landeen, A. Ratcliffe, A three-dimensional osteochondral composite scaffold for articular cartilage repair, Biomaterials 23(24) (2002) 4739-4751.

[134] J.M. Moran, D. Pazzano, L.J. Bonassar, Characterization of polylactic acid polyglycolic acid composites for cartilage tissue engineering, Tissue Engineering 9(1) (2003) 63-70.

[135] G.K. Reddy, C.S. Enwemeka, A simplified method for the analysis of hydroxyproline in biological tissues, Clinical Biochemistry 29(3) (1996) 225-229.

[136] J.K. Chan, The wonderful colors of the hematoxylin–eosin stain in diagnostic surgical pathology, International journal of surgical pathology 22(1) (2014) 12-32.

[137] Ö.Ş. Çalışkan, Bioactive glycopeptide nanofibers for tissue regeneration applications, Bilkent University, 2016.

[138] H. PUCHTLER, S.N. Meloan, M.S. TERRY, On the history and mechanism of alizarin and alizarin red S stains for calcium, Journal of Histochemistry & Cytochemistry 17(2) (1969) 110-124.

[139] Y. Wang, D.J. Blasioli, H.-J. Kim, H.S. Kim, D.L. Kaplan, Cartilage tissue engineering with silk scaffolds and human articular chondrocytes, Biomaterials 27(25) (2006) 4434-4442.

[140] Y. Wang, U.-J. Kim, D.J. Blasioli, H.-J. Kim, D.L. Kaplan, In vitro cartilage tissue engineering with 3D porous aqueous-derived silk scaffolds and mesenchymal stem cells, Biomaterials 26(34) (2005) 7082-7094.

[141] L. Zou, Y. Luo, M. Chen, G. Wang, M. Ding, C.C. Petersen, R. Kang, F. Dagnaes-Hansen, Y. Zeng, N. Lv, A simple method for deriving functional MSCs and applied for osteogenesis in 3D scaffolds, Scientific reports 3 (2013) 2243.

[142] H. Li, R. Chen, Z. Jia, C. Wang, Y. Xu, C. Li, H. Xia, D. Meng, Porous fish collagen for cartilage tissue engineering, Am J Transl Res 12(10) (2020) 6107-6121.

[143] H.C. Zhou, R. Chen, J.P. Wang, J. Lu, T. Yu, X.B. Wu, S.C. Xu, Z.H. Li, C. Jie, R.F. Cao, Y.F. Yang, Y.Q. Li, D.P. Meng, Biphasic fish collagen scaffold for osteochondral regeneration (vol 195, 108947, 2020), Mater Design 197 (2021).

[144] F. Gao, Z.Y. Xu, Q.F. Liang, H.F. Li, L.Q. Peng, M.M. Wu, X.L. Zhao, X. Cui, C.S. Ruan, W.G. Liu, Osteochondral Regeneration with 3D-Printed Biodegradable High-Strength Supramolecular Polymer Reinforced-Gelatin Hydrogel Scaffolds, Adv Sci 6(15) (2019).

[145] F. Shapiro, S. Koide, M.J. Glimcher, Cell origin and differentiation in the repair of full-thickness defects of articular cartilage, The Journal of bone and joint surgery. American volume 75(4) (1993) 532-553.

[146] R.F. Canadas, R.P. Pirraco, J.M. Oliveira, R.L. Reis, A.P. Marques, Stem Cells for Osteochondral Regeneration, Adv Exp Med Biol 1059 (2018) 219-240.

[147] H. Favreau, L. Pijnenburg, J. Seitlinger, F. Fioretti, L. Keller, D. Scipioni, H. Adriaensen, S. Kuchler-Bopp, M. Ehlinger, D. Mainard, P. Rosset, G. Hua, L. Gentile, N. Benkirane-Jessel, Osteochondral repair combining therapeutics implant with mesenchymal stem cells spheroids, Nanomedicine 29 (2020) 102253.

[148] C.M. Murphy, A. Matsiko, M.G. Haugh, J.P. Gleeson, F.J. O'Brien, Mesenchymal stem cell fate is regulated by the composition and mechanical properties of collagen–glycosaminoglycan scaffolds, Journal of the mechanical behavior of biomedical materials 11 (2012) 53-62.

[149] D.E. Discher, P. Janmey, Y.-l. Wang, Tissue cells feel and respond to the stiffness of their substrate, Science 310(5751) (2005) 1139-1143.

[150] A.J. Engler, S. Sen, H.L. Sweeney, D.E. Discher, Matrix elasticity directs stem cell lineage specification, Cell 126(4) (2006) 677-689.

[151] R. McBeath, D.M. Pirone, C.M. Nelson, K. Bhadriraju, C.S. Chen, Cell shape, cytoskeletal tension, and RhoA regulate stem cell lineage commitment, Dev Cell 6(4) (2004) 483-95.

[152] L. Li, J. Li, J. Guo, H. Zhang, X. Zhang, C. Yin, L. Wang, Y. Zhu, Q. Yao, 3D molecularly functionalized cell‐free biomimetic scaffolds for osteochondral regeneration, Advanced Functional Materials 29(6) (2019) 1807356.

[153] L. Dai, Z. He, X. Zhang, X. Hu, L. Yuan, M. Qiang, J. Zhu, Z. Shao, C. Zhou, Y. Ao, One-step repair for cartilage defects in a rabbit model: a technique combining the perforated decalcified cortical-cancellous bone matrix scaffold with microfracture, The American journal of sports medicine 42(3) (2014) 583-591.

[154] M. Brittberg, Cell carriers as the next generation of cell therapy for cartilage repair: a review of the matrix-induced autologous chondrocyte implantation procedure, The American journal of sports medicine 38(6) (2010) 1259-1271.

[155] Y.H. An, K.L. Martin, Handbook of histology methods for bone and cartilage, Springer2003.

[156] Y. Li, Y. Xu, Y. Liu, Z. Wang, W. Chen, L. Duan, D. Gu, Decellularized cartilage matrix scaffolds with laser-machined micropores for cartilage regeneration and articular cartilage repair, Mater Sci Eng C Mater Biol Appl 105 (2019) 110139.

[157] Z. Chen, H. Xiao, H. Zhang, Q. Xin, H. Zhang, H. Liu, M. Wu, L. Zuo, J. Luo, Q. Guo, C. Ding, H. Tan, J. Li, Heterogenous hydrogel mimicking the osteochondral ECM applied to tissue regeneration, J Mater Chem B (2021).

[158] H. Ding, Y. Cheng, X. Niu, Y. Hu, Application of electrospun nanofibers in bone, cartilage and osteochondral tissue engineering, J Biomater Sci Polym Ed 32(4) (2021) 536-561.

[159] W. Dai, M. Sun, X. Leng, X. Hu, Y. Ao, Recent Progress in 3D Printing of Elastic and High-Strength Hydrogels for the Treatment of Osteochondral and Cartilage Diseases, Front Bioeng Biotechnol 8 (2020) 604814.

[160] J. Xue, A. He, Y. Zhu, Y. Liu, D. Li, Z. Yin, W. Zhang, W. Liu, Y. Cao, G. Zhou, Repair of articular cartilage defects with acellular cartilage sheets in a swine model, Biomed Mater 13(2) (2018) 025016.

[161] A.K. Lynn, I.V. Yannas, W. Bonfield, Antigenicity and immunogenicity of collagen, J Biomed Mater Res B Appl Biomater 71(2) (2004) 343-54.

[162] K. Wei, M. Zhu, Y. Sun, J. Xu, Q. Feng, S. Lin, T. Wu, J. Xu, F. Tian, J. Xia, Robust biopolymeric supramolecular “Host− Guest Macromer” hydrogels reinforced

by in situ formed multivalent nanoclusters for cartilage regeneration, Macromolecules 49(3) (2016) 866-875.